Surface plasmon lasers

Tenner, V.T.

Citation

Tenner, V. T. (2017, June 22). *Surface plasmon lasers*. *Casimir PhD Series*. Retrieved from https://hdl.handle.net/1887/49932

Author: Tenner, V.T.
Title: Surface plasmon lasers
Issue Date: 2017-06-22

Surface plasmon lasers

PROEFSCHRIFT

ter verkrijging van
de graad van Doctor aan de Universiteit Leiden,
op gezag van Rector Magnificus prof. mr. C. J. J. M. Stolker,
volgens besluit van het College voor Promoties
te verdedigen op donderdag 22 juni 2017
klokke 10.00 uur

door

Vasco Tomas Tenner

PROMOTORES
Prof. dr. M. P. van Exter
Prof. dr. E. R. Eliel

PROMOTIECOMMISSIE

Dr. C. Genet	(Université de Strasbourg, France)
Prof. dr. J. Gomez Rivas	(Technische Universiteit Eindhoven)
Dr. M. J. A. de Dood	
Prof. dr. M. A. G. J. Orrit	
Dr. ir. S. J. van der Molen	
Prof. dr. J. M. van Ruitenbeek	

COVER IMAGE
By Vasco Tenner and Dirk Boonzajer Flaes. It shows the intensity and phase of the laser beam emitted by a surface-plasmon laser operating in the B-mode of a hexagonal metal hole array at distances from the sample ranging from $1\,\mu\mathrm{m}$ (left bottom) to $300\,\mu\mathrm{m}$ (right top). The images are based on the intensity and phase measurements shown in Fig. 6.4 and propagated numerically to the desired distance with a Fresnel propagator. The colors encode the local phase of the $j = \pm 3$ component of the beam. Every image is scaled in order to create an esthetical ensemble.

The research reported in this thesis was conducted at the ‘Leids Instituut voor Onderzoek in de Natuurkunde‘ (LION).

An electronic version of this dissertation is available at the Leiden University Repository (https://openaccess.leidenuniv.nl).

Casimir PhD series, Delft-Leiden, 2017-20

ISBN: 978-90-8593-304-5

The mountains are calling and I must go.

John Muir

Aan Rosalie

Contents

Appendix

4 Measurement of the phase and intensity profile of surface plasmon laser emission 43

Appendices

5 Surface plasmon dispersion in hexagonal, honeycomb and kagome plasmonic crystals 57

6 Two-mode surface plasmon lasing in hexagonal arrays 69

Appendices

Chapter 1

Introduction

1.1 Wave confinement and surface plasmons

Confining a wave of wavelength λ to a limited volume of space with typical dimension L is quite an easy task provided that the dimension L is larger than the wavelength λ. Musical instruments and lasers provide prime examples of this idea. In both cases the confinement gives rise to resonant enhancement of the wave-field amplitude. In contrast, when the volume is much smaller than the wavelength, the wave cannot be confined in this resonator-like fashion and resonant enhancement is non-existent.

Nature, however, does provide a totally different system of wave confinement, namely on an interface between two materials. There, surface waves can exist and the name betrays the nature of the wave phenomenon: it is confined to the interface. Ocean waves and coastal edge waves [1, 2] are prime examples of this particular wave phenomenon, and so are surface plasmons (SPs). The latter are electromagnetic-like waves that hug the interface between good metals, such as silver and gold, and a dielectric.

Surface plasmons consist of light coupled to free electrons on a metal-dielectric surface and hence are strongly confined to this surface. The electromagnetic field induces a temporal charge redistribution in the metal and it oscillates the electrons at optical frequencies. The strong confinement leads to a large enhancement of the wave amplitude, opening up the possibility of strong light-matter interaction.

During the last 20 years the study of surface plasmons has experienced an enormous revival, mostly as a consequence of novel and advanced nanofabrication techniques. It has led to a large variety of applications of surface plasmons, such as sensors based on surface-enhanced raman-spectroscopy of molecules [3]. Here, SPs are employed to increase the light-matter interaction and drastically enhance the single-molecule signal up to 10-orders of magnitude [4]. Closer related to the work in this thesis are optical metamaterials [5, 6], where artificial building blocks are used to create materials with unprecedented optical properties such as a negative refractive index [7–9]. These metamaterials have been used to create ultra-thin lenses [10–13], waveplates [14–16], and rudimentary invisibility cloaks [17]. A particular example of a simple metamaterial in which SPs play an important role is a metal hole array. It consists of a metal film perforated by a lattice of sub-wavelength nano-holes. Metal hole arrays form two-dimensional crystals for SPs. They exhibit extraordinary transmission [18], meaning that more light is transmitted than is expected from the surface area of the holes. This extraordinary transmission is mediated by SPs.

Absorption in the metal poses a limitation on the application of SPs. This absorption is caused by electron scattering (Ohmic loss) and hence unavoidable. To mitigate this absorption, an optical gain material next to the metal surface can be employed for loss compensation [19]. Due to the strong confinement of the light, only a thin ($\sim$ 120 nm) gain layer is needed: SPs with an energy equivalent to photons with a free space wavelength of 1500 nm are confined within 200 nm from the gold-semiconductor interface. Figure 1.1 shows a schematic of the layer stack of our samples, consisting of a 100 nm thick gold layer on a semiconductor (InGaAs) gain layer top of a InP substrate. It also illustrates the confinement of the SP field at the Au-semiconductor surface. As soon as the Ohmic loss and all other losses of the SP mode are compensated, SP-laser action can occur [20].

Lasers are known to emit coherent, monochromatic, and strongly directional beams. There are two essential components to a laser: a (pumped) gain medium and a resonator. The resonator confines the laser mode and supplies the feedback needed to obtain coherence. The aim of this thesis is to understand SP lasers and to investigate to which extent they can be described by traditional laser theory. We focus primarily on the resonators which, in our case, are formed by metal hole arrays.

1.2 Surface plasmon lasers

SP lasing has been observed in several resonator geometries, from nano particles to metal hole arrays. The first claim of SP-laser action was based on observations of isolated 14 nm-large nano particles [21]. However, these results are disputed on theoretical and experimental grounds and have not been reproduced by other groups to date. Next, Hill et al. [22] demonstrated SP lasing in metal-coated semiconductor nano pillars, in which a localized resonance in such a pillar forms a zero-dimensional resonator. SP-laser action also has been observed in nano-wire systems, in which the gap between a

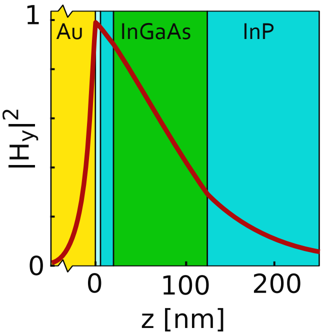

Figure 1.1: A side-view of our devices, consisting of an Au metal hole array on top of a semiconductor (InGaAs) gain layer on a InP substrate. The red curve shows the intensity of the H_y component of the SP-field. The SP field decays away from the metal-dielectric interface. Details are given in Fig. 2.1.

semiconductor nano wire and a silver surface serves as a one-dimensional resonator [23]. These experiments were later extended to two-dimensional geometries, where the feedback is provided by total internal reflection of the SPs in the semiconductor gain medium [24].

Two-dimensional resonators can also be based on distributed feedback, where the optical feedback is not provided by a Fabry-Pérot cavity comprising two highly reflective mirrors but by scattering on a periodic array, either in the form of holes in a metal [20, 25] or metal particles on a substrate [26–30]. Both periodic arrays support SPs and SP lasing, and they form two-dimensional crystals for SPs. For metal hole array SP lasers, the resonator is formed by the reflection of traveling SPs on the holes, as discussed below. In contrast, for particle-array SP lasers, the interplay of localized particle-resonances and non-localized lattice resonances typically plays an important role and the feedback can be described by coupled localized harmonic oscillators. Research on particle arrays has demonstrated, among others, lasing in the strong-coupling regime [30] and the influence of randomness [29].

SP lasing in metal hole arrays has been demonstrated at wavelengths ranging from the visible regime (~ 0.6 μm) to the THz regime (~ 100 μm). The first demonstration originates from our group in Leiden, for SP lasers operating at telecom wavelengths (~ 1.5 μm) using a solid-state semiconductor gain medium [20]. Later, others used molecular dyes as gain medium in the visible regime [25]. Metal hole arrays are also used as resonator for lasers

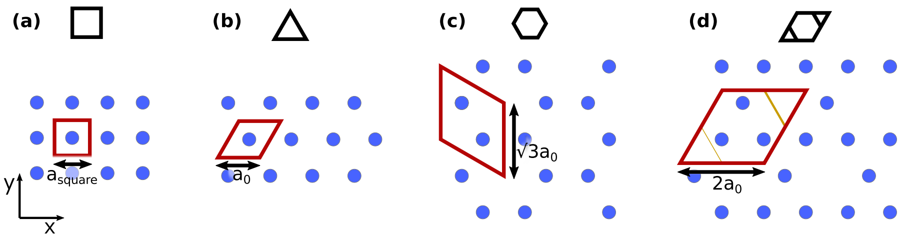

Figure 1.2: Schematic images of the 4 different two-dimensional crystal lattices studied in this thesis: (a) square, (b) hexagonal, (c) honeycomb and (d) kagome. Their unit cells are indicated by red parallelograms.

at much longer wavelengths, corresponding to THz frequencies [31, 32]. However, at these frequencies the confinement of SPs above the surface is weak and the confinement can only exist due to the specific structure on the surface; hence, these SP are called spoof-surface plasmons [33] to indicate that they differ considerably from ordinary SPs.

1.3 Crystals and band structures in two dimensions

Crystals are periodic structures that can be described by their unit cell and by their Bravais lattice or associated reciprocal lattice vectors $\vec{G}_i$. Besides a translation symmetry, most crystals exhibit additional mirror and rotation symmetries, which can be described by point groups. In this thesis we will consider two-dimensional crystals for SPs, consisting of lattices of metal holes in a gold film. Figure 1.2 displays a schematic overview of the studied crystals, which are square lattices (C_{4v}-point group) and three hexagonal-based lattices (C_{6v}-point group): hexagonal, honeycomb and kagome. The spacing between the holes is comparable to the wavelength of the SPs. The hexagonal-based lattices have the same symmetry, but increasingly more complex unit cells.

The dispersion relation describes the relation between the wavelength $\lambda = 2\pi/k$ (or wavevector $\vec{k}$) of a wave and its energy (or frequency ω). It plays a central role in solid-state physics, where it forms, among others, electronic conduction and valence bands, and determines the performance of diodes, LEDs and transistors. It also plays a central role in the description of optics and plasmonics in crystals. In both cases, crystals severely alter the dispersion relation.

Periodic structures and crystals scatter waves and create standing waves

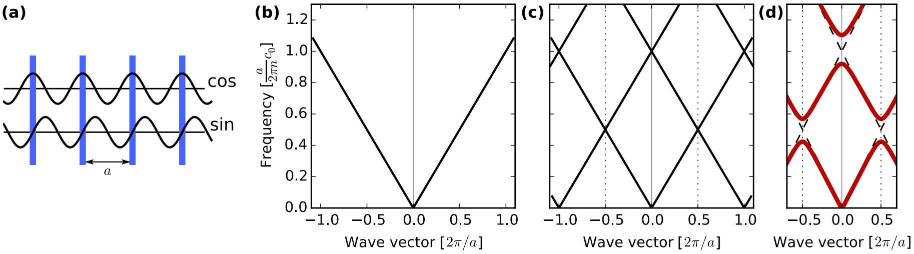

Figure 1.3: (a) One-dimensional crystal lattice with lattice spacing a. Dispersion of (b) free waves, (c) waves in a periodic lattice, and (d) waves in a scattering periodic lattice.

that can completely stop the wave propagation in specific crystal directions. The formation of such bands in the dispersion relation is due to the combination of scattering on the unit cell and their periodic nature. This is most easily explained for a one-dimensional infinitely-large crystal. Figure 1.3(a) shows several unit cells of a one-dimensional crystal with lattice spacing a and lattice vector $G = 2\pi/a$. Figure 1.3(b) shows the linear dispersion of a free wave. The slope is linked to the effective refractive (group) index via the relation $d\omega/dk = c/n_{eff}$. Figure 1.3(c) shows the dispersion of a wave in a one-dimensional crystal. The periodicity of the crystal induces a periodic repetition in the dispersion relation; wave vectors spaced with a lattice vector $\vec{k}_1 - \vec{k}_2 = \vec{G}_i$ are equivalent such that all information is contained in the first Brillouin zone $\left[-\vec{G}_i/2, \vec{G}_i/2\right]$. At higher order Γ-points ($k = 0$, $\omega > 0$) left- and right-traveling waves cross and their wavelength fits on the lattice. Figure 1.3(d) shows the influence of scattering on the holes in the unit cell. The scattering couples part of the left-traveling wave to the right-traveling wave (and vice-versa); standing waves are formed and avoided crossings appear. The anti-symmetric (sine-type) standing wave has nodes on the holes, while the symmetric (cosine-type) standing wave has anti-nodes on the holes, as shown in Fig. 1.3(a). Hence, these two standing waves have different energies $\omega_\pm = \omega_0 \pm \gamma$, where γ is the amplitude scattering rate, and a stop-gap is formed, i.e. an energy range in which no waves can travel in a certain direction.

In two dimensions, the band structure is more complex than in one dimension as waves and scattering in additional directions have to be included [34]. We study the formation of SP bands in two-dimensional crystals with square symmetry in chapters 2 and 3, and with hexagonal symmetry in

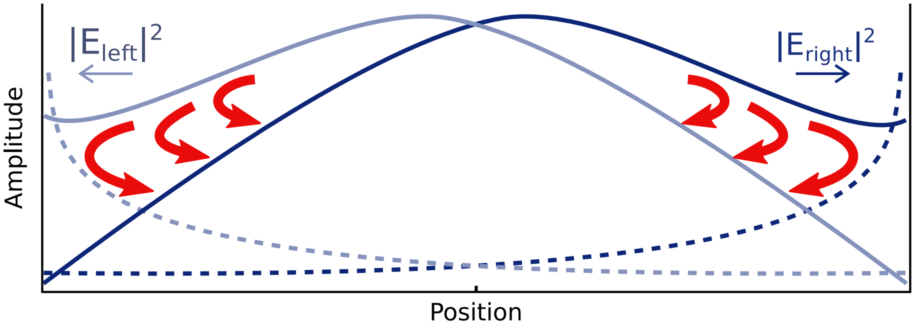

Figure 1.4: Fields inside an one-dimensional distributed feedback laser. The dashed curves show field profiles when no coupling is present, the solid curves show the profiles in the presence of coupling.

chapter 5. We also study the influence of the shape of the unit cell on the scattering rates and its link to the scattering by a single hole.

1.4 Lasing in finite size crystals

The analysis of the dispersion relation of two-dimensional crystals presented in the previous section works fine for very large crystals, but is insufficient for the description of SP-laser action in crystals of finite size. This finite size alters the band structure; it breaks apart the continuous band structure of infinite-large crystals into discrete modes. Suited for lasing in finite size crystals is distributed-feedback laser theory [35]. This theory describes the laser field as traveling waves in real space that are, again, coupled via scattering. Figure 1.4 shows how this scattering confines the field to the center of a one-dimensional device.

In two-dimensional crystals traveling waves in additional directions should be included in this distributed-feedback laser theory; it becomes more complicated and no analytical solutions are known. Numerical modeling of the combination of strongly-confined SPs and gain is challenging and hence experiments are invaluable in order to understand the behavior of such systems. The first realizations of lasing in two-dimensional crystals was in photonic crystals. Since then the field blossomed and produced, among others, Watt-class surface-emitting photonic-crystal lasers [36]. Utilization of this knowledge can accelerate the development of SP lasers and SP sensors.

1.5 Outline of this thesis

In this thesis, we study SP-laser action in metal hole arrays. We try to understand these systems and connect this understanding to existing knowledge about lasers. The figure below schematically displays the contents of this thesis. The two columns indicate that we have studied SP-lasers in metal hole arrays with different geometries: square lattices (left column) and hexagonal-based lattices (right column). The two rows indicate that we have studies these structures both below lasing threshold (top row) and above lasing threshold (bottom row). Below threshold we measured the dispersion of the SPs and extracted information on their loss and scattering rates. Above threshold, we observed SP-laser operation and retrieved information about intensity and phase profiles, polarization, optical feedback and spatial non-uniformities. All these experiments have contributed to our understanding of SP physics in metal hole arrays.

	□	△ ⬡ ▱
Below laser threshold	**Chapter 2** SP dispersion & SP scattering 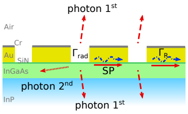 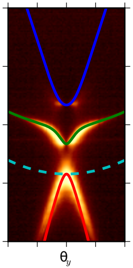 **Chapter 3** Loss & SP-photon scattering	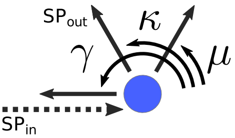 **Chapter 5** SP-SP scattering & link to a single hole
Above laser threshold	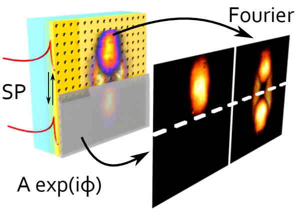 **Chapter 4** Intensity, phase & feedback	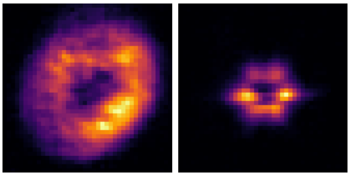 **Chapter 6** Tuning between lasing in two modes

Chapter 2

Surface plasmon dispersion in metal hole array lasers

We experimentally study surface plasmon lasing in a series of metal hole arrays on a gold-semiconductor interface. The sub-wavelength holes are arranged in square arrays of which we systematically vary the lattice constant and hole size. The semiconductor medium is optically pumped and operates at telecom wavelengths ($\lambda \sim 1.5$ µm). For all 9 studied arrays, we observe surface plasmon (SP) lasing close to normal incidence, where different lasers operate in different plasmonic bands and at different wavelengths. Angle- and frequency-resolved measurements of the spontaneous emission visualizes these bands over the relevant $(\omega, k_{\parallel})$ range. The observed bands are accurately described by a simple coupled-wave model, which enables us to quantify the backwards and right-angle scattering of SPs at the holes in the metal film.

This chapter was previously published as:
M. P. van Exter, V. T. Tenner, F. van Beijnum, M. J. A. de Dood, P. J. van Veldhoven, E. J. Geluk, and G. W. 't Hooft, *Surface plasmon dispersion in metal hole array lasers*, Optics Express **21**, 27422 (2013)

2.1 Introduction

Surface plasmons are intrinsically lossy due to the ohmic losses of the metals at which these optical excitations occur. To better harvest the unique properties of surface plasmons, in particular their compact (sub-wavelength) size, it would be great if we could compensate their losses with a nearby gain medium. Successful loss compensation enables lossless plasmonics and surface plasmon lasing [38]. This feat has been accomplished in various geometries, ranging from metal-coated nanopillars [22], to metal-coated nanorings [39] and nanowires on a silver film [23]. The common denominator in these experiments is the use of semiconductor gain media, as these media can provide huge gain. This gain is typically provided at infrared and telecom wavelengths, where surface plasmons are less confined, more photonic, and thus less lossy than in the visible range. Alternative laser medium like dyes can supply enough gain to compensate the losses of special SP excitations, like long-range surface plasmons [40] and resonances in plasmonic nanoparticle arrays [28].

Surface plasmons play a dominant role in the optical excitation and transmission of metal films perforated with a regular lattice of sub-wavelength holes, the so-called metal hole arrays. In 1998, the optical transmission of these arrays was found to be extra-ordinary large [18] on account of the resonant excitation of surface plasmons (SP). Many experiments have followed since, aimed to unravel the intriguing properties of SPs propagating and scattering on these arrays [41–44].

The periodic nature of a metal hole array, which provides distributed feedback through scattering, is ideally suited for the construction of a plasmonic laser. Plasmonic crystal lasing was first demonstrated at mid-infrared wavelengths in quantum cascade lasers [45]. Very recently, it was also demonstrated at telecom wavelength (1.5 μm) in loss-compensated hole arrays in a gold-semiconductor structure [20]. Surface plasmon lasing was observed and three experimental proofs were reported to demonstrate the surface plasmon character of the lasing mode [20]. These experiments were performed on square arrays with a lattice spacing comparable to the SP wavelength, i.e. in so-called second-order Bragg structures.

In this chapter, we expand on the results reported in [20] by presenting a systematic study of surface plasmon lasing in a series of 9 square hole arrays with different lattice spacings and hole sizes. We compare their laser characteristics, such as emission wavelengths, lasing thresholds, and the remarkable donut-shaped modes in which these lasers emit. We focus on the angular and wavelength dependence of the luminescence that they emit, both below and above their lasing threshold. This luminescence is shown to be concentrated in four plasmonic bands, similar to the photonic bands that exist in photonic crystals. The observed shape/dispersion of these plasmonic bands can be well described with a simple coupled-mode model of four traveling SP waves that are coupled by SP-SP scattering and emit into a fifth free-space (= photonic) mode by SP-photon scattering. By analyzing these plasmonics bands for a series of devices, we present the first performance overview of surface plasmon lasing in metal hole arrays.

2.2 Experimental setup

Figure 2.1(b) shows the layer package of all studied devices. This package comprises a 105 nm thick $In_{0.53}Ga_{0.47}As$ (gain) layer grown lattice-matched on a 300 μm thick double-polished InP wafer and capped with a 100 nm gold layer on top. A thin (15-20 nm) spacer layer, comprising SiN_x and InP and a very thin sticking layer ($\sim$ 0.5 nm chromium), in between the gold and the $In_{0.53}Ga_{0.47}As$ layer prevents quenching of the excited carriers [46]. A 20 nm thick chromium layer on top of the gold damps SPs at the gold-(chromium)-air interface. The red curve in Fig. 2.1(b) shows the square of the magnetic field profile associated with the surface plasmons at the gold-(spacer layer)-semiconductor interface. The presence of the spacer layer, with its lower refractive index, widens this profile somewhat and decreases the effective index of the SP mode, compared to that of SPs on a gold-semiconductor interface without spacer layer.

A square lattice of circular holes is patterned into the gold by a standard lift-off process that uses an array of pillars defined by e-beam lithography in a 400 nm thick layer of HPR504 resist capped with a 80 nm layer of HSQ resist. The relevant lattice spacings in our square arrays are $a_0 = 450$ nm, 460 nm, and 470 nm. For each lattice spacing we produced arrays with different hole size, by fine-tuning the e-beam dose in steps of 10%, which we denote as $d1$, $d2$, and $d3$ for increased dose and hole diameter. Each of these $3 \times 3 = 9$ arrays was produced as a $50\,\mu\text{m} \times 50\,\mu\text{m}$ pattern.

Figure 2.1(a) shows our experimental geometry. The $In_{0.53}Ga_{0.47}As$ active/gain layer is optically excited through the InP substrate, using a continuous-wave Nd:YAG laser (wavelength 1064 nm) that is spatially filtered with a pinhole and imaged into a circular top-hat shape with a diameter of $\sim$ 49 μm. This beam diameter is larger than the $\sim$ 30 μm reported in [13] because we now use a $f = 75$ mm lens instead of a $f = 50$ mm lens to focus the pump light. The fluorescence and laser radiation produced by the sample is observed on the gold side, using a far-field imaging system that enables us to measure the emitted intensity $I(\theta_x, \theta_y; \lambda)$ as a function of emission angle $\boldsymbol{\theta} \equiv (\theta_x, \theta_y)$ and vacuum emission wavelength λ. More specifically, the light emitted through the cryostat window is first collimated by a 20x microscope objective with a numerical aperture of 0.4, is then focused by an $f = 20$ cm (tube)lens to produce a 20x direct image of the source, and is finally reconverted into a far-field image by an $f = 5$ cm lens. We measure the far-field intensity $I(\theta_x, \theta_y; \lambda)$ by scanning a single-mode fiber in the focal plane of the final lens and analyzing the collected spectrum with a grating spectrometer. The cryostat window (0.5 mm AR-coated BK7) is thin enough to limit spherical and other optical aberrations in the imaging system. The full imaging system has an angular resolution of $\sim$ 4 mrad and a wavelength resolution of $\sim$ 1 nm.

The sample is operated at cryogenic temperatures in a Helium flow cryostat. The

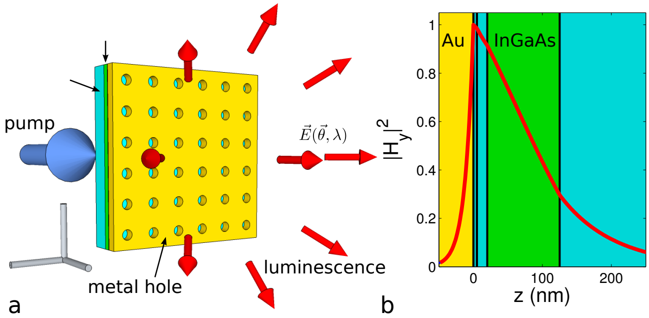

Figure 2.1: (a) Sketch of experimental geometry. We optically excite the gain layer through the substrate, using a continuous-wave pump laser, and observe its fluorescence and laser emission on the metal size, as a function of emission angle and wavelength. (b) The layer package of all samples consists of InP substrate, an $In_{0.53}Ga_{0.47}As$ gain layer, a thin spacer layer, and gold on top (see text for details). The red curve shows the calculated (square of the) magnetic field $|H_y|^2$ of the surface plasmon polaritons, which are excited by fluorescence, amplified by stimulated emission, and scattered by the holes.

base temperature of the cryostat is 8 K. Based on a simple model of pump-induced heating we estimate the temperature difference between the pumped region and the rest of the wafer to be limited to 5 K at 125 mW pump power. This value is small, primarily because the heat conductivity of InP is extremely large at cryogenic temperatures, with a local maximum around 20 K and heat conductivities exceeding 10^3 W/Km between 8 and 45 K [47]. The thermal contact between the InP wafer and the rest of the cryostat might be limiting though. An indication that this is indeed the case is that the SP laser power decreases in the first few second after switch-on.

2.3 Angle-dependent spectra

The optical characteristic of one of our structures, with lattice spacing $a_0 =$ 470nm and hole size d_2, has already been reported in [20]. This device exhibits a clear lasing threshold with intense directional emission in a narrow spectral band above the lasing threshold. Below the lasing threshold, the wavelength-dependent far-field emission pattern $I(\theta_x, \theta_y; \lambda)$ provides insight on the nature of the optical excitation. Three experimental proofs were presented to substantiate the claim that lasing occurs in the surface plasmon mode: *(i)* all emission patterns can be modeled with a single effective index n_{eff} with a value comparable to that expected for the only guided wave, being the SP, *(ii)* laser emission occurs in a remarkable donut-shaped beam with the radial polarization expected for SPs, being TM waves, and *(iii)* the coupling between the traveling waves, observable as avoided crossings in the $(\omega, k_{\parallel})$ dispersion, is as large as expected for SPs. In this chapter we will apply similar analysis tools to our full set of 3×3 structures.

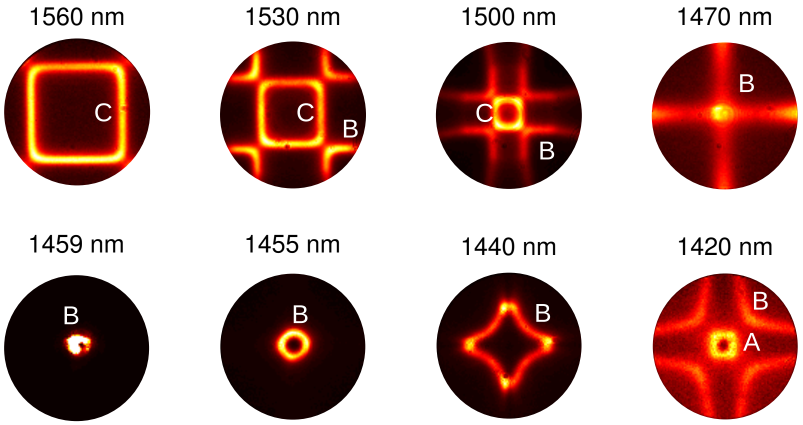

Figure 2.2: Far-field emission pattern of ($a_0 = 450$ nm, d2) laser observed within the NA=0.4 of our microscope objective at detection wavelengths ranging from 1560 to 1420 nm. The emission features can be divided in three groups: a low-frequency (C), mid-frequency (B), and high-frequency (A).

Figure 2.2 shows the far-field emission patterns $I(\theta_x, \theta_y; \lambda)$ of one of our lasers ($a_0 = 450$ nm, d_2) at eight selected emission wavelengths, observed under our "standard excitation condition" ($P = 125$ mW in a 49 μm diameter disk). The wavelength decreases, i.e. the optical frequency increases, from left to right and top to bottom. All patterns exhibit the 4-fold rotation and (x, y) mirror symmetry expected for square arrays. For decreasing wavelength, the observed structures first move inwards and then move outwards again. The false-color scale varies from picture to picture, being normalized at the individual peak intensities, which increase from 2 at $\lambda = 1560$ nm to 10 at $\lambda = 1500$ nm, peaks at a saturated value $\gg 60$ at the lasing wavelength of $\lambda = 1459$ nm, and decreases to 9 at $\lambda = 1455$ nm and to 0.9 at $\lambda = 1420$ nm (all in arbitrary units).

The emitted structures depicted in Fig. 2.2 can be directly interpreted as equifrequency contours of the plasmonic bandstructure. The observed structures can be divided into three groups, each of which can be assigned to a specific plasmonic band. We have labeled these bands as A, B, and C from high to low frequency. The C band starts as a large square with rounded corners at $\lambda = 1560$ nm and shrinks to disappear between 1500 and 1470 nm. The wavelength dependence of the B band is more complicated. The B band is visible in the four corners at

λ = 1530 nm, transforms into a full cross at 1470 nm, then turns into a small circle at $\lambda = 1459$ nm, and grows into a larger circle at 1455 nm that transforms into a star at 1440 nm and a larger open star at 1420 nm. The A band starts as a small square at $\lambda = 1420$ nm and increases in size towards lower wavelengths (not shown). Our ($a_0 = 450$ nm, $d2$) device lases in the B band at a lasing wavelength of $\lambda = 1459$ nm, where the false-color image is a saturated white. In contrast, the ($a_0 = 470$ nm, $d2$) array studied in [20] lased in the A band at $\lambda = 1479$ nm.

It is instructive to compare the patterns in Fig. 2.2 with a similar set of patterns obtained for the ($a_0 = 470$ nm, $d2$) laser and displayed as Fig. 3 in [20]. The two sets are comparable, but the wavelengths at which similar features appear are red-shifted by approximately 4.5 % in the $a_0 = 470$ nm laser on account of the larger lattice spacing. Hence, the patterns displayed in [20] show more of the A band. A closer comparison between our Fig. 2 and Fig. 3 in [20] also shows subtle differences. For instance, (i) our 4-lobed star at $\lambda = 1440$ nm has intensity maxima at its tips, whereas the 4-lobed star at 1500 nm for the $a_0 = 470$ nm device has intensity minima at its tips, and (ii) the compact structure of the A band that we observe at $\lambda = 1420$ nm looks like a square, whereas a similar structure observed at 1480 nm for the $a_0 = 470$ nm device resembles a circle. Figure 2.2 thus presents a wealth of information that provides insight on the influence of SP-SP scattering on the plasmonic bandstructure.

2.4 Comparison of nine surface-plasmon lasers

In the rest of this chapter we will limit the discussion of the angle dependent fluorescence spectrum $I(\theta_x, \theta_y; \lambda)$ to its θ_y dependence, i.e. we fix $\theta_x = 0$. For this purpose, we combine the angular and spectral profile $I(\theta_x = 0, \theta_y; \lambda)$ in a single false-color dispersion plot. In the experiment, this plot is recorded by taking only a one-dimensional angular scan at fixed $\theta_x = 0$.

The intensity profile $I(0, \theta_y; \lambda)$ enables us to visualize the plasmonic bands of the SPs on the hole array. By choosing the angle θ_y as horizontal axis and the wavelength λ in inverted order as vertical axis, the resulting figure closely resembles the standard $(\omega, k_\parallel)$ dispersion diagram, where $\omega = 2\pi c/\lambda$ is the optical frequency and $k_\parallel = k_y = (2\pi/\lambda)\sin(\theta_y)$ is the photon momentum parallel to the interface.

Figure 2.3 shows the measured intensities $I(0, \theta_y; \lambda)$ for each of our $3 \times 3 = 9$ samples, under identical pump conditions (P = 125 mW in a 49 μm disk). A polarizer was inserted to single out the vertical (= p = TM) polarization and thereby limit the number of photonic bands from 4 to 3 (see Sec. 2.5). The data in Fig. 2.3 is arranged in a rectangular grid. The hole size increases from left to right ($d1-d3$) and the lattice spacing increases from top to bottom ($a_0 = 450, 460,$ and 470 nm). All figures have the same scale, $\theta_y = -0.4$ to 0.4 rad and λ = 1400 to 1600 nm, indicated only in the top-left figure. Each figure contains all three photonic bands (A, B, and C), albeit at different wavelengths and with different intensities.

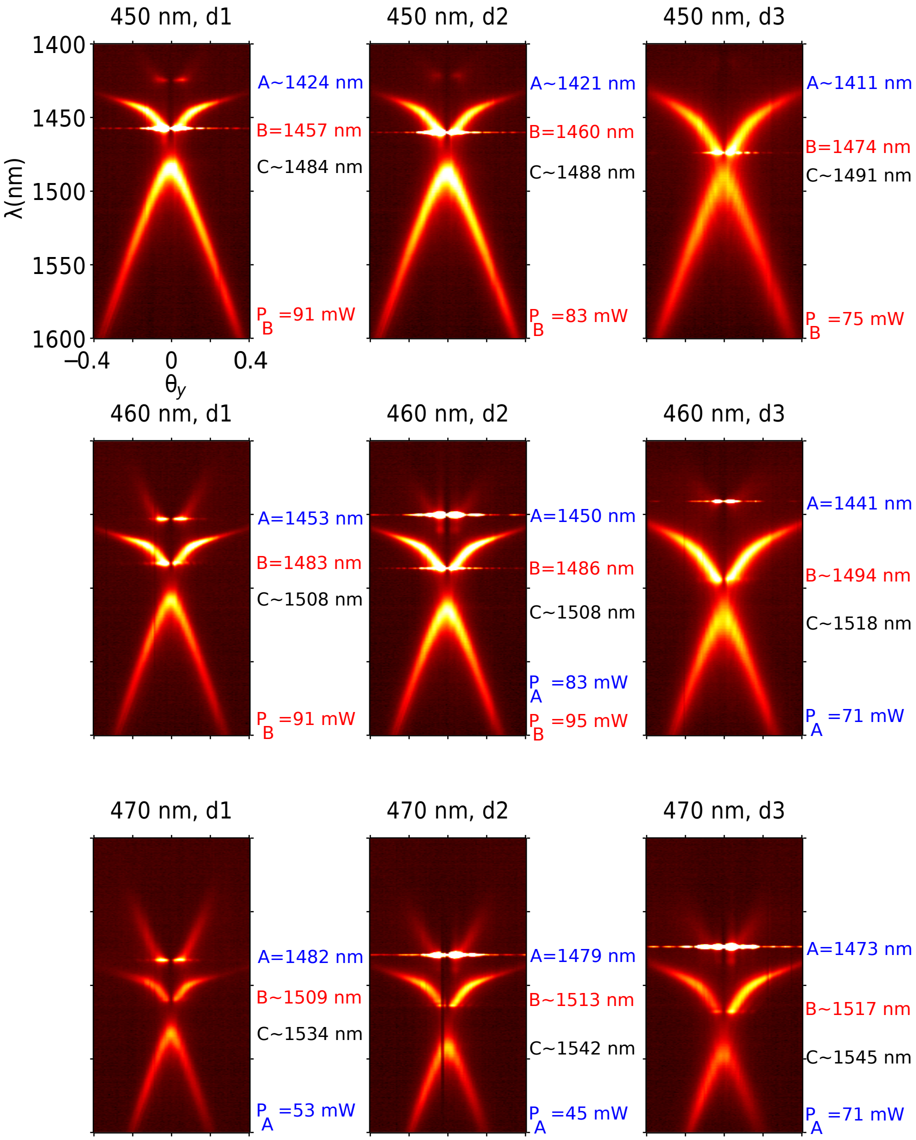

Figure 2.3: False-color images of the measured far-field intensities $I(0, \theta_y; \lambda)$ of our devices, which vary in lattice spacing (top to bottom; indicated in nm), and hole size (left to right; indicated as d1-d3). Lasing is visible as a saturated white, which often turns into a saturated stripe. The scale in all figures runs from $\theta_y = -0.4$ to 0.4 mrad and from $\lambda = 1400$ to 1600 nm and is indicated only in the top left figure. The inverted vertical axis helps to compare these figures with the standard $(\omega, k_{\|})$ dispersion diagrams. The righthand side of each figure contains information on the wavelengths of the A, B, and C bands close to normal incidence and the pump threshold of lasing modes. Note the color coding of the three bands.

The wavelengths around the $\theta_y = 0$ center of each band ($\theta_x = 0$ in all scans) is added on the righthand side of each figure, and denoted for instance as $B = 1457$ nm when lasing occurs in the B band and as $A \sim 1424$ nm when the A band only contains fluorescent emission in a somewhat wider spectral band.

When comparing the 9 pictures in Fig. 2.3, the first thing we notice is their similarity. Moving from lattice spacing $a_0 = 450$ down to 460 and 470 nm (top to bottom), all features shift downwards, such that the ratio λ/a_0 remains approximately constant. This certainly applies to the A band at hole size $d1$, where the ratio $\lambda_A/a_0 = 3.16$, 3.16, and 3.15 for $a_0 = 450, 460$, and 470 nm, respectively. It is less valid for the C band in this series, for which $\lambda_C/a_0 = 3.30$, 3.28, and 3.26, respectively.

The next thing we notice is that the frequency splitting between the resonances increases when the hole size increases (from left to right). More specifically, for the $a_0 = 450$ nm device we find $\lambda_A - \lambda_C = 60$ nm for hole size $d1$, 67 nm for $d2$, and 80 nm for $d3$, making the relative splitting $\Delta\lambda_{AC}/\overline{\lambda}_{AC} \equiv 2(\lambda_A - \lambda_C)/(\lambda_A + \lambda_C) =$ 0.041, 0.046, and 0.055, respectively. Similar numbers apply to the lattice with $a_0 = 460$ nm, where we find $\Delta\lambda_{AC}/\overline{\lambda}_{AC} = 0.037$, 0.039, and 0.052, and to the 470 nm devices, where we find $\Delta\lambda_{AC}/\overline{\lambda}_{AC} = 0.034$, 0.042, and 0.048, respectively. All numbers are accurate to ± 0.001. The increased splitting between the A and C bands is accompanied by a downwards shift of the B band towards the C band, as if the A and B bands repel each other. The coupled-mode model introduced in Sec. 2.5 explains both effects as an avoided crossing of photonic bands, induced by SP-SP scattering at the holes. The observed splittings are consistent with a picture where the radiative splitting increases monotonously with the ratio d/λ probed in the experiment.

Another thing to note is the different appearance of the three photonic bands. While the low-frequency C band has the more or less standard form of two straight lines, connected and capped by a smooth top, the B and the A band have a more intriguing angle dependence. Both bands are visible only away from the surface normal at $\theta \neq 0$. The B band starts off with an almost linear dispersion that quickly levels off, while the A band resembles two straight lines that loose their intensity before they meet.

All 9 studied devices exhibit laser action at the investigated pump power of 125 mW in a 49 μm disk, corresponding to a pump density $P/\text{Area} = 6.6$ kW/cm^2, but the lasing thresholds, at which an intense sharp spectral feature appears, differ. These threshold powers are indicated by P_A and P_B for laser action in the A and B band, respectively. The ($a_0 = 460$ nm, $d2$) device lases in both bands, seemingly simultaneously but probably in an alternating way. Under slightly different alignment, this behavior was also observed for the ($a_0 = 450$ nm, $d1$) and ($a_0 = 450$ nm, $d2$) devices, but not indicated here. The ($a_0 = 470$ nm) devices have the lowest thresholds, which starts at 53 mW for the $d1$ laser, decreases to 45 mW for the $d2$ laser, and increases to 71 mW for the $d3$ laser. This variation indicates that there is an optimum hole size for surface plasmon lasing.

The accuracy of the threshold measurements is limited to ±20%, as the lasing threshold depends on the location of the 49 µm round pump spot within the 50 µm square array. For all devices, laser action typically occurred over the full pumped area, but the emission was seldom spatially uniform over this area and for some devices it was clearly concentrated at the edges of the array. These spatial observations were made with an infrared CCD illuminated with a magnified direct image of the devices.

Lasing in either the A or B band occurs at comparable threshold powers. None of the studied devices lased in the C band, nor did this laser action occur in a similar set of devices with lattice spacing $a_0 = 440$ nm, where the C band was shifted upwards in the figures to a resonance wavelength of $\lambda_C \approx 1462$ nm, more in line with the lasing wavelengths of the other devices.

Each lasing device emits its light in a remarkable beam profile that is approximately donut-shaped, radially polarized, and centered around the surface normal [20]. Although this statement applies to all lasers, the angular widths of the emitted donut beams are noticeably different. The beams emitted in the A band typically have an angular diameter of $\Delta\theta \approx 65 \pm 6$ rad. The beams emitted in the B band are less collimated, with typical diameters of $\Delta\theta \approx 85 \pm 8$ rad. This diameter is comparable to the diameter of $\Delta\theta \approx 90 \pm 10$ rad (FWHM 120 rad [20]) measured for the same laser under excitation with a 2/3× smaller pump spot. There is, apparently, no simple (Fourier) relation between these opening angles $\Delta\theta$ and the size of the pump spot. Furthermore, the product of opening angle times pump size is considerably larger than the value expected from Fourier relations.

After the optical inspection presented above, we took the sample out of the cryostat and placed it in a scanning electron microscope (SEM) for inspection and an experimental estimate of the hole diameters. This inspection showed that the holes were nicely circular and uniform (standard deviation in hole size 1-2%). The measured hole diameters d are: (180, 179, and 175 nm) for $d1$, (189, 187, and 183 nm) for $d2$, and (221, 206, and 202 nm) for $d3$, where the numbers in parentheses refer to the samples with lattice spacings $a_0 =$ (450, 460, 470 nm). As expected, the hole diameter increases with e-beam dose and increases slightly with decreasing a_0 due to proximity effects.

2.5 Coupled-mode model

This theoretical section presents a relatively simple coupled-mode model for the observed angular emission spectrum $I(0, \theta_y; \lambda)$ and the associated plasmonic bands. Before doing so, we first note that the highly directional nature of the observed spectrum is not as straightforward as one might think. On the contrary: we expect the direct fluorescent photon emission through the holes to be spread out over all angles, because each sub-wavelength hole radiates like a dipole and because radiation from neighboring holes should hardly be correlated, as the fluorescent medium is thin in relation to the hole spacing. The observed directionality of the emission, on the other hand, proofs the existence of long-range coherence between the emitting holes. This coherence must be created by traveling-wave surface plasmons that are excited by fluorescence and later converted into photons by coherent scattering on the holes in the lattice. More specifically, most photons emitted at an angle (θ_x, θ_y), with an associated photon momentum $\mathbf{k}_{\|} \equiv (k_x, k_y)$ with $k_x = (2\pi/\lambda)\sin\theta_x$ and $k_y = (2\pi/\lambda)\sin\theta_y$, originate from coherent scattering of traveling-wave SPs with momenta $\mathbf{k}_{\mathrm{sp}} = \mathbf{G}_i + \mathbf{k}_{\|}$, where $\mathbf{G}_i$ is a lattice vector. For our device, which has modest scattering and operates close to the 2^{nd}-order Bragg condition $k_{\mathrm{sp}} \equiv |\mathbf{k}_{\mathrm{sp}}| \approx 2(\pi/a_0)$ only four SP traveling waves are important. These corresponds to the four fundamental lattice vectors with $|\mathbf{G}_i| \equiv G = (2\pi/a_0)$, pointing in the four lattice directions $\{\mathbf{e}_x, \mathbf{e}_{-x}, \mathbf{e}_y, \mathbf{e}_{-y}\}$. We will thus denote them as the $+x, -x, +y$, and $-y$ traveling waves, although strictly speaking their wavevector might deviate slightly from these directions when $k_{\|} \neq 0$ $(k_{\|} \ll G)$.

A first-order approximation of the dispersion of the SP bands neglects the influence of scattering and simply uses the dispersion relation $\omega = |\mathbf{k}_{\mathrm{sp}}|c/n_{\mathrm{eff}}$ of traveling-wave SPs on a smooth metal-dielectric interface, where n_{eff} is the SP effective index. We only consider angle-tuning in the yz-plane, where $\mathbf{k}_{\|} = k_{\|}\mathbf{e}_y$, and use the paraxial (= small-angle) approximation to write $k_{\|} \approx (2\pi/\lambda)\theta_y$. In the equations presented below, we will abbreviate θ_y as θ and often use the approximation $(2\pi/\lambda) \approx (2\pi/\lambda_0)$ for the mentioned prefactor, where $\lambda_0 = 2\pi c/\omega_0 \equiv n_{\mathrm{eff}} a_0$ is a fixed reference wavelength, as wavelength variations within the SP bands are small $(\lambda \approx \lambda_0)$. Under these conditions, it is easy to show that the eigenfrequencies of the two $\pm y$ modes are $\omega(\theta) = k_{\mathrm{sp}}(\theta)c/n_{\mathrm{eff}} = (G \pm k_{\|})c/n_{\mathrm{eff}} \approx \omega_0 \pm c_1\theta$, with $c_1 \equiv \omega_0/n_{\mathrm{eff}}$. The uncoupled $\pm y$ modes thus exhibit a linear dispersion, which can also be written as $\lambda(\theta)/a_0 = n_{\mathrm{eff}} \pm \theta$ if we stick the original form $k_{\|} = (2\pi/\lambda)\theta$. The eigenfrequencies of the two $\pm x$ modes are both $\omega(\theta) \approx \omega_0 + c_2\theta^2$, with $c_2 \equiv \omega_0/(2n_{\mathrm{eff}}^2)$, as the SP wavevector of these modes $k_{\mathrm{sp}}(\theta) = \sqrt{G^2 + k_{\|}^2} \approx (2\pi/\lambda_0)\sqrt{n_{\mathrm{eff}}^2 + \theta^2}$, with $\sqrt{n_{\mathrm{eff}}^2 + \theta_y^2} \approx n_{\mathrm{eff}} + \theta^2/(2n_{\mathrm{eff}})$. The dispersion relations of these four uncoupled traveling SP waves are depicted in Fig. 2.4(a).

In our system, the uncoupled traveling-wave model is accurate enough only at angles sufficiently far away from the surface normal, where it produces the piecewise circular dispersion contours depicted in Fig. 2 of [20]. At smaller momenta $\mathbf{k}_{\|}$, the scattering-induced interaction between the (now almost frequency-degenerate) SP waves needs to be included. We do so with a coupled-mode model that decomposes the SP field at any position $\mathbf{r} \equiv (x, y)$ in its traveling-wave components

$$\mathbf{E}(\mathbf{r}, t) = \left[E_x(t)\mathbf{u}_x e^{iGx} + E_{-x}(t)\mathbf{u}_{-x} e^{-iGx} + E_y(t)\mathbf{u}_y e^{iGy} + E_{-y}(t)\mathbf{u}_{-y} e^{-iGy}\right] e^{ik_{\|}y}, \tag{2.5.1}$$

where $\{E_x, E_{-x}, E_y, E_{-y}\}$ are the modal amplitudes of the four traveling waves and $\mathbf{u}_i$, with $i = \{x, -x, y, -y\}$, are unit vectors that describe the four associated optical polarizations. We choose these eigenvectors to be rotationally-imaged copies of each

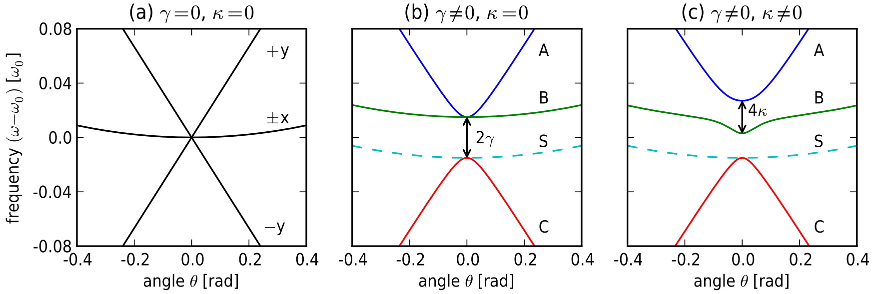

Figure 2.4: Dispersion curves of the four SP bands, depicted as frequency difference $(\omega - \omega_0)$ versus angle θ, for three different models of increasing complexity: (a) uncoupled traveling waves, (b) backscattering only, and (c) right-angle and backscattering. Fig. (a) shows the linear dispersion of the $\pm y$ modes at slope $\pm c_1 = 1/n_{\text{eff}}$, for $n_{\text{eff}} = 3$ and the almost flat-band dispersion for the $\pm x$ modes. Fig. (b) shows the case $\gamma/\omega_0 = 0.015$, where the $\pm y$ bands exhibit an avoided crossing at $\theta = 0$ and where the $\pm x$ bands have a fixed splitting 2γ. The three solid bands A, B, and C couple to p-polarized light, whereas the single dashed S band couples to s polarization. Fig. (c) shows how only the cosine-type modes exhibit a second avoided crossing around $\theta = 0$ when right-angle scattering at a rate $\kappa/\omega_0 = 0.006$ is added.

other, such that the perpendicular component $E_\perp$ of their electric fields are in phase if the modal amplitudes are. Equation (2.5.1) is the Bloch-mode representation of the relevant SP field, in first-order Fourier components only. When the four modal amplitudes are combined into a single vector E, the time evolution of this SP field can be expressed as $dE/dt = -iHE$, where H is a 4×4 matrix. If scattering is neglected, H reduces to a diagonal matrix with the elements/eigenvalues mentioned above, being $\{\omega_0 + c_2\theta^2, \omega_0 + c_2\theta^2, \omega_0 + c_1\theta, \omega_0 - c_1\theta\}$.

The effects of SP scattering can be easily incorporated in the matrix description. The 4-fold rotation and (x, y) mirror symmetry of the square lattice enables us to divide the SP-SP scattering in three fundamental processes: forward scattering under 0°, right-angle scattering under ±90°, and backwards scattering under 180°. Forward scattering at a rate γ_0 merely changes the eigenfrequencies of all traveling waves, but does not couple these waves. It can thus be easily incorporated in our model by redefining the combination $\omega_0 + \gamma_0$ as the new ω_0, which simply indicates that the effective index n_{eff} of SPs on a surface with holes can be different than that of SPs on a smooth surface. Backwards scattering couples the $x \longleftrightarrow -x$ and $y \longleftrightarrow -y$ waves at an amplitude scattering rate γ. Right-angle scattering leads to coupling between the $\pm x \longleftrightarrow \pm y$ traveling waves at an amplitude scattering rate κ.

Inclusion of all coupling rates into our $dE/dt = -iHE$ matrix description yields

$$H = \begin{pmatrix} \omega_0 + c_2\theta^2 & \gamma & \kappa & \kappa \\ \gamma & \omega_0 + c_2\theta^2 & \kappa & \kappa \\ \kappa & \kappa & \omega_0 + c_1\theta & \gamma \\ \kappa & \kappa & \gamma & \omega_0 - c_1\theta \end{pmatrix} \tag{2.5.2}$$

Although the presented model is very general and can be applied to plasmonic as well as photonic crystals [48] it contains one central assumption that needs to be discussed. For simplicity, we have chosen the coupling rates γ and κ to be real-valued, making the coupling conservative and H Hermitian. However, being amplitude scattering rates, γ and κ do not need to be real-valued [49]. They could in principle contain imaginary parts, which would then result in dissipative coupling and (mode-selective) energy loss. Although a future and more detailed analysis will probably show that these imaginary parts are not strictly zero, we prefer the simplicity for now. We can also justify this simplification with two arguments. First of all, theory predicts that small ($\ll \lambda$) holes scatter light in an off-resonant way, such that both the polarizability and the related scattering rates γ and κ are real-valued [50]. Secondly, previous experiments on SPs on an air-metal interface with a grid of 50 nm wide slits measured conservative coupling to dominate over dissipative coupling at a normalized rate of $\gamma/\omega_0 = 0.022$ versus 0.008 for the mentioned geometry [51].

The plasmonic bands of our system are associated with the eigenvalues of the H matrix. As these are quite complicated, we will first consider a simpler system without right-angle scattering, i.e. with $\kappa = 0$, where the H matrix separates in two 2×2 blocks. The lower (y) block describes the prototype avoided crossing with eigenvalues $\omega(\theta) = \omega_0 \pm \sqrt{\gamma^2 + (c_1\theta)^2}$. The associated eigenmodes are $(1, \pm 1)$, with corresponding field profiles $E(\mathbf{r}) \propto \cos Gy$ and $E(\mathbf{r}) \propto \sin Gy$, at $\theta = 0$, and an unbalanced superposition of traveling waves at $\theta \neq 0$. The upper (x) block has eigenvalues $\omega(\theta) = \omega_0 + c_2\theta^2 \pm \gamma$. Its eigenmodes are $(1, \pm 1)$, with corresponding field profiles $E(\mathbf{r}) \propto \cos Gx \cdot \exp ik_y y$ and $E(\mathbf{r}) \propto \sin Gx \cdot \exp ik_y y$, at any θ. These results are depicted in the four dispersion curves in Fig. 2.4(b).

The general case also contains right-angle scattering ($\kappa \neq 0$), which couples the $\pm x \longleftrightarrow \pm y$ traveling waves and thereby complicates the model. Before we resort to numerics, we like to point out that our 4 mode model is actually a 3+1 mode problem. The $(1, -1, 0, 0)$ eigenmode, with eigenvalue $\omega_0 + c_2\theta^2 - \gamma$, is special as it doesn't change with angle and is not affected by right-angle scattering. The physical reason for this is that the $E_0(\mathbf{r}) \propto \sin Gx \cdot \exp ik_y y$ profile of this mode doesn't scatter, because it has intensity minima at the holes, or - phrased in a different way - because the scattering contributions from the two counter-propagating waves interfere destructively. Below, we will argue that this special SP eigenmode is the only mode that emits s-polarized light.

The three remaining SP waves form a coupled set, of which the solution is only simple at $\theta = 0$, where the $(0,0,1,-1)$ eigenmode, with $E_1(\mathbf{r}) \propto \sin Gy$ profile, then has the same eigenvalue $\omega_0 - \gamma$ as the $(1,-1,0,0)$ mode. At $\theta = 0$, the two cosine-type standing waves $\cos Gx$ and $\cos Gy$ couple into two eigenmodes of the form $E_{2,3}(\mathbf{r}) \propto \cos Gx \pm \cos Gy$, with eigenvalues $\omega_0 + \gamma \pm 2\kappa$. At $\theta \neq 0$, they also couple to the $E_1(\mathbf{r})$ mode and the eigenvalue problem now corresponds to finding the roots of a third-order polynomial. Figure 2.4(c) shows the numerically obtained results for the realistic case $\kappa/\gamma = 0.4$.

2.6 SP-photon coupling and vector aspects

It is good to know the SP eigenmodes, but this is not yet the complete story. As the observed fluorescence originates from coherent scattering of the four SP traveling waves, its intensity depends crucially on the (far-field) interference between these scattering contributions. Constructive interference can make some SP modes bright (= radiative), whereas destructive interference can make other SP modes practically invisible (= non-radiative). This phenomenon is clearly visible in Fig. 2.3, where the A and B bands loose their intensity around $\theta = 0$, whereas the C band still radiates.

We also need to consider the vector character of the electro-magnetic fields, which is hidden in the eigenvectors $\mathbf{u}_i$ of the SP waves. By solving Maxwell's equations at a metal-dielectric interface, one quickly finds that each SP traveling wave contains three field components, just like any TM-mode in a planar medium: an in-plane magnetic field $H_{\|}$, perpendicular to the propagation direction, an out-of-plane electric field $E_{\perp}$, and an in-plane electric field $E_{\|}$ in the direction of $\mathbf{k}_{\text{sp}}$, which for the SP is much weaker than $E_{\perp}$ and approximately 90° out of phase with the other two field components. The interference between two counter propagating SP waves depends on the field component that we consider. When the out-of-plane electric field components $E_{\perp}$ interfere constructively, to produce a cosine-type pattern, the two in-plane field components $E_{\|}$ and $H_{\|}$ interfere destructively, into a sine-type pattern, and vice versa. This difference will play a crucial role in the comparison between theory and experiment.

The vector character of the SP field determines the polarization of the emitted light. Instead of discussing the vectorial aspects of the SP-photon scattering, this can also be understood from symmetry, which, for emission at $\theta_x = 0$ is the mirror symmetry in the yz (emission) plane. For TM-polarized waves, the four eigenmodes naturally divide in three vectorial modes that are even under mirror action and therefore only couple to p-polarized light and one mode that is odd and only emits s-polarization [48]. To understand why, let's consider the symmetry of the H field of the four standing waves. The two linear combinations of the $\pm y$ SPs, with magnetic fields $\mathbf{H}(\mathbf{r}) \propto \sin Gy \cdot \exp ik_{\|}y\, \mathbf{e}_x$ and $\cos Gy \cdot \exp ik_{\|}y\, \mathbf{e}_x$, are both even under mirror action, as their field profiles are even and the magnetic field is a pseudovector, and therefore emit p (TM) polarized light in the yz plane. The two linear combinations of the $\pm x$ SPs combine SPs with $\mathbf{k}_{\text{sp}} = \pm G\mathbf{e}_x + k_{\|}\mathbf{e}_y$ and therefore have $\mathbf{H}$ components in both the $\mathbf{e}_x$ and $\mathbf{e}_y$ direction. The combination with dominant magnetic field $H_y(\mathbf{r}) \propto \sin Gx \cdot \exp ik_{\|}y$ is even under mirror action and thus emits p-polarized light, albeit only through coupling with the other even SP modes. The combination with magnetic field profile $\mathbf{H}(\mathbf{r}) \propto \exp ik_{\|}y[\cos Gx\, \mathbf{e}_y - i(k_{\|}/G) \sin Gx\, \mathbf{e}_x]$ is the only combination that is odd and radiates s-polarized light.

The symmetry argument presented above ended with the statement that the SP standing wave with dominant magnetic field profile $H_y(\mathbf{r}) \propto \cos Gx \cdot \exp ik_y y \mathbf{e}_y$ is a 'special' eigenmode. At first sight this statement seems to be in conflict with our 3+1 coupled-mode model, where we concluded that the 'special' eigenmode has a mode profile $E_0(\mathbf{r}) \propto \sin Gx \cdot \exp ik_y y$. This paradox is solved when we realize that the cosine profiles of the in-plane H fields corresponds to a sine profiles of the out-of-plane E field, and vice verse. The former determines the SP-photon coupling, whereas the latter apparently dominates the SP-SP scattering. The special mode was removed in the experiment with a polarizer set for p (TM) transmission.

The next step in theory could be the development of a microscopic model that explains the origin of scattering rates γ, κ, and γ_0. For small holes, this scattering is typically modeled by considering each hole as a polarizable object that scatters through dipole radiation. Under TM-polarized excitation, the induced electric dipole has both an out-plane component $p_\perp$ and an in-plane component $p_{\|}$. The induced magnetic dipole, which is unique in metals, only has an in-plane component $m_{\|}$. The orientation of these dipoles derive three general rules for the relative magnitudes of the mentioned scattering rates: (i) right-angle SP-SP scattering is only supported by the electric dipole $p_\perp$, (ii) forwards and backwards SP-SP scattering are supported by both $p_\perp$ and $m_{\|}$, albeit in different combinations ($p_\perp + m_{\|}$ versus $p_\perp - m_{\|}$), and (iii) the SP-photon scattering observed close to the surface normal is insensitive to $p_\perp$ and dominated by $m_{\|}$, as $p_{\|}$ is typically weak.

Whether the hole is small enough to validate the dipole approximation mentioned above depends on the ratio of hole radius r over SP wavelength λ_{sp}. The observed hole diameters in all our sample, apart from ($a_0 = 450$ nm$, d3$), span a range $d = 2r = 175$-206 nm, which corresponds to dimensionless ratio's $r/\lambda_{\text{sp}} = 0.19 - 0.22$. Figure 2 in the supplementary material of [50] indicates that these ratio's are at the edge of validity range of the dipole approximation: the electrical polarizability is still dominantly real-valued, but the magnetic polarizability already has a sizeable imaginary component. Hence we expect κ to be dominantly real-valued, whereas γ might already have a sizeable imaginary component.

2.7 Comparison experiment and theory

After having presented the experimental dispersion curves in Fig. 2.3 and the theoretical curves in Fig. 2.4(c), we are finally able to compare the two. We start by noting that Figure 2.3 displays only the three p (TM) polarized bands. The fourth s-polarized band exhibits hardly any dispersion and has a (very wide) extremum with a central wavelength that practically coincides with that of the C band, as demonstrated in Fig. 2.5 below for one of the lasers. This s-polarized band is without any doubt the special $E_0(\mathbf{r}) \propto \sin Gx \cdot \exp ik_y y$ band.

A qualitative comparison between the nine experimental pictures in Fig. 2.3 and the theoretical prediction in Fig. 2.4 leaves no doubt about the labeling of the p-polarized bands. The high-frequency band A and the low-frequency band C are the $\pm y$ traveling waves, with eigenvalues $\omega_0 \mp c_1\theta$ and field profiles $E(\mathbf{r}) \propto \exp i(k_{\|} \pm G)y$ at large θ, whereas the mid-frequency band is the B band. This labeling is supported by two arguments. First of all, the observation that the center of the C band practically coincidence with the center of the s-polarized band is as expected: at $\theta = 0$ these modes have the same eigenvalue $\omega_0 - \gamma$ and comparable mode profiles ($E_0(\mathbf{r}) \propto \sin Gx$ versus $E_1(\mathbf{r}) \propto \sin Gy$. The A and B modes, on the other hand, have different eigenvalues $\omega_0 + \gamma \pm 2\kappa$ and eigenmodes $E_{2,3}(\mathbf{r}) \propto \cos(Gx) \pm \cos(Gy)$ at $\theta = 0$.

The proposed labeling is also consistent with the radiative or non-radiative character of the eigenmodes around $\theta = 0$. The C and s-polarized modes have a sine-type profile in $E_\perp$ and a corresponding cosine-type profile in $E_{\|}$ and $H_{\|}$, which makes them radiative modes. The A and B modes, on the other hand, have cosine-type profiles in $E_\perp$ and sine-type profiles in $E_{\|}$ and $H_{\|}$, and therefore do not radiate at $\theta = 0$. The A and B band indeed becomes extremely faint and disappears close to the surface normal. The overall labeling is also supported by optical transmission spectra, recorded with white light incident along the surface normal, which only show the resonance of the (radiative) C band but not those of the (non-radiative) B and A bands [19].

We have fitted all 9 dispersion curves in Fig. 2.3, by looking in particular at the fit quality around $\theta = 0$. The frequency difference between the upper bands $(\omega_A - \omega_B) = 4\kappa$ at $\theta = 0$ yields the rate of right-angle scattering rate, although we do not know its sign. The frequency difference between the average of the upper two bands and the lower band $(\omega_A + \omega_B - 2\omega_C)/2 = 2\gamma$ at $\theta = 0$ yields the back scattering rate. In this case we do know the sign. The observation that the split bands lie above the degenerate bands shows that $\gamma > 0$, such that modes with a cosine-type $E_\perp$-profile have a higher resonance frequency and a larger effective index than the modes with a sine-type profile. The numbers obtained from these fits correspond to right-angle scattering rates $\kappa/\omega_0 = 0.005 - 0.011$ for increasing hole size. The backwards scattering rate $\gamma/\omega_0 = 0.013 - 0.017$ is considerable larger and increases less rapidly with hole size. Our observation that $\gamma > \kappa$ is consistent with the notion that the induced magnetic dipole $m_{\|}$, which contributes only to γ, is a stronger scatterer than the induced electric dipole $p_\perp$, which scatters in all directions. For comparison, we note that in holes in dielectric slabs, which scatter only through electric dipoles, typically yield a scattering rate γ that is (somewhat) larger that κ, such that the special s-polarized band for coupled TM modes now coincides with the B band instead of the C band [48].

Figure 2.5 shows a detailed comparison of the measurements and fits for one of

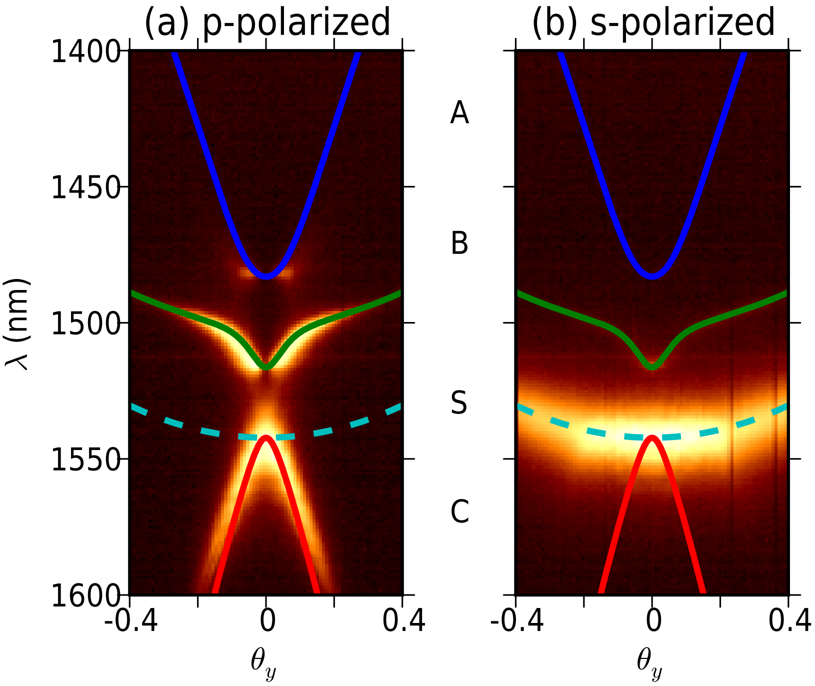

Figure 2.5: Dispersion curves of four SP bands of the ($a_0 = 470$ nm, $d2$) laser for (a) p-polarized and (b) s-polarized emission. The three solid and single dashed curve show the p-polarized (A, B, C) bands and the s-polarized S band and are calculated based on three fit parameters: γ, κ and n_{eff} (see text).

our lasers. Figure 2.5(a) and 2.5(b) show the p-polarized and s-polarized emission, respectively, of the ($a_0 = 470$ nm, d_2) laser (see also supplement of [20]). The combined fit, depicted as three solid curves and one dashed curve, is based on $\gamma/\omega = 0.0140$, $\kappa/\omega = 0.0056$, and $n_{\mathrm{eff}} = 3.235$, and optimized by eye. The high quality of this combined fit is typical for all studied lasers.

The most intriguing aspect of surface plasmon lasers is undoubtedly their approximately donut-shaped and radially-polarized emission. In the above discussion, we have linked the central hole in the donut to the non-radiative character of the A and B modes that these lasers operate on. An obvious question to ask, then, is whether the SP field in the laser simply avoids the fundamental wave vectors $\mathbf{k}_{\mathrm{sp}} = \mathbf{G}_i$ or whether the SP field in the laser is far more intense then we actually observe, because laser action also occurs at $\mathbf{k}_{\mathrm{sp}} = \mathbf{G}_i$, but is simply invisible as SPs in non-radiative bands barely couple to the outside world. The latter scenario is quite plausible, in particular because non-radiative modes are bound to be the first ones to lase, precise because they hardly suffer from radiation loss. Hence we expect that our SP lasers might be (much) brighter than they seem to be.

In future research, we would like to study the optical coherence within the emitted donut-like beams. We will also try to make the C mode lase in at least one of our devices, in order to check whether the characteristics of this radiative band are really as different as we expect them to be.

2.8 Conclusion

In conclusion, we have presented a systematic study of the performance of a series of semiconductor metal hole array lasers with different lattice spacings and hole sizes. Angle- and wavelength-resolved measurements of the luminescence of the $\mathrm{In}_{0.53}\mathrm{Ga}_{0.47}\mathrm{As}$ gain medium provides important insight in the nature of the lasing modes and the dispersion of all surface plasmon (SP) resonances on the hole arrays. The hole arrays act as a second-order Bragg reflector that provides distributed feedback to the laser close to normal incidence. We observe four plasmonics bands, which correspond to four linear superpositions of SP traveling waves, and could identify all bands. Three bands couple to p-polarized light, of which only one radiates along the surface normal. One band couples to s polarized light and also radiates along the surface normal. A relatively simple coupled-wave model enables us to extract the amplitude rates for SP-SP scattering, both under 90° (κ) and in the backwards direction (γ). For the lasers studied in this chapter, with a hole diameter to lattice constant of $d/a \approx 0.4$, the observed plasmonic bandstructures correspond to amplitude scattering rates $\kappa/\omega_0 = 0.005 - 0.011$ and $\gamma/\omega_0 = 0.013 - 0.017$ for right-hand and backwards scattering, respectively.

Acknowledgements

We acknowledge M.T. Hill, M.J.H. Marell, E. Smalbrugge, T. de Vries, and W. Löffler for discussions and help. This work is part of the research program of the Foundation for Fundamental Research on Matter (FOM), which is part of the Netherlands Organization for Scientific Research (NWO).

Chapter 3

Loss and scattering of surface plasmon polaritons on optically pumped hole arrays

We study surface plasmons on 2-dimensional square arrays of subwavelength holes in a gold film deposited on an optically-excited semiconductor. We observe four resonances of which we measure the resonance frequencies, the spectral widths, and the relative intensities. The spectral widths allow us to quantify various loss processes, including ohmic loss, optical absorption/gain and radiative scattering loss. Prominent kinks in the plasmon dispersion relation occur around the Rayleigh anomaly. A coupled mode model that includes a frequency dependent gain of the semiconductor reproduces the main features in the experimental data.

This chapter was previously published as:
V. T. Tenner, A. N. van Delft, M. J. A. de Dood, and M. P. van Exter, *Loss and scattering of surface plasmon polaritons on optically-pumped hole arrays*, Journal of Optics **16**, 114019 (2014)

3.1 Introduction

Surface plasmons polaritons or surface plasmons (SPs) are a combined optical and electronic solution to Maxwell equations bound to an interface. These surface plasmons can be localized on a nano particle, or they can be traveling along an extended interface. One remarkable property of SPs is the strong confinement normal to the interface, with exponentially decaying fields in both media. Several applications benefit from the strong confinement of the field that can be used to enhance the light-matter interaction, for example in molecular sensors [53, 54]. The strong confinement can also be used to guide SP and build plasmonic circuits, including beam splitters [55]and phase manipulators [56]. Similarly, meta-materials often consist of sub-wavelength metal structures where the plasmon modes are responsible for many of their extraordinary properties, such as the ability to create negative refractive index materials [7, 8].

Although SP-based systems are highly succesfull, the main limiting factor is loss, which can be divided in (ohmic) absorption loss and scattering loss. For instance, SPs traveling on smooth Ag or Au interfaces are typically absorbed after 2-100 μm [57] for wavelengths between 0.5 and 1.5 μm. Gain can be introduced to overcome this limitation and several demonstrations of complete loss compensation have been shown, using a semiconductor [19] or dye [40] as gain material. SP-lasing action is possible when complete loss compensation is combined with a mechanism for optical feedback. This feedback has been demonstrated in several structures [58], including metal-coated nano-pillars [22], gold nano-spheres [21], and metal hole arrays [20].

In this chapter, we study the modes of metal hole arrays with gain. These structures are comparable to the structures that we have studied before [20, 37]. To gain insight in the lasing mechanism it is essential to identify the modes responsible for lasing. This can be done by measuring the dispersion of plasmonic bands and quantifying the spectral width of these modes. This analysis is best performed below the lasing threshold, where optical saturation and other nonlinear optical processes are not yet relevant. In our earlier work we reported avoided crossings of the mode frequencies and compared this to a coupled mode model [37]. In this chapter, we extend this analysis and extract the frequency, width and total intensity of each mode, by fitting the angle dependent emission spectra. The measured width allows to quantify the effective ohmic loss as well as the scattering loss rate. We augment the coupled mode model to include frequency dependent gain. This extended coupled mode model captures all the main features without introducing a large number of unknown parameters. This allows to identify the physical mechanisms that are most relevant to lasing action of SPs in metal hole arrays. This simplified model necessarily misses some of the details that are visible in the experimental data. Most notably, we identify abrupt changes in the dispersion of the plasmonic bands and the associated width of the resonances that coincide with a Rayleigh anomaly.

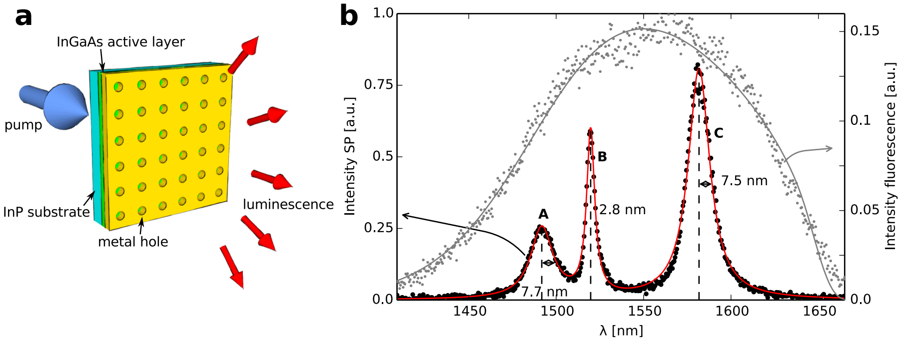

Figure 3.1: a) Sketch of setup. Samples are optically pumped through the substrate and fluorescence is collected through the hole array. A fiber on a translation stage placed in the far field allows to measure spectra as a function of angle. b) Spectrum of p-polarized light emitted at ($\theta_x = 0$, $\theta_y = 0.10$) rad. The fit (red curve) is based on a sum of three Lorentzian resonances. The half widths of these peaks are indicated in the graph. The grey symbols show the measured fluorescence on a piece of the wafer without a gold layer. The line through this data is a model that describes the frequency dependent gain (see text).

3.2 Methods

3.2.1 Sample

The semiconductor-gold samples that we studied are identical to the ones described in refs [20, 37]. Their layer structure, depicted in Fig. 3.2, comprise a 100 nm thick gold film on a 105 nm thick $\mathrm{In}_x\mathrm{Ga}_{1-x}\mathrm{As}$ semiconductor layer that is lattice matched ($x \simeq 0.53$) to a 300 µm thick, double polished, InP substrate. A 15-20 nm thick SiN_x/InP spacer-layer between the $\mathrm{In}_x\mathrm{Ga}_{1-x}\mathrm{As}$ and the gold prevents quenching of the optically excited semiconductor. A 20 nm thick chromium layer on top of the gold damps the SP resonance on the gold-air interface, leaving only the gold-semiconductor resonances. The gold layer is perforated with holes with a diameter of 180 nm. The holes are arranged in a 50x50 µm square grid with a spacing $a_0 = 470$ nm between the holes.

3.2.2 Experimental geometry

Fig. 3.1a shows the experimental geometry. We optically excite the InGaAs active/gain layer through the InP substrate with a continuous-wave pump laser with a wavelength of 1064 nm. The resonances of the system are all visible below the laser threshold, and hence the incident power (120 mW) was kept below laser threshold of the device at a temperature of 120 K. The pump spot on the sample had a square shape with a size of 45x45 $\mu\mathrm{m}^2$. This pump beam creates electron-hole pairs in the active layer of InGaAs material. These carriers radiatively recombine and couple light into the plasmon modes of the metal hole array living on the gold-semiconductor interface. The grey curve in Fig. 3.1b shows the measured spectrum of this radiative recombination for a part of the sample without gold.

The collection part of our setup was the same as in [20, 37]. The fluorescence light was collected in the far field at the gold side of the sample as a function of angle (θ_x, θ_y). More precisely, the light was collected using a 20x microscope objective with a numerical aperture of 0.4. Sequentially the array structure was magnified 20x by a lens with a 20 cm focal length. Finally, the far field of the sample was reached in the back-focal plane of a lens (focal length 5 cm), where the fluorescence light was collected on a spectrometer using a single mode optical fiber ($w \approx 10\mu\mathrm{m}$ $@\lambda = 1500$ nm). This fiber was scanned in the far field by a 2-dimensional translation stage. In this chapter we keep the fiber at $\theta_x = 0$ and scan the fiber only in the θ_y direction, from $\theta_y = -0.44$ rad to $\theta_y = 0.44$ rad in 110 steps, but we limit all figures to the most relevant part $-0.3 \leq \theta_y \leq 0.3$. The angle θ_y is related to the in-plane momenta in the y-direction (Γ-M) by $k_{\|} = (\omega/c)\sin\theta_y$[37]. A thin film polarizer was used to discriminate between vertical (p=TM) and horizontal (s=TE) polarized light.

Figure 3.1b shows a typical p-polarized emission spectrum, obtained at an angle $\theta_y = 0.10$. This spectrum contains three peaks, labeled by A, B and C. A curve consisting of three Lorentzians fits the data very well. We repeated these measurements at other angles θ_y and for both polarizations, where similar high quality fits yielded the position, the spectral width (half height half maximum, HWHM), and the integrated intensity of each of the three peaks. The observed angle dependence of the frequencies, spectral widths, and integrated intensities of these resonances are discussed below.

3.3 Theory

We analyze all our data with a model based on four coupled surface plasmon modes. This model, which is discussed in the Appendix, extends the work of [37]. It includes the SP-to-SP scattering that dominantly determines the SP dispersion relation [37]. As an extension it also includes SP losses due to SP-to-photon scattering, ohmic losses, and optical gain. These loss/gain channels determine the spectral widths of the resonances. We describe these losses as imaginary rates in the coupled mode model and thus obtain a complex plasmonic bandstructure.

Our model contains the following parameters: SP-to-SP coupling is parameterized by scattering rates γ and κ, which refer to back-scattering and right-angle-scattering, respectively[37]. The ohmic loss and optical gain are combined into a reduced ohmic loss rate $\Gamma_R = \Gamma_r - g(\omega)$, where the ohmic loss Γ_r rate includes surface-roughness related effects. Finally, SP-to-photon coupling occurs at a radiative loss rate Γ_{rad} for the traveling waves, and at loss rates $2\Gamma_{\mathrm{rad}}$ or 0 for the standing

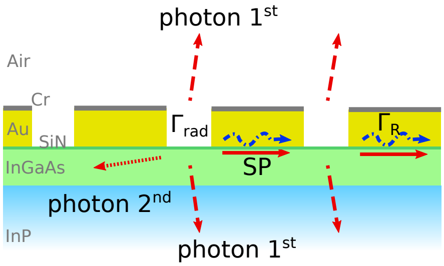

Figure 3.2: Loss channels of SP. The reduced ohmic loss, denoted by the loss rate Γ_R, is spatial uniform and includes the effective optical gain. The radiative loss, denoted by the loss rate Γ_{rad}, occurs only at the holes and originates from scattering of SPs to photons. At large angle, the SP-to-photon scattering is distributed over three diffraction orders: 1st order diffraction into the air, and 1st and 2nd order diffraction into the semiconductor. We only observe the emission into air and analyze it as a function of frequency and emission angle.

waves (depending on the positions of their nodes).

The various loss channels are depicted in Fig. 3.2. The radiative loss originates from scattering of surface plasmons to photons in air and to photons in the semiconductor. At sufficiently large angles a Rayleigh anomaly becomes visible in the data. This anomaly opens a second scattering channel and is expected to lead to an increase in the radiative loss [59] and may affect the SP dispersion via a Kramer-Krönig-type relation. This second scattering channel is denoted as photon 2nd in Fig. 3.2, where the other channels are denoted as photon 1st.

By combining the (complex) amplitudes of the four coupled SP modes in a four-vector $|E(t)\rangle$, the time evolution of the SP field can be described by a single equation

$$\frac{d}{dt}|E(t)\rangle = -iH|E(t)\rangle + |S(t)\rangle\,, \tag{3.3.1}$$

where the evolution matrix H contains all scattering and loss/gain processes. The vector $|S(t)\rangle$ describes the spontaneous emission that continuously feeds the SP field (see Appendix for details). We use two versions of this equation to model our experimental results. In our basic model we keep all parameters in the evolution matrix constant and neglect the frequency dependence of the spontaneous emission. This model is most easy to implement and already demonstrates various key features of the system, such as the separation of the four coupled modes into three p-polarized modes and one s-polarized mode. The symmetry of the square lattice also force the modes to be radiative and non-radiative modes. In our advanced model we include the most prominent frequency dependences, being that of the spontaneous emission $S(\omega)$ and the optical gain $g(\omega)$. For simplicity, and to keep the number of fit parameters limited, we will not include the milder frequency dependences of the various scattering rates and the appearance of the additional scattering channel depicted in Fig. 3.2.

The spontaneous and stimulated emission in the semiconductor originate from radiative recombination of electron-hole pairs. These emission rate, and the associated optical gain, depends on the density of states of electrons and holes in the conduction and valence bands and their fractional occupations $0 < f_{c/v} < 1$. For the usual parabolic bands, the electronic density of states has a $\sqrt{E-E_g}$ dependence above the bandgap E_g, while the fractional occupations are Fermi-Dirac functions of the form $f_{c/v} = 1/[1+\exp(E-E_{F,c/v})/k_B T]$. The optical transitions are direct, i.e. $\Delta k \approx 0$, and the heavy hole mass of lattice-matched InGaAs is much larger than the effective electron mass ($m_h/m_e \approx 5$) [60]. As a result, the frequency dependence of the emission rate is well approximated by the occupation in the conduction band. We model the emission rate and frequency dependent gain as [61]

$$\begin{aligned} S(\omega) &\propto \sqrt{\hbar\omega - E_g} f_c (1-f_v) \\ &\approx \sqrt{\hbar\omega - E_g} \frac{1}{1+\exp(\hbar\omega - E_{F,c})/k_B T} (1-f_{v,0}), \end{aligned} \tag{3.3.2}$$

$$\begin{aligned} g(\omega) &\propto \sqrt{\hbar\omega - E_g} (f_c - f_v) \\ &\approx \sqrt{\hbar\omega - E_g} \left(\frac{1}{1+\exp(\hbar\omega - E_{F,c})/k_B T} - f_{v,0} \right), \end{aligned} \tag{3.3.3}$$

where $(1-f_v)$ is the hole occupation and $f_{v,0}$ is the electron occupation at the top of the valence band. Note that the optical gain originates from the balance between stimulated emission and absorption, where the absorption generates the minus sign in front of $f_{v,0}$. Our extended model includes four additional fit parameters. The bandgap energy E_g, the Fermi energy $E_{F,c}$, and the effective temperature T can be determined experimentally by comparing the measured spontaneous emission spectrum of the bare sample, depicted in Fig. 3.1b, with the above equation. This leaves only one adjustable parameter, being the valence band occupation $f_{v,0}$ which controls the amount of absorption. We note that the outcome of the model is not very sensitive to the exact value of this parameter and use $f_{v,0} \sim 0.5$ to obtain reasonably good agreement with the experimental data.

3.4 Results

In this section we present measurements of the resonance frequencies of the four SP modes, their widths and total intensities. These measurements are in essence contained in the false-color plots of the measured (angle- and polarization-dependent) spontaneous emission spectra shown in Fig. 3.3a and b. In Fig. 3.3a three p-polarized resonances are visible, labeled with A, B and C. Fig. 3.3b shows one intense s-polarized resonance, labeled S. We analyzed these measurements with two different versions of a coupled-mode model to obtain physical relevant

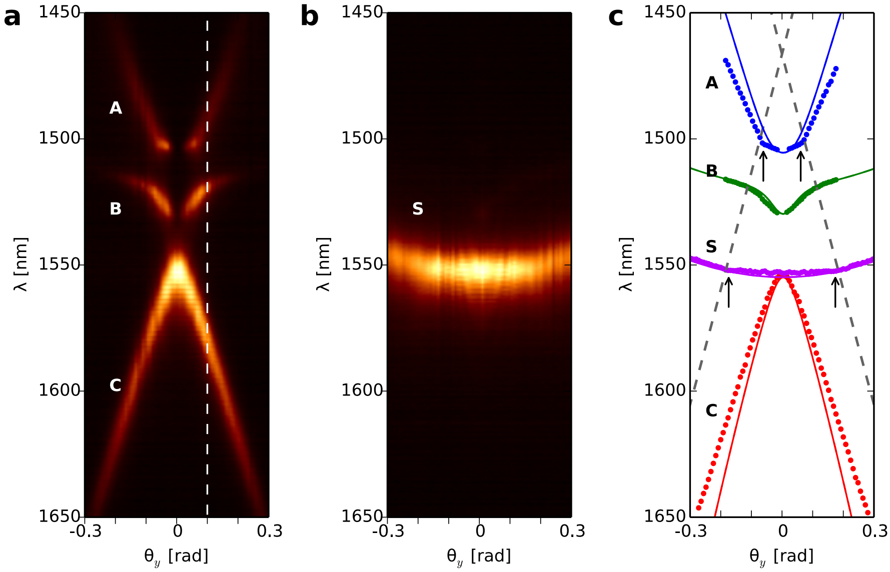

Figure 3.3: False color plots of the measured fluorescence intensity $I(\theta_y, \lambda)$ of a) p-polarization and b) s-polarization. The y-axis depicts energy, in units of vacuum wavelength of the collected photons. The white dashed line in a) at $\theta_y = 0.10$ indicates the cross section shown in Fig. 3.1. c) The resonance frequencies of the bands deduced from the measurements. The dashed lines show the light line of the semiconductor. The arrows mark clear kinks in the dispersion relation.

phenomena and parameters. The two models predict similar dispersion curves, but differ in their predictions of modal linewidths and intensities. Most of the extra parameters required for the advanced model can be obtained for the fluorescence spectrum measured in the absence of gold: the fit curve depicted in Fig. 1b) yields an effective temperature (190K), band filling (down to 1494 nm), and band gap (1653 nm) sample. To remove the unphysical abrupt change at $E = E_{F,c}$ in eq. (3.3.2) and (3.3.3) a convolution with a 17 THz wide Hann window function was used to obtain the spontaneous emission and gain functions used in the advanced model. The subsections below describe the analysis of the resonance frequencies, the widths and the total intensities, respectively.

3.4.1 Resonance frequencies

Figure 3.3c shows the resonance frequencies of all bands. The dispersion of the p-polarized A, B, and C bands shows an avoided crossing. This crossing is modified by the presence of the (intermediate) B band, which exhibits a remarkable dispersion.

To describe the data we use a coupled mode model, which is described in detail in the appendix. Our measured dispersion curves can be well fitted with amplitude scattering rates $\gamma/\omega_0 = +0.012$ and $\kappa/\omega_0 = \pm 0.004$ and an effective refractive index $n_{eff} = 3.268$ as shown with the solid lines in Fig. 3.3. These values are comparable to values found in ref. [37], where SP dispersion curves measured for nine similar arrays could be well fitted with rates $\gamma/\omega_0 = +0.013$ to $+0.017$ and $\kappa/\omega_0 = \pm 0.005$ to ± 0.011 [37]. We observe that the model deviates from the measured resonance frequencies of the A and C band for larger angles.

Abrupt changes in the dispersion curves of the A and S band are located at $\theta = \pm 0.06$ and $\theta = \pm 0.17$, respectively, and these kinks are marked with arrows in Fig. 3.3c. The A and S band are more flat between the kinks. We do not observe clear kinks in the B and C band. Our relatively simple model does not predict the kinks and flat region of the A and S band. We note that the kinks in the dispersion curves coincide with the positions where they cross the light line of the substrate. This suggests that there is a connection between these kinks and the occurrence of a Rayleigh anomaly, i.e., at the point where an additional diffraction order becomes visible in the substrate. This suggestion is further supported by the observation of a relatively sudden increase in the SP loss rate beyond this point (see below). The dashed light lines in Fig. 3.3c correspond to $n \simeq 3.12$, which is close to the value of $n = 3.10$ of the InP wafer. The thin InGaAs layer and the even thinner SiN_x/InP layer are too thin ($\ll \lambda$) to support a guided (optical) mode and modify this anomaly. We do not yet understand why these kinks are only visible in the S and A band, but not in the B band, which also crosses the light line.

3.4.2 Linewidths

Figure 3.4 shows the observed linewidths of the four SP bands. The C and S band have a large linewidth of $\Delta\omega/\omega \simeq 0.0045$ near $\theta = 0$, while the A and B band have a small linewidth of $\Delta\omega/\omega \simeq 0.001$. The C band is the only band with a linewidth that does not depend on angle. Also the linewidth of the S band is almost constant, except from the sudden increase at $\theta = \pm 0.17$, marked with arrows in Fig. 3.4b. The linewidth of the B band is M shaped, with a minimum at $\theta = 0$.

The basic coupled mode theory, without frequency dependent gain and emission, already explains most of the features that we observe as shown with the dashed lines in Fig. 3.4. For instance, it explains why the SPs in the C and S band are more lossy than the SPs in the A and B band. The reason is that the former scatter efficiently to photons, whereas the latter do not scatter to photons at small angles. At $\theta = 0$ the spectral width of the radiative modes $\Gamma_{C,S} = 2\Gamma_{\mathrm{rad}} + \Gamma_R$ is set by the radiative and reduced ohmic losses, whereas the spectral width of the dark modes $\Gamma_{A,B} = \Gamma_R$ is only determined by the reduced ohmic losses. The experimental results presented in Fig. 3.4 correspond to $\Gamma_R/\omega \leq 0.001$ and $2\Gamma_{\mathrm{rad}}/\omega \simeq 0.004$. This SP-to-photon

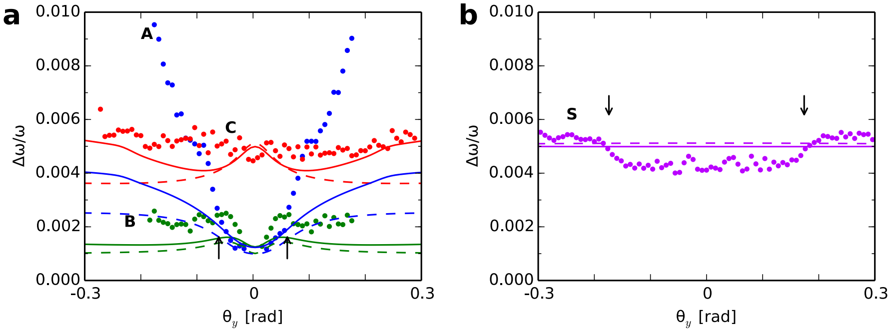

Figure 3.4: Linewidths of the a) p-polarized b) s-polarized bands. The points indicate the experimental values, whereas the curves indicate the predictions of the basic (dashed) and advanced (solid) model. The angle for the observed kink in the A and S band is marked by the arrows.

scattering rate is approximately six times lower than the backscattering rate, but two times higher than the reduced ohmic losses for the applied pump power and temperature.

Extending the model with a frequency dependent gain improves the fits to the A and C band, as shown with the solid lines in Fig. 3.4. Due to the band gap and finite band filling the gain is lower for the A and C band at higher angles. This leads to a larger linewidth at larger angles. The observed linewidth of the A band is still larger than our model predicts. This discrepancy might possibly be explained by both the exact shape of the electron bands in the semiconductor as by a physical description of the Rayleigh anomaly. A good quantitative picture of the Rayleigh anomaly, and in particular the intensity that is carried away by this anomaly is lacking without extensive numerical calculations.

3.4.3 Total intensity

Figure 3.5 shows the integrated intensity, $A = \pi I_{max}\Delta\lambda$, of the individual resonances, where I_{max} is the maximal intensity of the band and $\Delta\lambda$ is its spectral width (half width half maximum). The C and S band have a large integrated intensity with a maximum at $\theta = 0$, whereas the A and B band are much fainter and have a minimum near $\theta = 0$. We call the C and S mode bright/radiative and the A and B mode dark/non-radiative [37].

The first thing to note in Fig. 3.4b is the distinction between the bright C and S bands and the dark A and B bands, in particular around $\theta \approx 0$. This observation is easily understood from the theoretical observation that the bright bands have field maxima at the holes, while the dark bands have field minima at the holes around

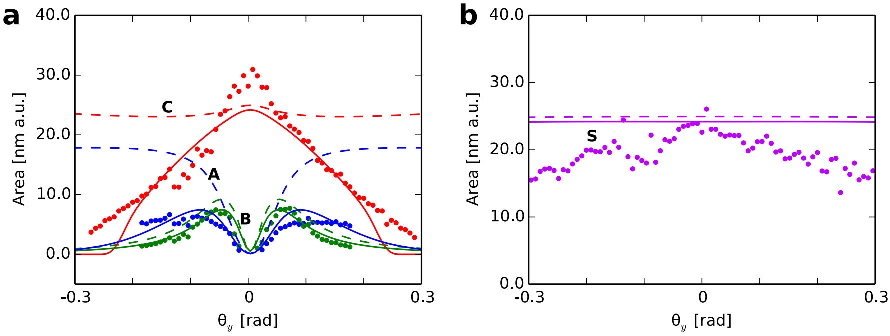

Figure 3.5: Integrated intensity of a) p-polarized and b) s-polarized bands. The points indicate the experimental values, whereas the curves indicate the predictions of the basic (dashed) and advanced (solid) model. Note the large integrated intensity of the bright C and S mode and the small integrated intensity of the dark A and B mode, in particular at $\theta = 0$.

$\theta = 0$. The field we are referring to is the parallel magnetic field, which is the field that scatters SPs to photons [37].

The model without a frequency dependent gain and fluorescence signal reproduces only the main features close to normal incidence, as shown by the dashed lines in Fig. 3.5. It predicts two bright and dark modes, and a M-shaped B band. The fit of the A and C band is improved considerably by including the spectral dependence of the gain and spontaneous emission, as shown with solid lines in Fig. 3.5. In this advanced model, the weak spontaneous emission and gain at short and long wavelengths limit the amount of light in the A and C band at large θ.

3.4.4 Different samples

We repeated these measurements and analyses on different metal hole arrays on the same wafer, with different hole sizes and spacings ($a_0 = 450...470$ nm). All arrays showed similar results, to be more precise: (i) the resonance frequency of the S band showed kinks that occur at the Rayleigh anomaly again, (ii) the spectral width of the two bright modes C and S was larger than that of the two dark modes A and B, and the spectral width of the S band suddenly increased between $\theta_y = 0.1$ and 0.25, and the spectral width of the B band was M-shaped, and (iii) the C and S bands were bright, while the A and B bands were dark at $\theta_y = 0$. There were also differences, one of them was in the width of the A band, which is now constant at small angles, before it increases towards larger angles. The onset of this increase is at the same angle as the kink in the resonance frequency of the A band and coincides with the Rayleigh anomaly.

Furthermore, we studied metal hole arrays with a similar spacing on a different wafer with a thicker (150 nm) active layer. These metal hole arrays did not have a perfect square lattice, but a slightly skewed (2°) parallelogram lattice. The most striking difference with the data presented in Figs 3.3-3.5 was a small bump in the angle dependence of the linewidth of the S band; the measured width of the S is identical to that of the C band at normal incidences, but decreases at $\theta_y = 0.05$. In addition, the resonance frequency of the S band was 4 nm blue-shifted compared to the C band.

3.5 Discussion

To verify that the loss rates and refractive index that are obtained from our model are reasonable, we compared them with theoretical values. The complex refractive index of surface plasmons on a smooth metal-semiconductor interface is

$$n_{eff} + in_i = \sqrt{\frac{\epsilon_1 \epsilon_2}{\epsilon_1 + \epsilon_2}} \tag{3.5.1}$$

where ϵ_1, ϵ_2 are the dielectric constant of the dielectric and the metal respectively. The ohmic loss rate is given by $\Gamma_r/\omega = n_i/n_{eff}$. For transparent InGaAs and InP as dielectric this leads to an expected ohmic loss rate $\Gamma_r/\omega = 0.0053$ and 0.0043 respectively[1]. The very thin SiN_x/InP layer next to the gold interface lowers this value to 0.0033 [20, 62]. Our reduced ohmic loss rate $\Gamma_R/\omega = 0.001$ is lower, which indicates that the InGaAs layer reduces the total loss and hence there is a net gain in the InGaAs layer. However, due to the ohmic losses and SP-to-photon scattering the SP-modes do not have net gain.

In ref. [19], Van Beijnum et al. determined the loss rate of the radiative SP mode around normal incidence, using Fano fits of measured transmission spectra which contained only the radiate modes S and/or C. Their analysis yield a half-width (HWHM) of 12 nm for the resonance around $\lambda = 1562$ nm at low pump power, which narrows to 4 nm at high pump power. The corresponding loss rates are $\Gamma_s/\omega = 0.0077$ and 0.0026, respectively. The loss rate of the unpumped system is considerably larger than our loss rates, while the loss rate of the pumped system is somewhat smaller, which can be explained by the lower temperature used in Ref. [19]. We expect an ohmic loss rate of $\Gamma_R/\omega \approx 0.036$ for the most absorptive case of unpumped bulk InGaAs.

Comparing the basic and advanced model with the data allows us to identify the frequency dependent gain and spontaneous emission as a dominant factor in the system. This frequency dependence depends on the exact shape of the electronic bands in the semiconductor, which might be more complex than our

---

[1] The following dielectric constants were used for the calculations of the expected loss rates: Gold: $\epsilon = -116 + 11.1i$. Transparent InGaAs: $\epsilon = 11.6$ ($n = 3.407$). InGaAs with absorption (gain):$\epsilon = 11.6 \pm 0.65i$. InP: $\epsilon \approx 9.61$ ($n \approx 3.10$). SiN: $\epsilon \approx 4$ ($n \approx 2$).

simple assumption made in eq. (3.3.2) and (3.3.3). Adding this to the model will increase the complexity and the number of fit parameters, and obscure the relevance of physical phenomena in the model.

3.6 Conclusion

We studied the complex dispersion relation of surface plasmons on a square metal hole array. We observed the frequencies, linewidths, and integrated intensities of the four resonances and compare our data to a simple model designed to identify the key ingredients. This model gives a quantitative prediction for both linewidths and intensities and captures all main features without introducing a large number of unknown parameters. The model necessarily misses some of the observed details. The most notable detail in the experiment are abrupt changes in the resonance frequencies and line widths which coincide with a Rayleigh anomaly.

The basic model is used to deduce the SP-to-photon scattering rate and the reduced ohmic losses. The SP-to-photon scattering rate is found to be approximately six times smaller than the backscattering rate, but is two times higher than the reduces ohmic losses for the applied pump power and temperature. We made a distinction between bright (radiative) and dark (non-radiative) modes. Furthermore we identified the frequency dependent gain as a dominant factor in our model, which should be included in any model of laser action. We augmented the model to include this dominant factor and retrieved improved predictions for both the intensity as the widths of the modes.

Acknowledgement

We acknowledge Frerik van Beijnum, Peter J. van Veldhoven and Erik Jan Geluk for their help in fabricating the samples at the COBRA Research Institute of the Technische Universiteit Eindhoven, The Netherlands.

Appendix

3.A Coupled mode model for SPs in square metal-hole-arrays

3.A.1 SP field in traveling-wave basis

In this appendix we describe a simple coupled-mode model for the surface plasmons (SP) that exist at the metal-dielectric interface of a square hole array. This model is an extension of an earlier model described in ref. [37]. It is based on the notion that photons emitted with parallel momentum $\mathbf{k}_{\|} \equiv (k_x, k_y)$ only couple to traveling-wave SPs with (in-plane) momenta $\mathbf{k}_{SP} = \mathbf{k}_{\|} + \mathbf{G}_{\mathrm{i}}$, where $\mathbf{G}_i$ is a lattice vector of the hole array. Our model only considers the four dominant Fourier components (modes), with magnitude $|\mathbf{G}_i| \equiv G = (2\pi/a_0)$ pointing in either of the four lattice directions $\{\mathbf{e}_x, \mathbf{e}_{-x}, \mathbf{e}_y, \mathbf{e}_{-y}\}$, and neglects higher-order Fourier components of the SP. These components are not resonant and hardly excited. The non-resonant contributions from all Fourier components are included in a change in the effective refractive index n_{eff}, which is different from the effective index of SPs on a smooth interface.

In this chapter, we only consider emission at $\theta_x = 0$ and write the parallel momentum $k_y = (\omega/c)\sin\theta_y$ at emission angles $\theta_y \ll 1$. We express the associated out-of-plane components of the SP field at position $\mathbf{r} \equiv (x, y)$ as

$$\begin{aligned}\mathbf{E}(\mathbf{r},t) = \big[&E_x(t)\mathbf{u}_x e^{iGx} + E_{-x}(t)\mathbf{u}_{-x}e^{-iGx}\\ &+E_y(t)\mathbf{u}_y e^{iGy} + E_{-y}(t)\mathbf{u}_{-y}e^{-iGy}\big]e^{ik_{\|}y},\end{aligned} \tag{3.A.1}$$

where $\{E_x, E_{-x}, E_y, E_{-y}\}$ are the modal amplitudes of the four traveling waves. The eigenvectors $\mathbf{u}_i$, which describe the four associated optical polarizations, are chosen to be rotationally-imaged copies of each other. When the four modal amplitudes in Eq. (3.A.1) are combined into a single vector $|E\rangle$, the time evolution of this SP field can be expressed as $d|E\rangle/dt = -iH|E\rangle$, where H is a 4×4 matrix. If scattering is neglected, H reduces to a diagonal matrix with elements $\{\omega_{+x}, \omega_{-x}, \omega_{+y}, \omega_{-y}\}$. At $\theta_x = 0$ and $\theta_y \equiv \theta$, the dispersion relation $\omega = |\mathbf{k}_{\|}|c/n_{eff}$ for traveling-wave SPs on a metal-dielectric interface yields $\omega_{\pm y}(\theta) \approx (G \pm k_{\|})c/n_{eff} \approx \omega_0 \pm c_1\theta$, and $\omega_x(\theta) = \omega_{-x}(\theta) \approx \omega_0 + c_2\theta^2$, with $\omega_0 \equiv (2\pi/a_0)c/n_{eff}$, $c_1 \equiv \omega_0/n_{eff}$, and $c_2 \equiv \omega_0/(2n_{eff}^2)$, where n_{eff} is the SP effective index.

Reference [37] also described the SP-to-SP scattering processes. This scattering was divided into three fundamental processes: forward scattering under 0° (at a rate γ_0), right-angle scattering under ±90° (at a rate κ), and backwards scattering under 180° (at a rate Γ). Inclusion of these scattering processes into the $d|E\rangle/dt = -iH|E\rangle$ matrix description yields the result presented in ref. [37]:

$$H = \begin{pmatrix} \omega_0 + c_2\theta^2 & \gamma & \kappa & \kappa \\ \gamma & \omega_0 + c_2\theta^2 & \kappa & \kappa \\ \kappa & \kappa & \omega_0 + c_1\theta & \gamma \\ \kappa & \kappa & \gamma & \omega_0 - c_1\theta \end{pmatrix} \tag{3.A.2}$$

The scattering rates γ and κ are assumed to be real-valued, such that the associated coupling is conservative (= energy conserving) and the matrix H is Hermitian. The reference frequency is again $\omega_0 = (2\pi/a_0)c/n_{eff}$, but n_{eff} now contains a small contribution from forward scattering at a rate γ_0.

3.A.2 SP field in standing-wave basis

Next, we transform the evolution matrix H from the traveling-wave to the standing-wave basis. For this purpose, we combine the waves traveling in the $\pm x$ direction into two standing waves with out-of-plane $E_{\perp}(\mathbf{r}) = E_{cx}(\mathbf{r}) \propto \cos Gx \cdot \exp ik_y y$ and $E_{sx}(\mathbf{r}) \propto \sin Gx \cdot \exp ik_y y$, where the labels cx and sx denote a cosine- or sine-pattern in the x direction. Likewise, we combine the $\pm y$ traveling waves into two standing waves with out-of-plane E-fields $E_{cy}(\mathbf{r}) \propto \cos Gy \cdot \exp ik_y y$ and

$E_{sy}(\mathbf{r}) \propto \sin Gy \cdot \exp ik_y y$. The transition from the $\{+x, -x, +y, -y\}$ traveling-wave basis to the $\{-i\sin Gx, \cos Gx, -i\sin Gy, \cos Gy,\}$ or $\{sx, cx, sy, cy\}$ standing-wave basis transforms the H matrix into

$$H = \begin{pmatrix} \omega_0 + c_2\theta^2 - \gamma & 0 & 0 & 0 \\ 0 & \omega_0 + c_2\theta^2 + \gamma & 0 & 2\kappa \\ 0 & 0 & \omega_0 - \gamma & \delta \\ 0 & 2\kappa & \delta & \omega_0 + \gamma \end{pmatrix}, \qquad (3.A.3)$$

where $\delta \equiv -c_1\theta = -(\omega_0/n_{eff})\theta$.

Note how the 4×4 matrix separates in an uncoupled element, associated with the sx standing wave, and a 3×3 matrix. This separation results from the mirror symmetry in the xz-plane ($\theta_x = 0$). The $E_{sx}(\mathbf{r}) \propto \sin Gx \cdot \exp ik_y y$ field is the only standing wave that is odd under mirror inversion, while the other three standing waves are even. The former couples only to s-polarized emission, which has an odd symmetry, while the latter three mix and couple to p-polarized emission, which also has an even symmetry. Also note how the coupling rate κ, associated with SP-SP scattering under 90°, only couples the $\cos Gx$ and $\cos Gy$ waves, which have intensity maxima at the holes, while the detuning δ only couples the cy and sy standing waves.

3.A.3 Losses and gain

Next, we include losses and gain in our model. First of all, we include ohmic losses at an ohmic damping rate $\Gamma_r = (n_i/n_{eff})\omega$, where n_i and n_{eff} are the imaginary and real part of the SP effective index $n_{eff} + in_i = \sqrt{\epsilon_1\epsilon_2/(\epsilon_1 + \epsilon_2)}$ at the interface between medium 1 and 2. Second, we include optical gain at a gain rate g_0 per second. As both ohmic loss and optical gain are distributed approximately uniformly, they can be combined into an effective ohmic loss rate $\Gamma_R \equiv \Gamma_r - g_0$ and are easily incorporated in our matrix description by replacing the evolution matrix $iH \rightarrow iH - \Gamma_R$. Finally, we include radiative losses through scattering from SPs to photons, either in the air or in the semiconductor. This radiative loss rate $\Gamma_{\text{rad}} = \Gamma_{air} + \Gamma_{semi}$ is equal for all traveling waves, but mode selective for the standing waves. As radiative scattering only occurs at the holes and as the SP-to-photon coupling proceeds dominantly via the in-plane magnetic field (at $\theta \ll 1$), we expect that only the standing waves with a sinusoidal $E_\perp$- pattern couple radiatively, at a decay rate $2\Gamma_{\text{rad}}$, while the cosine-type modes don't couple. By combining the above loss and gain rate into our matrix description we arrive at our final expression

$$H = \begin{pmatrix} \tilde{\omega}_{sx} & 0 & 0 & 0 \\ 0 & \tilde{\omega}_{cx} & 0 & 2\kappa \\ 0 & 0 & \tilde{\omega}_{sy} & \delta \\ 0 & 2\kappa & \delta & \tilde{\omega}_{cy} \end{pmatrix}, \qquad (3.A.4)$$

where $\tilde{\omega}_i = \omega_i - i\Gamma_i$ are four complex frequencies, with real parts $\omega_{sx} = \omega_0 + c_2\theta^2 - \gamma$, $\omega_{cx} = \omega_0 + c_2\theta^2 + \gamma$, $\omega_{sy} = \omega_0 - \gamma$, and $\omega_{cy} = \omega_0 + \gamma$, and imaginary parts $\Gamma_{sx} = \Gamma_{sy} = \Gamma_R + 2\Gamma_{\text{rad}}$ and $\Gamma_{cx} = \Gamma_{cy} = \Gamma_R$.

3.A.4 Spontaneous emission spectra

The fluorescence spectrum of the optically-pumped systems can be calculated in two steps, once the evolution matrix of the SP-field is known. In the first step, the spontaneous emission into the surface plasmon manifold is calculated from the expression

$$\frac{d}{dt}|E(t)\rangle = -iH|E(t)\rangle + |S(t)\rangle \quad \Rightarrow \quad |E(\omega)\rangle = -i(H-\omega)^{-1}|S(\omega)\rangle \,,$$

where the 4-element vector $|S\rangle$ describes the original spontaneous emission, divided over the four standing-wave SP modes, and $|E\rangle$ describes the generated SP field. The multiplication by $(H-\omega)^{-1}$ describes how the original emission source is modified by the gain and loss in the system into the resulting SP field, which therefore peaks around optical frequencies ω close to the complex poles of the matrix H. In the first step of the calculation, we assume that the original emission at each optical frequency is equally distributed over the four standing waves and that the four emitted fields are uncorrelated. This assumption is the Fourier equivalent of the statement that the original emission at different spatial positions is homogeneous, isotropic, and uncorrelated. The emitters are thus treated as classical noise sources with a strength that depends only on their excited-state and ground-state population, as was done in the analysis of spontaneous emission noise in semiconductor lasers [63]. In the second (and final) step, the generated surface plasmons are scattered into photons and detected. The sx standing SP wave scatters into s-polarized photons and only the sy standing SP wave is assumed to scatter into p-polarized photons.

The emission in the (odd) s-polarized mode is easily calculated. As only one of the four SP standing waves is odd, the SP field follows from the scalar relation $E(\omega) = iS(\omega)/(\omega - \tilde{\omega}_{sx})$ and its absolute square

$$I_{\text{s-polarization}}(\omega) \propto \frac{I_s(\omega)}{(\omega-\omega_{sx})^2 + \Gamma_{sx}^2} \,, \tag{3.A.5}$$

where $I_s(\omega) \longleftrightarrow |S(\omega)|^2$. We recognize the standard Lorentzian form, with its resonance frequency $\omega_{sx} \equiv \omega_0 + c\delta^2 - \gamma$ and its (HWHM) half-width $\Gamma_{sx} \equiv \Gamma_R + 2\Gamma_{\text{rad}}$. The excited sx mode emits efficiently from SP-to-photon, as this $E_{sx}(\mathbf{r}) \propto \sin Gx \cdot \exp ik_y y$ mode has a magnetic field $\mathbf{H}_{sx}(\mathbf{r}) \propto \cos Gx \cdot \exp ik_y y \mathbf{e}_y$ with anti-nodes at the holes.

A calculation of the (even) p-polarized emission is more complicated, as this emission originates from three coupled SP modes. After some straightforward mathematics, which involves the inversion of a 3 × 3 matrix and a projection onto the sy mode, which is the only one of the three mode that couples to photons, we obtain

$$I_{\text{p-polarization}}(\omega) \propto \sum_{i=1}^{3} \frac{I_s(\omega)\,|\langle sy|u_i\rangle|^2}{(\omega-\omega_i)^2+\Gamma_i^2} \tag{3.A.6}$$

where $\langle u_i|$ are the three left eigenvectors of the 3 × 3 lower-right submatrix $\tilde{H}$ of H, $\tilde{\omega}_i \equiv \omega_i + i\Gamma_i$ are the associated eigenvalues, such that $\langle u_i|\tilde{H} = \tilde{\omega}_i\langle u_i|$, and $|sy\rangle$ denotes the field of the sy mode. The explicit solution of this problem reads

$$I_{\text{p-polarization}}(\omega) \propto \frac{|(\tilde{\omega}_{cy}-\omega)(\tilde{\omega}_{cx}-\omega)-4\kappa^2|^2+\delta^2\left[|\tilde{\omega}_{cx}-\omega|^2+4\kappa^2\right]}{|(\tilde{\omega}_{sy}-\omega)\left[(\tilde{\omega}_{cy}-\omega)(\tilde{\omega}_{cx}-\omega)-4\kappa^2\right]-\delta^2(\tilde{\omega}_{cx}-\omega)|^2}\,I_s(\omega), \tag{3.A.7}$$

At $\delta = 0$ and $\kappa = 0$, we recover the expected result $I_{\text{p-polarization}}(\omega) = I_{\text{s-polarization}}(\omega) \propto I_s(\omega)/|\tilde{\omega}_{sy}-\omega|^2$.

The above expressions for the emitted spectrum contain subtleties that might go unnoticed in their present form, as they are related to the frequency dependence of some of its parameters. The spontaneous emission spectrum $I_s(\omega)$ and the associated stimulated emission or optical gain $g(\omega)$ will for instance depend on frequency. These effects are included in the advanced model used in the main text. To keep the description simple, and limited the number of fit parameters, we have not yet included the following two effects: (i) The SP-to-SP scattering rates γ and κ and the SP-to-photon scattering rate Γ_{rad} are expected to show a wavelength dependence, with Rayleigh-type scattering rates scaling as ω^n with $n \geq 6$, depending on the type of scattering [64], (ii) the appearance of a new diffraction order (Rayleigh anomaly) is expected to lead to a sudden increase in radiative loss at large angle.

Chapter 4

Measurement of the phase and intensity profile of surface plasmon laser emission

We study the near and far field radiation patterns of surface plasmon (SP) lasers in metal hole arrays and observe radially polarized vortex-vector laser beams in both near and far field. Besides the intensity profile, also the complementary phase profile is obtained with a beam block experiment, where we block part of the beam in the near field, measure the resulting changes in the far field, and retrieve the phase using an iterative algorithm. This phase profile provides valuable information on the feedback mechanisms and coherence of the laser and shows that our SP laser operates in a phase-slip mode instead of a pure dark mode. To explain our observations, we extend the standard model for distributed feedback (DFB) lasers by introducing a position dependence in the optical gain and refractive index.

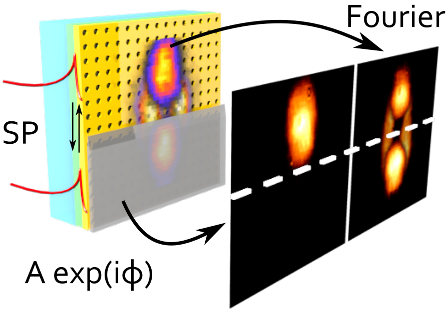

This chapter was previously published as:
V. T. Tenner, M. J. A. de Dood, and M. P. van Exter, *Measurement of the Phase and Intensity Profile of Surface Plasmon Laser Emission*, ACS Photonics **3**, 942 (2016)

4.1 Introduction

Optically coherent laser radiation can be generated if both gain and optical feedback are present in a medium. Our physical understanding of these phenomena originates from comparisons between measured intensity distributions and models of both the amplitude and the phase of the radiation. The optical phase is typically discarded because it evolves too fast to resolve directly with an optical detector or a camera. The inability to measure both amplitude and phase of the emitted laser radiation presents a recurring challenge in optics and limits progress in the field.

More ingenious schemes are needed to observe the phase using slow detectors. One of the simplest schemes uses the mixing of the amplitude and phase information of the light field upon propagation. At the laser exit the amplitude contains information where the light is emitted, while the phase profile contains information about the propagation direction. Recording the intensity distribution on different positions allows retrieval of the phase information by an iterative algorithm [66–68].

The ability to resolve both amplitude and phase is particularly relevant for lasers that emit non-standard beam profiles that are not yet fully understood. Examples of such lasers are surface-emitting distributed feedback lasers, such as photonic and plasmonic crystal lasers. Two-dimensional surface-emitting photonic-crystal-lasers often emit donut beams with azimuthal polarization [69], while surface plasmon lasers create radially polarized vector-vortex beams [20]. Devices can be tailored to emit other beam shapes [70], but information about the phase- and amplitude profile is scarce and has either low resolution [71] or an electrical contact blocks the view [72].

A better understanding of gain and feedback in plasmonic systems is important for improving photonics applications that use the strong confinement and light-matter interaction provided by plasmons. These applications include ultra sensitive molecule sensors (SERS) [3], anti-counterfeiting measures [73], perfect absorbers [74], ultra-fast optical modulators [75], as well as future metal-dielectric metamaterials consisting of arrays of plasmonic sub-wavelength elements [5, 6]. The strong plasmonic response of passive media is accompanied by Ohmic loss due to scattering of the free electrons in the material. Adding media with active gain can resolve this issue [19, 76, 77] and over-compensation typically leads to laser action, as has been demonstrated in two-dimensional metal particle arrays [28], and metal hole arrays [20].

In this chapter, we present the first experimental observation of the phase- and amplitude profile of a two-dimensional surface plasmon laser retrieved via the combination of a beam-block experiment and an iterative algorithm. The metal hole array in our study acts as a second order Bragg grating, which provides a natural output channel and enables easy observation of the intracavity field. Our observations go beyond the standard description of distributed feedback lasers. We extend the standard approach by including a position dependent gain and

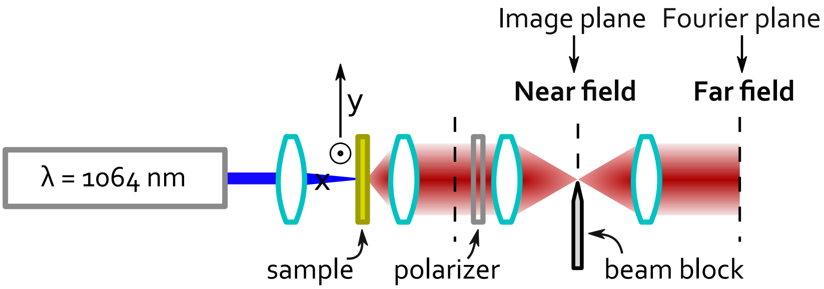

Figure 4.1: Schematic of the experimental setup to measure the amplitude and phase profile of the laser emission.

refractive index, which are both induced by the optical pump beam, and obtain good agreement between experiment and theory.

4.2 Device

The semiconductor-gold samples that we study contain metal hole arrays with a square lattice, with hole diameters of 160 nm and a lattice spacing of 470 nm (see Fig. 4.2a for a SEM image). The device dimensions studied here are 50x50 and 100x100 μm. The Au film is 100 nm thick and is deposited on a 127 nm $In_xGa_{1-x}As$ ($x = 0.536$) gain layer on an InP substrate (see Fig. 4.2e for a schematic side cut). Between the gold and the InGaAs, a thin InP spacer layer and a SiN passivation layer were incorporated. The gain layer is sufficiently thin such that the only supported optical mode is the surface plasmon (SP) mode. Similar samples are described in more detail in ref [20].

4.3 Experiment

Our experimental geometry is as shown in Fig. 4.1. The sample is mounted in a cryostat with optical access on both sides and cooled down to 80 K. We pump the active layer of the sample using a continuous wave laser with a wavelength of 1064 nm through the transparent InP substrate. The pump beam has a Gaussian profile that can be varied in size between 20 and 50 μm full width at half maximum. The light emitted by the SP laser is collected in transmission on the metal side of the device with a 20x microscope objective (NA = 0.4) combined with a tube lens (f = 200 mm) to create a 4-f imaging system. Hence, the optical field in the image plane is a scaled version of the radiative field at the sample; in this thesis, we call this the near field.

In some of the experiments we position a razor blade in the near field to block part of the beam. To inspect the near field, we image it with a lens (f = 100 mm) on a CCD camera. Subsequently, this lens is replaced by a lens with a longer focal distance (f = 200 mm) such that the far field is retrieved in the back-focal plane. A bandpass filter ($\lambda = 1490 \pm 6$ nm) that transmits the laser light is used to reduce the broadband spontaneous emission in the measurements.

4.4 Results

Figure 4.2 show the measured near field (top) and far field (bottom) of the SP laser. Images are shown for the unpolarized light (b,f), with a linear polarizer transmitting y-polarized light (c,g) and with half of the near field blocked (d,h). The near field is donut shaped, i.e. it is circular with a dark center. The laser area is comparable to the size of the pump, being 40 μm in this case. The dark central spot is remarkable and raises questions about the apparent lack of energy in the center of the device. Figure 4.2c shows a polarization resolved measurement. Since this image rotates along when rotating the polarized axis, we conclude that the near field donut is radially polarized. The observation of a clear donut in the near field is only apparent when the pump beam is small enough. In our experiments, we observe that larger pump beams (up to 100 μm) result in a larger laser areas and spatial inhomogeneity. Nonetheless, there is always a dark spot somewhere, as expected for a topological defect. Under some experimental conditions the laser hops between several spatial modes with different locations of the dark spot, and hence the central dark spot becomes less visible after averaging.

Figures 4.2f-h show the observed far field intensity profiles and display that the far field is also a radially polarized donut beam. This similarity is not trivial and warrants further investigation. In order to observe the associated phase profile, we perform an experiment in which we block half of the near field with a razor blade and observe the far field. The resulting near field, shown in Fig. 4.2d, is trivial and presented mainly for didactic reasons. The resulting far field, shown in Figure 4.2h, depicts that the two lobed far field is now reduced to a single lobe, while the angle of the maximum emission is hardly changed. This observation provides valuable information about the phase profile of the near field, because it indicates the existence of a phase gradient in the near field.

To quantify the full two-dimensional phase profile of the optical field, we retrieve the phase profile with an iterative Gerchberg-Saxton-based algorithm [66], see Methods. We find that the retrieved near field phase exhibits a π-phase jump in the dark center of the device and exhibits a phase gradient in the radial direction, with a slope that increases towards the edge of the device. A cross section of this phase profile is depicted in Fig. 4.3c,g. These figures also show cross sections of the near and far field intensity profiles presented earlier in Fig. 4.2. The far field of the full beam has no light in the center, whereas there is emission along the surface normal in the beam block experiments. Because the far field of the full beam should be equal to the coherent sum of the two halves, the dark center in the far field must be formed by interference of emission from the two halves of the sample. This in turn indicates the existence of long range coherence across the sample. In the rest of this chapter we will discuss the implications of our observations and compare

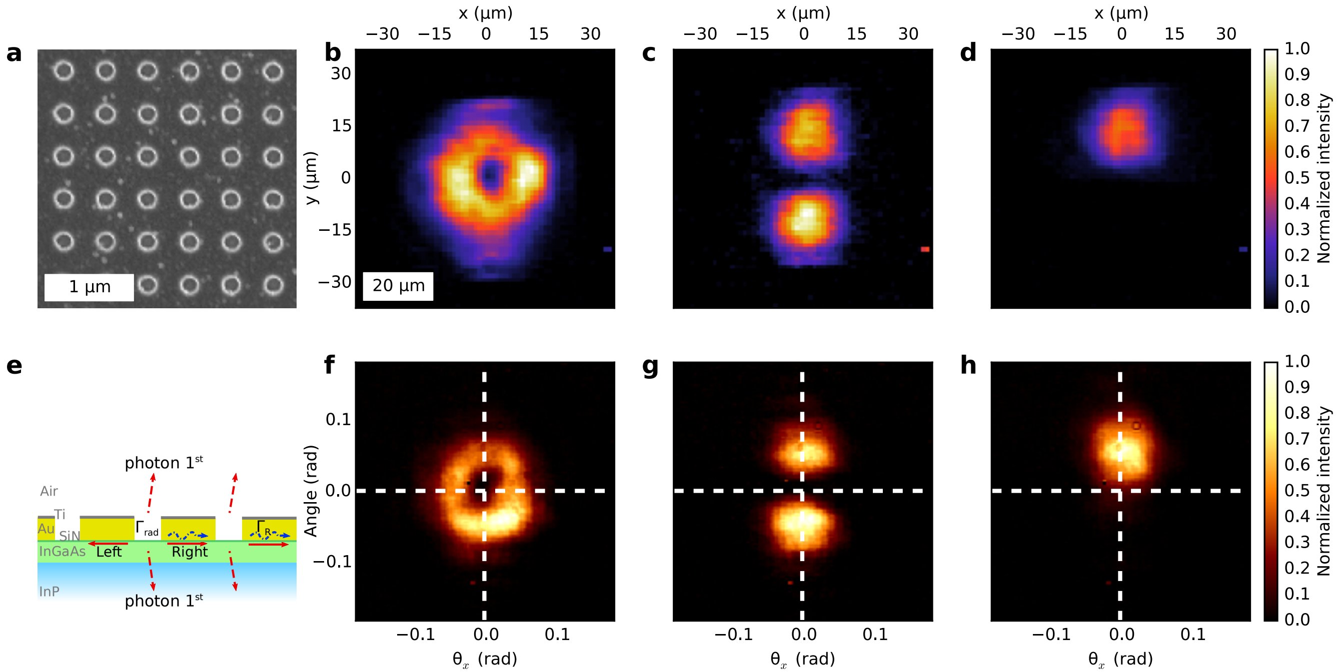

Figure 4.2: Our SP-laser and its emission, measured in near and far field. (a) Scanning electron microscopy image of the metal hole array. (e) Cross section through the sample, indicating the layer-stack, the left and right traveling waves and the emitted light. (b-d) Near field and (f-h) far field intensity profiles of a surface plasmon laser. (b,f) Show the donut shaped beams in both near and far field. (c,g) Show profiles observed behind a polarizer that transmits vertically polarized light. (d,h) Show what happens when we block the lower part of the near field. Vertical cross sections are shown in Fig. 4.3(c,g).

them with theory.

4.5 Discussion

We first compare our results with the standard DFB theory [35] for one dimensional systems with a finite size. In this theory, the field in the device is decomposed in two traveling waves, which are coupled by scattering at the holes. The relevant parameters are the length L of the device and the coupling rate κ. The product κL determines the behavior of the laser. This theory yields the threshold condition of the laser: wavelength, gain and the field profiles of the traveling waves.

The solutions are either symmetric or anti-symmetric around the center of the device. In an infinitely large index coupled system these are dark (non-radiating) and bright (radiating) modes, which are located at the exact center of the Brillouin-zone ($k = 0$) [37, 51, 78]. However, in a “real” laser, the coherence length ℓ_{coh} is limited by the finite sample size and the scattering [35], which breaks the description of a continuous band structure into discrete modes with a detuning from the Bragg wavelength. The relevant modes are at $\Delta k = \pi/\ell_{coh}$ and there is no mode at the center of the Brillouin-zone.

Scattering in the out-of-plane direction induces radiative loss, which increases the threshold of the radiative solution [79]. Our device operates in a transverse-magnetic (TM) mode and hence the coupled mode with the symmetric out-of-plane E-field distribution is the non-radiating mode with the lowest threshold, as explained in Appendix 4.A.

Figure 4.3a,b displays the calculated symmetric coupled mode solution of the standard DFB theory for our measured backscatter rate $\kappa/\beta_0 = 0.012$ [37], device length $L = 50\,\mu\text{m}$, and refractive index $n_0 = 3.268$ [52], corresponding to $\kappa L = 8$. The calculated near field shown in Fig. 4.3a contains the essential features of Fig. 4.3c: it has two lobes with opposite sign, indicated by a π-phase-jump in center of the device. However, in contrast to the experiment the calculated phase in each of the lobes is almost constant. As a consequence, the far field profiles depicted in Fig. 4.3e are very different from the observations depicted in Fig. 4.3g: the calculated profile is too narrow and is oscillatory at larger angles. Furthermore, the emission by half of the device is incorrectly predicted to be a single lobe located close to the surface normal.

To explain our observations we extend the standard DFB theory by introducing a position dependence of the gain and refractive index (see Appendix 4.A for derivation). Both are mainly set by the carrier density, which is position dependent due to inhomogeneous pumping and diffusion, and to a lesser extent by the local temperature associated with heating of the device. We model the local gain and index as the Gaussian profile of the pump beam, and note that deviations from an exact Gaussian shape are unimportant. In the center of the pumped area there is an effective gain, as discussed below, while outside the pumped area there is an effective loss (negative gain), which is mainly caused by absorption in the gain

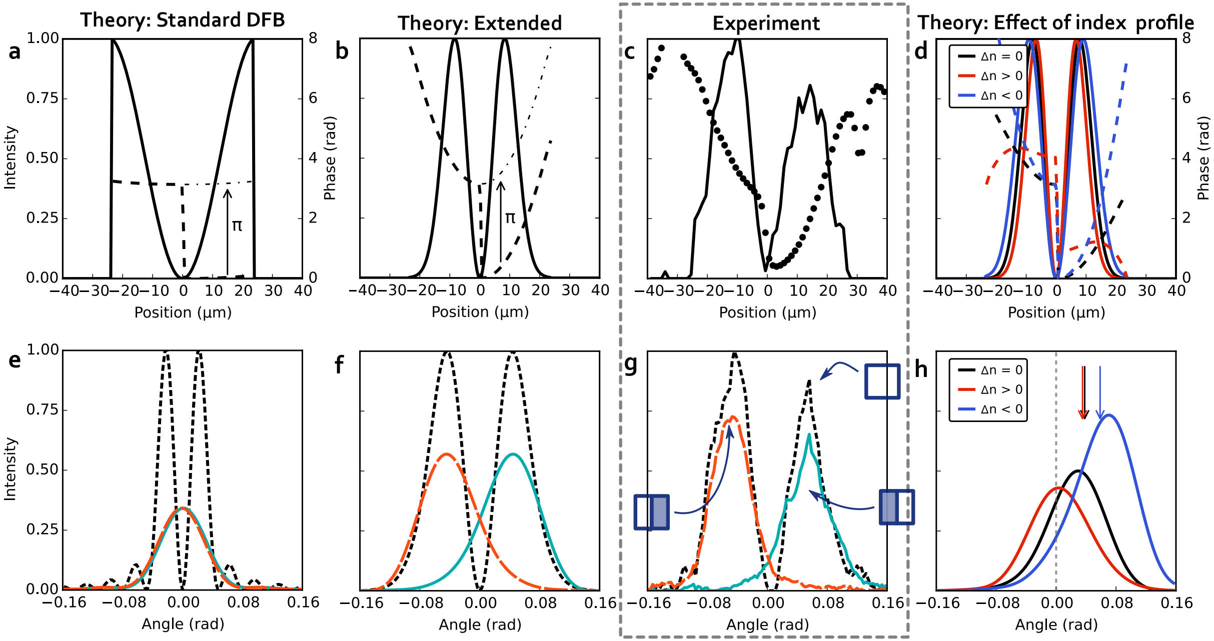

Figure 4.3: Cross sections through the center along the vertical direction of the (a-d) near field and (e-h) far field. In (a-d), the solid lines show the intensity envelope and the dashed lines show the phase of the near field. To stress the symmetry in (a,b), a π-shifted copy of the phase is displayed as a dashed-dotted line. In (e-h), the dashed curves show the far field intensity profiles of the full beam, while the colored curves show the resulting far fields when blocking the right (red dashed) or left (blue solid) half of the near field. The framed figures (c,g) are the experimental data taken from Fig. 4.2 and the reconstructed phase of the near field. The other figures are based on theory: (a,d) Standard DFB theory with uniform gain and index, (b,f) extended theory that includes a position dependent gain and refractive index, (d,h) extended theory with variations in the magnitude of the index profile. Note that (h) only displays the far field for one blocking condition. The arrows indicate the opening angle of the beam without beam block.

layer. We solve the coupled mode equations by an active mirror approach [63], which is relatively simple and powerful, as explained in Appendix 4.A. The resulting fields at the threshold are shown in Fig. 4.3b,f. The phase in the near field now increases towards the edge of the samples, very comparable to our measurements. Hence, also the far field profiles of the beam block experiment are very similar to our observations: the maxima are now at the same angle as the lobes of the full beam.

Figure 4.3d,h illustrates the predicted effect of index guiding and anti-guiding on the laser, with a Gaussian gain and index profile, with $\Delta n = 0$, $\Delta n = +0.13$, and $\Delta n = -0.13$ between the pumped center and the unpumped edges. The differences are best visible in a beam block experiment (see Fig. 4.3h), where the angle of the maxima of the lobe moves inwards for $\Delta n > 0$ and outwards for $\Delta n < 0$. The near fields depicted in Fig. 4.3d show index guiding for $\Delta n > 0$, and index anti-guiding for $\Delta n < 0$. This guiding can also be interpreted as a plasmonic bandgap with spatial dependence [80, 81]. Our experimental data can be best fitted with $\Delta n = -0.05$, which is consistent with the typical refractive index changes of pumped bulk material [82].

The gain profile, in contrast to the index profile, leads to guiding, because the effective gain in the center of the pumped area is higher than its surroundings. The gain and loss used in the model have realistic values: The unpumped areas have an effective intensity loss of [52] $\approx 3000\,\mathrm{cm}^{-1}$. At the threshold, the net gain in the center is $\approx 340\,\mathrm{cm}^{-1}$. The required material intensity gain is the sum of the net gain and the Ohmic loss of our device with transparent InP [52] ($270\,\mathrm{cm}^{-1}$), divided by the confinement factor in the gain layer [19] (0.32) and it is around $2000\,\mathrm{cm}^{-1}$, which is a reasonable number for a semiconductor operated at high carrier densities [38, 83].

For completeness we note that we have used a one-dimensional model to describe a two- (or even three)-dimensional system. Hence the derived numbers may differ somewhat from reality. From literature on DFB theory in two dimensions [84, 85], we expect that the influence of such 2D coupling on the derived numbers is rather low in our system, because it already operates in the overcoupled regime and the 2D coupling is small compared to the 1D coupling. In earlier work [37, 52] we measured $k_2/k_3 \approx 0.3$, where k_2 and $k_3 = \kappa$ are the scattering rates of respectively 90° and 180° scattering [84]. This extra coupling will only marginally change the detuning [85] and threshold [84]. Other authors have extended the standard DFB theory to two dimensions to answer the question under which conditions the symmetric mode can lase [86]. These analyses confirm that 2D DFB lasers are expected to emit donut shaped beams.

4.6 Conclusion

This chapter reports the first measurement and reconstruction of the phase and the amplitude of surface plasmon laser emission. Our two-dimensional plasmonic-crystal emits donut-shaped and radially-polarized light, both in the near field and in the far field. By blocking half of the laser emission we retrieve the phase of the emission and demonstrate the existence of long range coherence and lasing in a symmetric non-radiative mode. Our observations cannot be explained with the standard DFB theory, which assumes a device with uniform properties. We extend this theory by introducing position dependence of the gain and refractive index and find good agreement with our measurements on surface-emitting DFB lasers. This provides the following three insights: First, due to the round trip phase condition, the laser is in a phase-slip mode and not in a dark mode and hence the laser can radiate. Second, we attribute the lack of emission in the center of the near field interference between in-plane counter-propagating waves. Third, the central zero in the far field also results from the symmetry of the lasing mode and demonstrates the existence of long range coherence over the full sample.

Our results demonstrate a powerful method to analyze surface-emiting lasers. This method can also be deployed on surface plasmon lasers with other lattice symmetries or on photonic-crystal lasers in order to understand and improve their characteristics. Furthermore, our results indicate that much of the current knowledge about one- and two-dimensional photonic-crystal lasers can be applied to understand and improve surface plasmon lasers.

4.7 Methods

The phase of the fields is retrieved with an iterative Gerchberg-Saxton-based algorithm [66–68]. The near and far field measurements are used as support for the algorithm. The phase is retrieved for 3 sets of conjugate measurements in parallel: (i) the full polarization resolved measurements shown in Fig. 4.2c,g and measurements with either a blocked (ii) bottom (Fig. 4.2d,h) or (iii) top (measurements not shown). Every 5th iteration, the reconstructed phase of alternately the bottom or top part is applied on the full near field reconstruction. After 30 iterations, we end with 10 iterations on the full fields. The algorithm convergences and is stable to noise.

Acknowledgement

The authors thank Dirk E. Boonzajer Flaes for his discussions about the iterative algorithm, Matthias Saba for his discussions about surface plasmon lasers, and Peter J van Veldhoven and Erik Jan Geluk for their help in fabricating the samples at the COBRA Research Institute of the Technische Universiteit Eindhoven, The Netherlands. This work is part of the research program of the Foundation for Fundamental Research on Matter (FOM), which is part of the Netherlands Organization for Scientific Research (NWO).

Appendices

4.A Distributed feedback theory with a position dependence of the gain and refractive index

In this supplement, we derive a coupled mode theory that extends the standard DFB theory with a position dependence of the gain and refractive index. We explain how the equations can be solved both in the time domain and the spatial domain and compare them with previous efforts. We solve the equations with an active mirror approach and demonstrate that this method is very flexible and fast.

The temporal and spatial evolution of the optical field in a one-dimensional distributed feedback (DFB) structure can be derived from the optical wave equation by using the slowly-varying approximation. This derivation can be found in many text books [35, 82] and only the main results for a device with a second-order Bragg grating and TM polarized mode are stated here. We express the optical field as the sum of a rightward R and leftward S traveling wave and write each of them as a slowly-varying envelope multiplied by a reference wave [35]:

$$E(x;t) = [R(x,t)\,e^{i\beta_0 x} + S(x,t)\,e^{-i\beta_0 x}]e^{-i\omega_0 t}, \tag{4.A.1}$$

where ω_0 is the reference frequency. The reference wave vector $\beta_0 \equiv 2\pi/\Lambda = n_0\omega_0/c$ is fixed by the lattice spacing Λ, and is linked to the reference frequency via the reference index n_0. The dielectric constant is expanded in Fourier components and the resulting terms are sorted. The resulting dimensionless coupled-mode equation that describe the temporal and spatial evolution of the envelope functions R and S is:

$$\frac{1}{\omega_0}\frac{\partial}{\partial t}R + \frac{1}{\beta_0}\frac{\partial}{\partial x}R = \left(i\frac{\Delta n(x) - i\alpha(x)}{n_0} - \frac{\kappa_{\text{out}}}{\beta_0}\right)R + \left(\frac{i\kappa_{\text{back}} + \kappa_{\text{out}}}{\beta_0}\right)S \tag{4.A.2}$$

$$\frac{1}{\omega_0}\frac{\partial}{\partial t}S - \frac{1}{\beta_0}\frac{\partial}{\partial x}S = \left(i\frac{\Delta n(x) - i\alpha(x)}{n_0} - \frac{\kappa_{\text{out}}}{\beta_0}\right)S + \left(\frac{i\kappa_{\text{back}} + \kappa_{\text{out}}}{\beta_0}\right)R \tag{4.A.3}$$

The slow changes in the complex index $\hat{n} = n_0 + \Delta n(x) + i\alpha(x)$ are parameterized by the dimensionless gain $\alpha(x)$ and refractive index difference $\Delta n(x)$, which both have a gradual position dependence. The gain is related to the material intensity gain $g\,[\text{cm}^{-1}]$ via $\alpha(x) = g(x)n_0\Lambda/4\pi$. Fast changes in the complex index are governed by higher-order Fourier components, as discussed below. Dispersive effects are neglected ($\omega\frac{\partial n}{\partial\omega} \ll n$). The two counter propagating waves are coupled by scattering at the periodic corrugations with backscatter coupling parameter κ_{back}. This scattering also induces dissipative out of plane coupling κ_{out}.

The coupling κ_{back} and κ_{out} are related to Fourier components of the corrugation [82, 84, 87]. For a 2nd order DFB, the backscatter is relatively simple and is given by the second order ($2\beta_0$) Fourier component. The output coupling is related to the first (β_0) component in a more complicated way; it induces radiative loss of the energy of the R and S modes and κ_{out} depends approximately on the square of the first Fourier component.

The radiative loss and coupling induced by the out-of-plane scattering is most easily understood in the standing wave basis with the symmetric $R+S$ mode and the anti-symmetric $R-S$ mode. For a transverse-magnetic (TM) polarized mode, R and S denote the out-of-plane component of the E-field. The emission from the device depends on the in-plane fields, which are out-of-phase with the out-of-plane E-field[37]. Hence, the symmetric $R+S$ mode is a dark mode without loss, with anti-nodes in the out-of-plane E-field at the holes, while the anti-symmetric $R-S$ mode is radiative and experiences double radiative losses [37, 79, 84, 87]. This is mathematically described by the four coupling terms κ_{out} in Eqs. (4.A.2) and (4.A.3).

There are two different approaches to solve Eqs. (4.A.2)-(4.A.3): either in the time domain or in the space domain. In chapters 2, 3, and 5 we considered the *time dynamics of the Bloch modes of an infinitely large system* and labeled these modes by the angle θ at which they emit to free space, i.e. we set $\frac{\partial}{\partial x}R = k_0\theta R$ and $\frac{\partial}{\partial x}S = k_0\theta S$, where $k_0 = \omega_0/c$ is the wave vector in air. This yields the bandstructure of the crystal [37, 52] and was used to determine the dimensionless coupling rates $\kappa_{\text{back}}/\beta_0 = \gamma/\omega_0$ and $\kappa_{\text{out}}/\beta_0 = \Gamma_{rad}/\omega_0$.

Equations (4.A.2)-(4.A.3) can also be solved in the spatial domain, by looking for *the stationary eigenmodes of a finite-size system* at the laser threshold, i.e. the modes that vary in time as $\exp(-i\omega t)$, where $\omega \equiv \omega_0 + \delta\omega$ such that $\frac{\partial}{\partial t}R = -i\delta\omega R$ and $\frac{\partial}{\partial t}S = -i\delta\omega S$. The change of the fields over one unit cell can now be described by:

$$\Lambda\frac{\partial}{\partial x}\begin{pmatrix} R \\ S \end{pmatrix} = 2\pi\Bigg[(i\frac{\delta\omega}{\omega_0} + i\frac{\Delta n(x) - i\alpha(x)}{n_0})\begin{pmatrix} 1 & 0 \\ 0 & -1 \end{pmatrix} - i\frac{\kappa_{\text{back}}}{\beta_0}\begin{pmatrix} 0 & 1 \\ -1 & 0 \end{pmatrix} - \frac{\kappa_{\text{out}}}{\beta_0}\begin{pmatrix} 1 & -1 \\ 1 & -1 \end{pmatrix}\Bigg]\begin{pmatrix} R \\ S \end{pmatrix} \quad (4.A.4)$$

We solve Eq. (4.A.4) by launching a traveling wave in the center of the device and calculating its reflection amplitude on one half of the device [63]. In order to find the envelope of the field, we discretize the device on a grid with spacing Λ. In this active mirror approach, the propagation over one lattice spacing is given by

$$\begin{pmatrix} R(x_i+\Lambda) \\ S(x_i+\Lambda) \end{pmatrix} \approx \left(\boldsymbol{I} + \Lambda\frac{\partial}{\partial x}\right)\begin{pmatrix} R(x_i) \\ S(x_i) \end{pmatrix} = \mathbf{M}_{x_i}\begin{pmatrix} R(x_i) \\ S(x_i) \end{pmatrix} \quad (4.A.5)$$

and the transfer matrix of one half of the device is:

$$\mathbf{M}_{\text{half}} = \prod_{x_i=L/2}^{x_i=0}\mathbf{M}_{x_i} = \begin{pmatrix} M_{00} & M_{01} \\ M_{10} & M_{11} \end{pmatrix} \quad (4.A.6)$$

where L is the length of the device. As there is no input from outside the device

$$\begin{pmatrix} R(x=\frac{L}{2}) \\ S(x=\frac{L}{2}) \end{pmatrix} = \begin{pmatrix} t \\ 0 \end{pmatrix} \mathbf{M}_{\text{half}} \Rightarrow \begin{pmatrix} R(x=0) \\ S(x=0) \end{pmatrix} = \mathbf{M}_{\text{half}} \begin{pmatrix} 1 \\ r \end{pmatrix} \tag{4.A.7}$$

where r is the reflection and t is the transmission of half of the device. At the laser threshold, the round trip through the device is stable, hence $|r| = \left|-\frac{M_{10}}{M_{11}}\right| = 1$. The sign of r gives the symmetry of the mode.

We search for the detuning $\delta\omega$ and gain $\alpha(x)$ for the threshold condition of the symmetric mode by minimizing $1-r$ with a Powell hybrid method. Both the refractive index change $\Delta n(x)$ and gain $\alpha(x)$ are taken to have a Gaussian profile with the size of the pump beam. The gain $\alpha(x) = \alpha_{\text{absorption}} + \alpha_{\text{pump}}(x)$ consists of a negative baseline, due to absorption in the unpumped areas, and is more positive in the pumped center. This amplitude of the gain due to pumping is varied to find the threshold condition. For the best fit we take $\Delta n(x)$ negative in the center of the pump beam and zero in the unpumped areas. A discussion about the exact amplitude of the index and gain profiles is included in the main text. Note that the radiated field is proportional to the asymmetric combination $R-S$, as discussed before.

The described transfer matrix method proved to be very powerful; it is not only useful to find the threshold conditions [88], but it can also be extended to calculate the mode spectrum below threshold, to provide insight in noise in the system [63, 89], and to study the occurence of spatial hole burning [90].

4.B Retrieval of the phase of light

Measuring the phase of light is a non-trivial task, because electronic detectors, such as photo diodes and CCDs, are to slow to operate at optical frequencies ($\sim 400\,\mathrm{THz}$). The phase of the light encodes the direction in which the light travels [91]. When both the phase and the intensity of monochromatic light are known, also its trajectory in the forward and backward directions are known. When propagating, the information in the phase and intensity mixes. This can be scrutinized to obtain the phase: after measuring the intensity at different distances, the phase information can be retrieved by Gerchberg-Saxton-like iterative algorithms [66].

Figure 4.4 schematically depicts a Gerchberg-Saxton-like iterative algorithm which we used to retrieve the phase information from intensity measurements at different distances [92, 93]. In our case, these locations are at an image plane of the near and the far-field of the sample. The propagation of the light between these two planes can be described by a Fourier transform. The phase is retrieved by numerically propagating between both planes and applying the measured information. This goes in successive steps: the measured intensity of the near field is combined with the best known near-field phase and propagated to the far field. Now, the intensity information is mixed with the phase, and a better phase estimation is obtained, while the propagated intensity contains less information. The propagated intensity is replaced by the measured intensity in the far field, and is propagated back to the near field plane. Again, the intensity and phase are mixed and a better phase

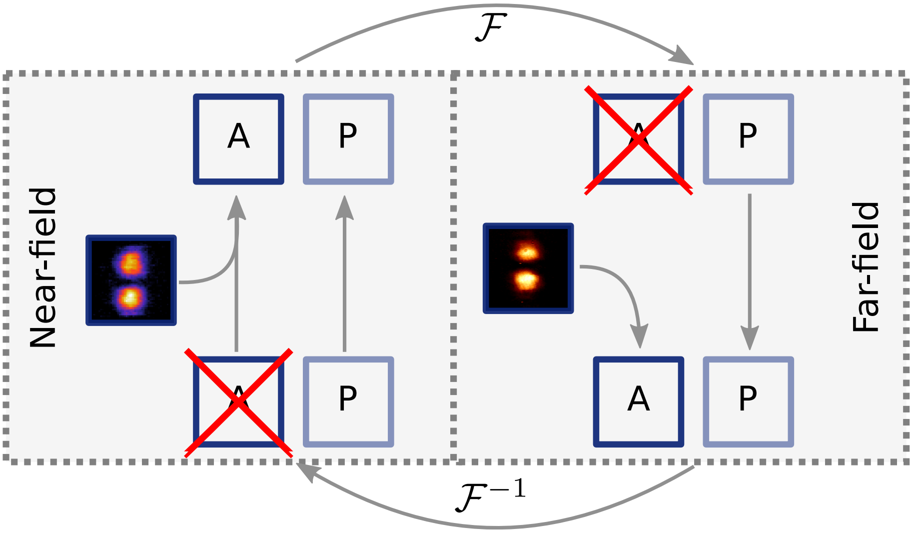

Figure 4.4: Schematic overview of iterative phase retrieval algorithm.

estimation is obtained. A good estimate of the phase is retrieved after several of such iterations [94].

This algorithm convergences after typically 50 iterations for our measurements. The first iteration is bootstrapped with a random phase pattern. In order to avoid local minima in this optimization procedure, the algorithm is run for 100 initial random phases and these results are averaged.

Faster and more reliable convergence can be obtained when more information about the sample is employed. In our case, we use the beam-block measurements to obtain a better first phase estimation as input for the final algorithm. This first phase estimation is obtained by running the algorithm with different intensity inputs in successive iterations. The near- and far-field measurements with the beam-block selecting in following places are used as inport: center, top, left, bottom, and right. This is sequence is repeated five times, and finalized with 10 iterations of the center measurements only. This reduces both the required number of iterations and increases the output stability.

Chapter 5

Surface plasmon dispersion in hexagonal, honeycomb and kagome plasmonic crystals

We present a systematic experimental study on the optical properties of plasmonic crystals (PlC) with hexagonal symmetry. We compare the dispersion and avoided crossings of surface plasmon modes around the Γ-point of Au-metal hole arrays with a hexagonal, honeycomb and kagome lattice. Symmetry arguments and group theory are used to label the six modes and understand their radiative and dispersive properties. Plasmon-plasmon interaction are accurately described by a coupled mode model, that contains effective scattering amplitudes of surface plasmons on a lattice of air holes under 60°, 120°, and 180°. We determine these rates in the experiment and find that they are dominated by the hole-density and not on the complexity of the unit-cell. Our analysis shows that the observed angle-dependent scattering can be explained by a single-hole model based on electric and magnetic dipoles.

This chapter was previously published as:
V. T. Tenner, M. J. A. de Dood, and M. P. van Exter, *Surface plasmon dispersion in hexagonal, honeycomb and kagome plasmonic crystals*, Optics Express **24**, 29624 (2016)

5.1 Introduction

The interaction between surface plasmons (SPs) and nano-structures is an active field of research [3, 6, 8, 77, 96, 97]. For instance, lattices of such nanostructures form optical meta-materials [5, 6]. Such materials can be designed and engineered despite the fact that the interaction with a single sub-wavelength circular nanohole in a gold film cannot be described accurately using simple theory. Near-field experiments on a single isolated hole provided more insight in such SP-hole scattering process [50], but leafs questions about the interaction between holes and the size variations that occur in arrays unaddressed. In this chapter we study 10^4 holes simultaneously and retrieve more accurate information on the scattering process of individual holes than what is possible with single hole experiments.

The sub-wavelength holes are placed in a periodic crystal and a built-in light source is used to excite SPs directly. We study hexagonal, honeycomb, kagome and square lattices with similar holes. Metal-hole arrays with a square lattice and an active layer show SP-laser action [20]. The question arises how lattices with hexagonal symmetry affect such laser action. While the square lattice is two-dimensional, the observed intensity and phase of the laser beam can be described by a one-dimensional model [65]. Hexagonal lattices are intrinsically two-dimensional; their lattice vectors are not orthogonal and a two-dimensional model is necessary. A first step in this process is to determine the SP-bandstructure of such hexagonal based lattices, where the scattering properties of a single hole form a key ingredient.

In photonic crystals, the relation between bandstructure and unit cell can be described as a function of hole size and refractive index contrast. For plasmonic crystals based on nano-holes, no such relation is known, although it would greatly simplify the design process. We demonstrate that such relation also exists for metal hole arrays.

In this chapter, we present accurate information about the scattering properties of individual sub-wavelength holes obtained from lattices of nano-holes. We compare plasmon scattering in square and hexagonal-based lattices, and hexagonal-based lattices with different unit cells. In the experiments, the hole size and the symmetry of the lattice and unit-cell are kept constant, while the complexity in the unit cell is increased. We show measurements of the dispersion relations around the Γ-point, present a didactic interpretation in terms of traveling waves, symmetries and group theory, and show that the observed bands are accurately described by a coupled-mode model. This model yields effective amplitudes for surface plasmons scattering on a lattice of air holes under angles of 60°, 120°, and 180°. These scattering rates can be explained by a microscopic model for SP-scattering on a single hole.

5.2 Methods

The samples that we study consist of metal hole arrays with three different unit-cells. All 50 × 50 μm arrays consists of holes with diameters of 160 nm and a

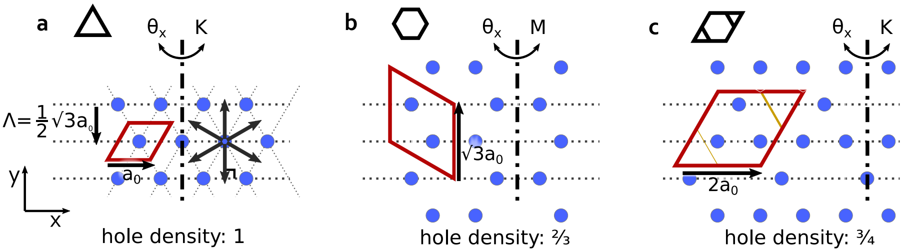

hole density: 1

hole density: ⅔

hole density: ¾

Figure 5.1: Three different real space lattices and their unit cells: (a) hexagonal, (b) honeycomb, and (c) kagome. First order lattice planes are indicated with dashed lines. (a) Six traveling waves perpendicular to the lattice planes are indicated with black arrows. The rotation axis for the dispersion measurement is indicated by the dashed-dotted lines.

hole-to-hole spacing of $a_0 = 535$ nm. The devices are layered as follows: a 20 nm chromium film on top of a 100 nm thick Au layer, which is deposited on a dielectric substrate that comprises of a thin SiN passivation layer, an InP spacer, and 127 nm $\mathrm{In}_x\mathrm{Ga}_{1-x}\mathrm{As}$ (x = 0.536) gain layer on top of an InP substrate. The layer-stack is designed such that it only supports the TM-like SP-mode. Square hole arrays with a similar layer-stack are described in more detail in refs [20, 37, 52].

The SP-dispersion is measured by scanning a fiber-coupled grating-spectrometer through the back-focal-plane of a microscope objective with NA = 0.4. A thin-film polarizer in front of the fiber is used to obtain polarization sensitivity. The fiber is mounted on a motorized x-y stage and is scanned in both the Γ-M and Γ-K direction. The light is collected on the metal-air side of the sample. The SP are excited by spontaneous emission from the optically pumped InGaAs gain layer. The same setup was used in refs [20, 37, 52].

5.3 Theoretical background

This section presents the geometry of the studied lattices and a model to describe their SP-dispersion relations: It covers a traveling wave model, were coupling between these waves results in stop gaps, and it elucidates the connection between symmetry and radiative properties of the coupled modes.

Figure 5.1 shows three different lattices: hexagonal (left), honeycomb (middle) and kagome (right). These lattices share the same C_{6v} symmetry, but have different unit cells and hole densities. The typical hole spacing a_0 is kept constant, while the size a of the unit-cell changes so that the number of holes in the unit-cell increases respectively from 1 to 2 and 3. The hole density changes between the three lattices with a ratio of 1:2/3:3/4.

The dispersion relation is observed via photons that are radiated when the SP scatter on the lattice of holes. Photons emitted at a certain angle (θ_x, θ_y) have an in-

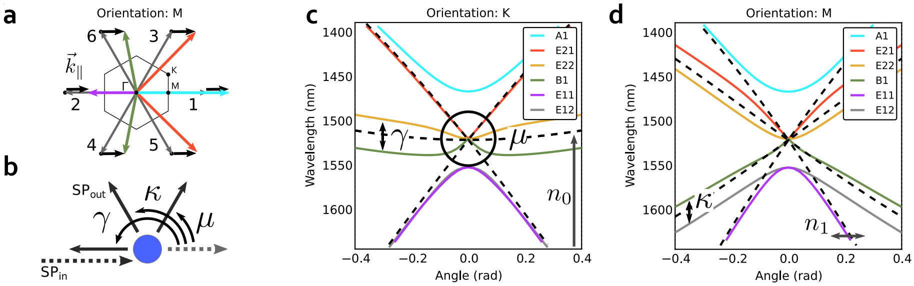

Figure 5.2: Influence of SP-hole amplitude scattering on the SP-dispersion relation. (a) Reciprocal unit cell with the six resonant lattice vectors $\vec{G}_i$ (grey) and $\vec{k}_{sp}$ (colored) for $k_{\parallel}$(black) in the M-direction. (b) The scattering rates in three different directions. (c,d) Theoretical dispersion relation obtained from coupled mode model. The arrows indicate the influence of the scattering rates γ, κ, μ (black arrows) and energy dependent refractive index n_0, n_1 (grey arrows).

plane momentum $\vec{k}_{\parallel} \equiv (k_x, k_y)$, with $k_x = (2\pi/\lambda_0)\sin(\theta_x)$, $k_y = (2\pi/\lambda_0)\sin(\theta_y)$. These photons are associated with SPs with 6 different momenta $\vec{k}_{sp} = \vec{G}_j + \vec{k}_{\parallel}$, where $\vec{G}_j$ are the lattice vectors with length $|\vec{G}_j| = 2\pi/(\sqrt{3}a_0/2)$ belonging to one of the relevant gratings [37]. These lattice vectors are indicated in Fig. 5.2(a). In real space, these are SP waves traveling perpendicular to the lattices planes as indicated in Fig. 5.1(a). The dispersion of these traveling waves is given by $\omega_j = c\,|\vec{k}_{sp}|/n_{sp}$, where n_{sp} is the effective refractive index of the SP-mode.

This uncoupled traveling wave approach already yields the main features of the dispersion relation. The dashed curves in Figs. 5.2(c,d) show the dispersion of uncoupled traveling waves. In the absence of SP-SP scattering, the resonance frequency at the Γ-point is given by $\omega_0 = c\,\left|\vec{G}_j\right|/n_{sp}$. The dashed curves have different slopes around $\theta = 0$. This slope $\frac{1}{\omega}\frac{\mathrm{d}\omega}{\mathrm{d}\theta} \backsimeq \frac{1}{n_{sp,group}}\cos(\phi)$ depends on the group index $n_{sp,group}$ of the SP and the projection between the observed $\vec{k}_{\parallel}$ and $\vec{G}_j$. Figure 5.2(a) depicts $\vec{G}_j$, $\vec{k}_{\parallel}$ and $\vec{k}_{sp}$ for a tilt in the M direction. In the M direction, two traveling waves (k_1 and k_2) are parallel to $\vec{k}_{\parallel}$, which generate two non-degenerate resonances with a steep slope with $\cos(\phi) = \pm 1$. Furthermore, there are two frequency degenerate traveling waves k_3, k_5 with a slope corresponding to $\cos(\phi) = 1/2$ and two traveling waves k_4, k_6 with a slope corresponding to $\cos(\phi) = -1/2$. In total, the six traveling waves thus create four resonances. This is indicated with four dashed lines in Fig. 5.2(d). The dispersion relation in the Γ-K direction as depicted in Fig. 5.2(c) shows three double-degenerate modes as three dashed lines with slopes corresponding to $\cos(\phi) = \pm\sqrt{3}/2$, 0.

In order to describe the SP-dispersion relation more accurately [37, 98], we consider the surface charge $\Psi(\vec{r},t)$, which is proportional to the out of plane $\vec{E}$-field. This surface charge $\rho(\vec{r},t)$ is then decomposed in periodic Bloch waves:

$$\rho(\vec{r},t) = \sum_j \rho_j(t) \exp\left(i\left(\vec{G}_j + \vec{k}_{||}\right)\cdot\vec{r}\right), \tag{5.3.1}$$

where $\rho_j(t)$ is the time dependent amplitude and $\exp\left(i\left(\vec{G}_j + \vec{k}_{||}\right)\cdot\vec{r}\right)$ is the spatial distribution of each plane-wave component. These plane-waves are associated with the lattice vectors $\vec{G}_j$. For the hexagonal lattices, the lowest three resonances at the Γ-point are all six-fold degenerate and a coupled-mode model with six Bloch waves suffices.

Scattering of SP on the holes causes coupling between the traveling waves, which lifts the degeneracy of the modes and creates stop gaps at the Γ-point [48, 99]. This behavior can be described by a coupled mode model for the time evolution of the Bloch waves. A similar model was used previously [37, 52] for plasmonic crystals with a square lattice. Here we extend it to hexagonal lattices. The time evolution of the surface charge can be expressed as $d\psi(t)/dt = -iH\psi(t)$, where $H(k_{||})$ is a 6x6 matrix and $\psi(t)$ a vector with the time dependent parts $\psi_i(t)$. The eigenvalues of this matrix are the resonance frequencies at $k_{||}$. The C_{6v} symmetry of the lattices allows us to describe the coupling with three amplitude scattering rates as depicted in Fig. 5.2(b): We define the 180°-scattering rate γ, the 120°-scattering rate κ, and the 60°-scattering rate μ. Analogous to ref [37], this leads to the following coupling matrix in traveling wave basis:

$$H = \begin{pmatrix} \omega_1 & \gamma & \mu & \kappa & \kappa & \mu \\ \gamma & \omega_2 & \kappa & \mu & \mu & \kappa \\ \mu & \kappa & \omega_3 & \gamma & \mu & \kappa \\ \kappa & \mu & \gamma & \omega_4 & \kappa & \mu \\ \kappa & \mu & \mu & \kappa & \omega_5 & \gamma \\ \mu & \kappa & \kappa & \mu & \gamma & \omega_6 \end{pmatrix} \tag{5.3.2}$$

The diagonal elements are the resonance frequencies $\omega_i = c\,|\vec{G}_i + \vec{k}_{||}|/n_{sp}$ of the uncoupled traveling waves. The off diagonal elements qualify the coupling between these waves: γ for the 180° scattering within the three groups of counterpropagating waves (1,2), (3,4), (5,6), and κ and μ for the 120° and 60° scattering between waves from different groups.

Figures 5.2(c,d) show the influence of the three scattering rates on the dispersion relation. While their influence is mixed near the Γ-point, it is discernible at higher angles. In the Γ-K direction, the effect of the back scattering rate γ is a coupling between the degenerate traveling waves k_5 and k_6, which results in an even and odd combination with a different field distribution and a different frequency. The energy splitting induced by the 120°-scattering rate κ is visible in the Γ-M direction where it couples the degenerate waves k_3 and k_5, and k_4 and k_6. The role of 60°-scattering rate μ is mainly visible at the center of the Brillouin-zone, where all uncoupled waves are degenerate; this rate slightly alters the shape of the dispersion relation at small angles.

The highly symmetric matrix H exhibits the same C_{6v} symmetry as the lattice. We will take full advantage of this symmetry when labeling the modes and describing the number of modes and their radiative nature [34]. The symmetry determines the charge distribution of the modes (irreducible representations of the C_{6v} point group) around the holes at the Γ-point, which resembles either a monopole, dipole, quadrupole, or hexapole depending on the number of local maxima around the hole. These modes are labeled with respectively A_1, E_{1x}, E_{2x}, and B_1, as indicated in Figs. 5.2(c,d). Both the E_{1x} and E_{2x} modes are double degenerate. A graphical representation of these distributions can be found in ref [98].

The radiative character of the modes can be deduced from symmetry arguments. The modes at the Γ-point have different responses on the symmetry operations of C_{6v} which is expressed by their character. These different characters dictate the radiative nature of the different modes at the Γ-point. The symmetry of the mode and the symmetry of free space radiation are either the same or different. Only the dipolar E_{1x} mode is radiative perpendicular to the surface (bright), while the other three modes are non-radiative (dark).

Also the polarization of the radiated light can be deduced from symmetry arguments. For k-vectors between the Γ-point and the M- and K- point (small angles), the symmetry is reduced to C_{1h} and all modes are allowed to radiate. The modes are symmetric or antisymmetric modes under reflection in the emission plane, which is spanned by the emission direction and the surface normal. The symmetric modes couple to radiation with p-polarization (radiated $\vec{E}$ field parallel to the symmetry plane), while antisymmetric modes couple to s-polarized radiation. Compatibility relations link the modes at the Γ-point to these odd and even modes: there are three s- and three p- polarized modes in the Γ-K direction, while there are four s- and two p- polarized modes in the Γ-K direction. This difference is caused by the fact that the B_1 mode has a different character for the mirror operation over the Γ-M or Γ-K-axis.

5.4 Experimental results

Figure 5.3 shows a false color plot of the observed SP-dispersion along the Γ-K and Γ-M directions for three different lattices: hexagonal (left), honeycomb (middle), and kagome (right). The polarization of the radiation is either perpendicular (s-) or parallel (p-) to the plane spanned by $\vec{k}_{\parallel}$ and the surface normal. The polarization is indicated with respectively blue and yellow colors. The dashed lines in Figs. 5.3(a,d) show the theoretical curves from the traveling wave model. The solid lines in Figs. 5.3(a-f) show the theoretical curves from the coupled mode model. These fits yields crucial information on the SP-dynamics (see below). The dispersion shows 6 resonances, following the 6-fold symmetry. At normal incidence only 4 bands remain, of which only the degenerate bands E_{1x} radiate perpendicular

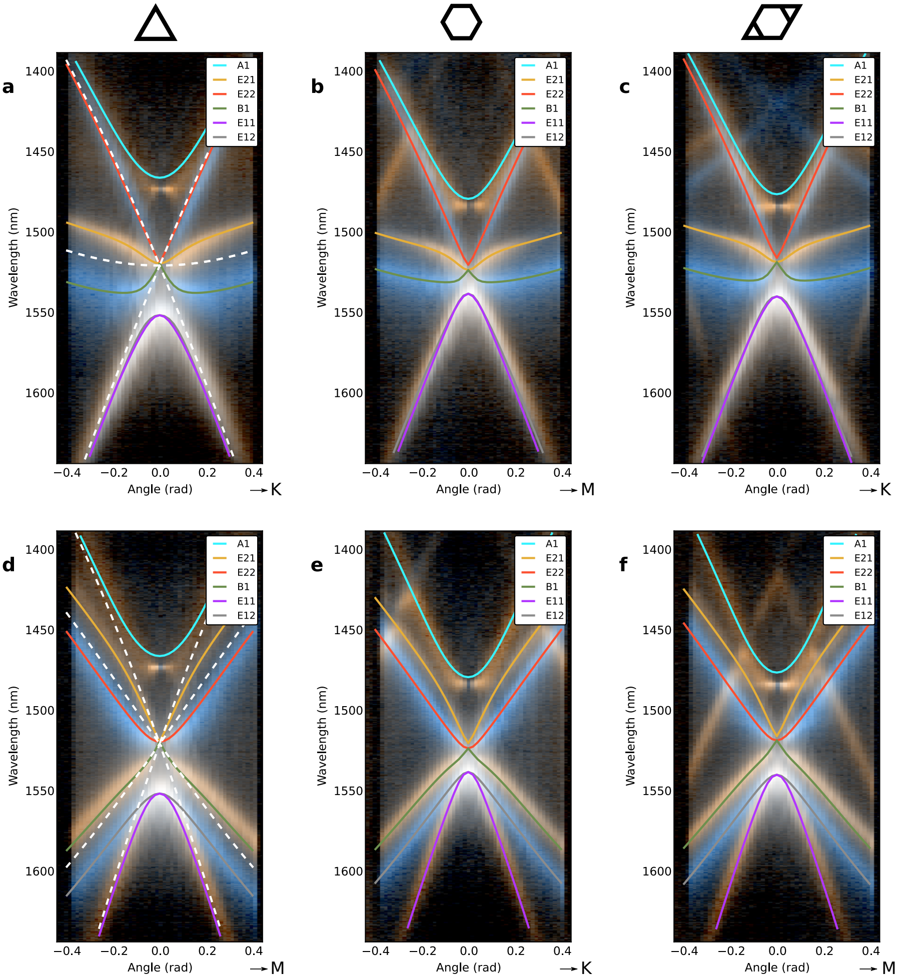

Figure 5.3: Dispersion relations of (a,d) hexagonal, (b,e) honeycomb and (c,f) kagome plasmonic crystals. s- and p- polarized light is indicated with respectively blue and yellow colors. The solid lines indicate theoretical resonance frequencies.

a	γ/ω_0	κ/ω_0	μ/ω_0
	0.015 ± 0.002	0.011 ± 0.002	0.003 ± 0.002
	0.009 ± 0.001	0.008 ± 0.0015	0.0035 ± 0.002
	0.0105 ± 0.001	0.0085 ± 0.0015	0.0025 ± 0.0015

b

$(\gamma/\omega_0)_{scaled}$	$(\kappa/\omega_0)_{scaled}$	$(\mu/\omega_0)_{scaled}$
0.015 ± 0.002	0.011 ± 0.002	0.003 ± 0.002
0.014 ± 0.001	0.012 ± 0.002	0.005 ± 0.002
0.014 ± 0.001	0.011 ± 0.002	0.003 ± 0.002

Table 5.1: (a) Scattering rates for hexagonal, honeycomb and kagome lattices for scattering under 180° (γ), 120° (κ), and 60° (μ). (b) Scattering rates scaled by the relative hole-density.

to the surface ($\theta = 0$), while the other three bands are dark. There are clear frequency splittings between the A_1 and E_{2x}, B_1 and E_{1x} modes at the Γ-point. The B_1 mode almost overlaps with both E_{2x} modes. In the Γ-K direction, there are three modes (B_1, E_{11} and E_{22}) of which the out-coupled light is s-polarized and the other three modes (A_1, E_{12} and E_{21}) are a p-polarization as expected from the symmetry of the lattice. In the Γ-M direction there are two modes (E_{12} and E_{22}) radiating s-polarized light, and 4 modes (A_1, B_1, E_{11} and E_{21}) p-polarized light, as expected from the symmetry.

The honeycomb and kagome lattices exhibit some additional features: extra modes appear at higher and lower frequencies. The honeycomb and kagome lattices have larger unit cells than the hexagonal lattice, while the center of the observed dispersion relations is at the same frequency. Hence, the observed mode-crossings occur at higher order Γ-points. The honeycomb lattice is operating at the 2nd Γ-point and exhibits addition modes that intersect at higher energies, which we associate to the 3rd Γ-point. The kagome lattice is operating at the 3rd Γ-point and has extra modes on both higher and lower energies. The lower energy modes are attributed to the 2nd Γ-point. The higher order mode cannot be attributed to a Γ-point of the kagome lattice. However, inhomogeneity with a period of twice the lattice period will induce the 4th Γ-point at the wavelength of the crossing of the high energy modes. Note that at the 2nd Γ-point, relevant for the honeycomb lattice, the reciprocal space is rotated 30° compared to the 1st and 3th Γ-point and hence the M- and K-direction are interchanged.

The effective amplitudes for surface plasmons scattering on a lattice of air holes are retrieved by comparing the experimental data with our model. As discussed before, different parts of the dispersion relation contain information on different scattering rates. These features are easily identified by eye; the model's resonance wavelengths are overlayed graphically [100] with the measurements and the scattering rates are adjusted by hand. The errors are estimated by adjusting a parameter until the overlap was clearly reduced. Hence the reported errors are interpreted as 2σ deviations. This procedure was performed independently by each of us and the resulting parameters were in accordance with each other within the errors estimated by each researcher. These values are presented in Table 5.1a (discussion follows below).

In order to retrieve a good fit of the modes at high and low energies, the dispersion of the refractive index should be taken into account. The effective refractive index shows dispersion due to the electronic structure of the media. This is included as a perturbation n_1 on the refractive index: $n_{sp}(\lambda) = n_0 + n_1 {}^{\lambda}/_{\lambda_0}$, which mainly influences the shape of the modes at high and low energies. The fitted refractive index n_0 is 3.28 ± 0.005 and n_1 is 0.35 ± 0.15 for all lattices, a straightforward calculation shows that this dispersion n_1 is created by both the gain layer [101] and gold layer.

The fitted scattering rates of the three different lattices parameters are shown in Table 5.1a. The backscatter rate γ is clearly larger than the 120°-scattering rate κ which is again larger than the 60°-scattering rate μ. The main uncertainty in the determination of the 60°-scattering rate μ arises from the dark nature of the A_1, B_1, and E_{2x} modes, limiting the visibility at the location of the dispersion relation that is most sensitive to μ. The scattering rates of the triangular lattice are larger than these of the kagome lattice which are larger than these of the honeycomb lattice. We attribute these differences to changes in the hole density in these three lattices (see below).

5.5 Discussion

All three scattering rates originate from the same physical effect: SP-scattering on subwavelength holes, and hence they are expected to depend on both the hole-density and the scattering cross-section of the holes. Table 5.1b shows the scattering rates scaled to the hole density of the hexagonal lattice, which corresponds to a multiplication by a factor 3/2 for the honeycomb and 4/3 for the kagome lattice. The good overlap between the scaled scattering rates demonstrates the proposed hole-density dependence. Hence, the scattering rates are mainly set by the hole-density, and less by the complexity of the unit-cell.

Figure 5.4 shows the scattering rates dependence on the scattering angle ϕ. The angle dependence of the scattering rates can be described by the equation $a - b\cos(\phi)$, indicated in Fig. 5.4 with the dashed line as guide to the eye. This line predicts that the forward scattering is zero. A physical interpretation follows below.

We first compare our results with earlier work on SP scattering in square [37] and hexagonal lattices [98, 102]. The reported scattering rates for square lattices [37] with a similar layer stack and hole size are $\gamma/\omega_0 = 0.016 \pm 0.02$ for 180°-scattering and 0.008 ± 0.003 for 90°-scattering. After scaling these results with the relative hole density ($\rho/\rho_0 = 1.03$), they are added to Fig. 5.4; the 180°-scattering overlaps very well with our results for hexagonal-based lattices, and also the extra

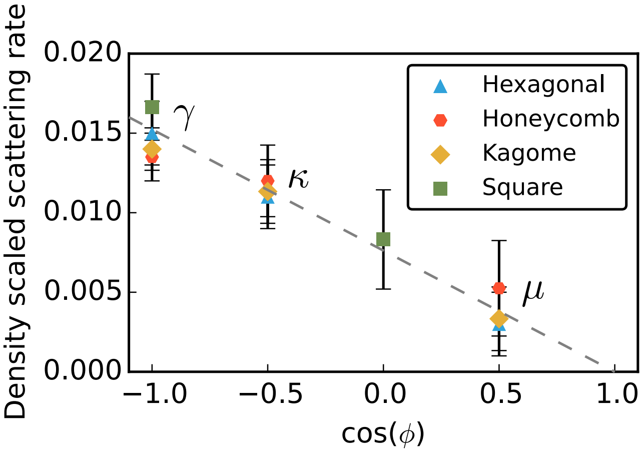

Figure 5.4: Scattering rates scaled to the hole-density of the hexagonal lattice as function of scattering angle ϕ for scattering under 180° (γ), 120° (κ), and 60° (μ). The scattering rates for 180° and 90° are taken from ref [52]. The dashed line indicates $a - b\cos(\phi)$ for $a/b = 1$.

datapoint at 90°-scattering neatly follows the $\cos(\phi)$-relation.

For completeness, we will also compare our results with the scarce previous efforts[98, 102]. Scattering rates of hexagonal plasmonic crystals were not reported yet, but these can be extracted from the dispersion relations in refs. [98, 102] using the procedure explained above. We take the results for hole sizes ($d/a = 0.34$) that are comparable to our sample. From the simulations in ref [102], we extract scattering rates $\gamma/\omega_0 = 0.0040 \pm 0.0010$, $\kappa/\omega_0 = 0.0028 \pm 0.0003$ and $\mu/\omega_0 = 0.0004 \pm 0.0003$. In the measurements of ref [98] the A-band of sample with the relevant hole sizes is outside the observed wavelength range. Instead, we extrapolate this band with a spline and extract scattering rates $\gamma/\omega_0 = 0.050 \pm 0.010$, $\kappa/\omega_0 = 0.010 \pm 0.010$, and $\mu/\omega_0 = 0.002 \pm 0.010$. Even though these scattering rates were observed at shorter wavelengths in the visible ($\lambda \sim 600$ nm), they are comparable in magnitude to our results. Furthermore, also the sequence of the scattering rates is the same: backscatter rate γ is larger than the 120°-scattering rate κ, which in turn is larger than the 60°-scattering rate μ.

The proposed $a - b\cos(\phi)$ dependence of the scattering rate is based on the SP-scattering of a single small cylindrical hole. This scattering process can be described by an effective electric $\vec{p}$ and magnetic $\vec{m}$ dipole [50]. In this model the incident SP-wave excites with these dipoles, which then radiate partially to SP-waves again. SP-waves are mainly TM polarized, and hence the out-of-plane component p_z of the electric dipole and the in-plane component m_y of the magnetic dipole dominate the scattering process. Both dipoles have a distinct in-plane scattering profile;

the electric dipole p_z radiates isotropically, while the magnetic dipole m_y radiates dominantly in the forward and backwards directions. The scattered field consists of a combination of these dipole responses, and yield a combined scattering amplitude $a - b\cos(\phi)$ with

$$\frac{b}{a} = \sqrt{\frac{\epsilon+1}{\epsilon}}\frac{m_y}{p_z} = \left(\frac{\epsilon+1}{\epsilon}\right)\frac{-\alpha_m}{\alpha_p}, \tag{5.5.1}$$

where α is the polarizability of a single hole. The factor $\sqrt{\frac{\epsilon+1}{\epsilon}}$ accounts for the small difference in the ratio H/E for confined SPs compared to free space electro-magnetic waves [50]. The ratio between the permitivities $\epsilon = \epsilon_{metal}/\epsilon_{dielectric} = -10$ for our system, and hence this factor is close to 1. Figure 5.1b shows the scattering rates as function of $\cos(\phi)$. The scattering rates overlap with a line that crosses the $\cos(\phi)$-axis at $\cos(\phi) = 1$, which indicates that the forward scattering is zero, suggesting that $|\vec{p}| \simeq |\vec{m}|$. This corresponds to the second Kerker condition [103], in which a hole acts as a Huygens-reflector. The supplemental information of ref. [50] calculates the polarizabilites α_m and α_p for holes in perfectly conducting metal film on a glass substrate, where a surface plasmons are traveling on the metal-air interface. For our relative hole radius $d/\lambda = 0.18$ this theory predicts that the polarizabilities have an opposite sign and a ratio $-\alpha_m/\alpha_p \approx 3.5$. For a smaller hole radius this ratio increases to 1.7 for zero radius. However, our experimental data indicate that the ratio is $\simeq 1$ for our geometry. This quantitative discrepancy might result from the following: Our SP scattering process is more complicated than captured in the calculations of the dipole model, because our SPs are scattering on holes filled with air, while they are traveling on the metal-semiconductor interface and the metal-air interface contains a chromium layer to damp the SP. The current calculations on the dipole model, assume the same index for both medium and hole as well as a perfectly conducting metal, where no field penetrates in. For a realistic gold film the optical penetration-depth at telecom-frequencies is typically ≈ 20 nm, resulting in a slightly higher effective hole diameter.

We find a qualitative agreement between the dipole model and our measurements. This is surprising, because there are two reasons why a description based on single-hole SP-scattering might be too simple. First of all, this dipole model does not take quasi cylindrical (or creeping) waves into account, while they carry more than 40% of the field at short (< 2.5 μm) distances [50] and they are typically responsible for half of the extra-ordinary transmission through metal hole arrays [44, 104]. However, there is no influence of quasi-cylindrical waves visible in our measurements, because the dispersion relation is formed by interference between scattered waves from many holes. The propagation distance of SP is much larger than for quasi-cylindrical waves and hence SPs dominate the dispersion [105, 106]. Finally, the dipole model describes the response of a single hole, while we observe the response of a lattice of holes. Hence, one might expect that lattice effects and multi-hole phenomena, such as coherent addition of the scattering of all holes and hole-hole (dipole-dipole) interaction, will become important. The current experiments do not yet have sufficient control to distinguish these effects, and detailed theory is absent: even for a lattice of only electric dipoles this is already a non-trivial exercise [107], where the magnetic dipoles are ignored due to their complexity. Hence, this remains a future challenge.

5.6 Conclusions

We experimentally studied the scattering properties of three different metal-hole-array plasmonic crystals with hexagonal lattices, but different unit-cells. The unit cells have the same symmetry, but an increasing number of holes and complexity. We compare the observed dispersion relations with a coupled mode model, which yields the amplitude scattering rate of surface plasmons on a lattice of metal holes under three different angles: 60°, 120°, and 180°. We find that the influence of the three different lattices on the scattering rates is dominated by the hole-density. The symmetry of the lattice only selects the allowed scattering angles by constructive interference, but does not influence the individual scattering rates. Furthermore, we find that the angle dependence of the scattering rates shows a qualitative, but no quantitative, agreement with a single-hole dipole approximation that takes only the SP-mode into account. Hence, we conclude that lattice effects and hole-hole (dipole-dipole) interaction are less important than the single hole response.

Acknowledgments

The authors thank Philippe Lalanne and Haitio Liu for the discussions about quasi-cylindrical waves, and Peter J van Veldhoven and Erik Jan Geluk for their help in fabricating the samples at the COBRA Research Institute of the Technische Universiteit Eindhoven, The Netherlands. This work is part of the research program of the Foundation for Fundamental Research on Matter (FOM), which is part of the Netherlands Organization for Scientific Research (NWO).

Chapter 6

Two-mode surface plasmon lasing in hexagonal arrays

We demonstrate surface-plasmon lasing in hexagonal metal hole arrays with a semiconductor gain medium. The device can be tuned between two laser modes, with distinct wavelengths, spatial distributions and polarization patterns by changing the size of the optically pumped area. One of the modes exhibits a six-fold polarization pattern, while the mode observed for larger pump spots has a rotationally symmetric polarization pattern. We explain the mode tuning by the differences of in-plane and radiative out-of-plane losses of the modes. The spatial and polarization properties of the modes are conveniently described by a sum of vectorial OAM beams with orbital, spin and total angular momentum $j = \ell + s$.

6.1 Introduction

Periodic structures and crystals scatter waves and create standing waves that can completely stop the wave propagation in specific crystal directions. The absence of propagating modes has important consequences. Atoms arranged in a crystalline structure give rise to electronic bandgaps and have opened the wide field of electronics. Analogously, periodic dielectric structures [78] have stimulated developments in photonics and have enabled, among others, planar photonic crystal reflectors [108–110], compact etalon filters [111, 112], and high-performance photonic crystal lasers emitting at wavelengths ranging from the visible regime [36, 113, 114] to the THz regime [31, 32]. The revival of the field of surface plasmons (SPs) was triggered by the observation of extraordinary transmission in crystals in the form of metal hole arrays. We combine similar plasmonic crystals with gain, to compensate the intrinsic SP losses and create a SP laser.

Plasmonic crystals have different optical properties compared to photonic crystals at visible and telecom wavelengths. In plasmonic crystals, the avoided crossings in the band structure are small, often hardly resolvable and no complete band gaps are possible. This implies that the feedback needed for laser operation is low, while the losses of surface plasmons are high due to electron scattering (Ohmic loss) and hence high gain is needed in order to reach the laser threshold. The mode volume of SP lasers can be much smaller than their photonic counterpart [22] and thus the power needed to reach threshold may be lower nevertheless. We address the question to what extent the theory for photonics systems can be applied to plasmonic.

In this chapter, we demonstrate SP lasing in hexagonal plasmonic crystals. To our surprise, we find lasing in two modes with different polarization profiles. Tuning between these modes is achieved by changing the size of the pump spot. We link this observation to previous experimental and theoretical work on photonic crystals. Furthermore, we explain the mode and polarization profiles from symmetry arguments and show that a compact description of the mode profiles can be given in terms of a sum of orbital angular momentum (OAM) beams.

6.2 Setup and Methods

Our devices consist of a hole array in a 100 nm thick gold film on an InP semiconductor substrate containing a 127 nm thick $\mathrm{In}_x\mathrm{Ga}_{1-x}\mathrm{As}$ ($x = 0.536$) gain layer. Holes with a diameter of 160 nm are placed in a hexagonal lattice with hole spacing $a = 525$ nm. This sample is manufactured using the same procedure on the same wafer as the samples in ref. [95].

Our experimental geometry is as follows: the sample is optically pumped at normal incidence on the semiconductor side with a Gaussian beam from a continuous-wave laser with a wavelength of 1064 nm. Light is collected on the other side of the sample and analyzed with a CCD camera. The SP-laser light is selected with a 12 nm wide band-pass filter centered around the wavelength of the lasing SP-mode. Polarization-resolved (stokes parameters) and phase-resolved measurements of the optical field are performed in the far- and near- field of the laser beam. The dispersion of the SP modes on the hole array are measured by recording the emission spectrum $I(\omega, \boldsymbol{\theta})$ as function of angle $\boldsymbol{\theta} = (\theta_x, \theta_y)$ to find the relation $\omega(\boldsymbol{k}_{\text{sp}})$, where $\boldsymbol{k}_{\text{sp}} = \boldsymbol{k}_{\|,\text{photon}}$ (modulo the lattice vectors) and $\left|\boldsymbol{k}_{\|,\text{photon}}\right| = (\omega/c)\sin|\boldsymbol{\theta}|$ [37, 95]. This experimental geometry is described in more detail in ref. [37, 65].

6.3 Results

We observe SP lasing in two distinct modes, which emit at wavelengths $\lambda \approx 1470$ nm and $\lambda \approx 1500$ nm. We attribute the high-energy mode to the A-band of the dispersion relation [95] and the low-energy mode to the B-mode. The A-band is known to have a monopole-like charge distribution [98, 115] and is expected to radiate radially polarized light [115]. The B-mode has a hexapole-like charge distribution and therefore is expected to have a more complex polarization pattern.

Figures 6.1(a) and (b) show images of the sample plane, i.e. they show the radiative part of the near-field of the SP-laser mode. The A-mode is donut shaped; it has a dark center with a bright ring around it. The B-mode has a different profile; it has six bright lobes placed in a hexagonal shape. Another striking difference is the size of the modes. The A-beam shown in Fig. 6.1 has a max-max diameter of 22.4(5) μm and the B-mode has a diameter of 10.2(4) μm. The images in Fig. 6.1 are obtained with a slightly elliptical Gaussian pump spot with an average full-width-half-max (FWHM) diameter of 15.9 ± 0.7 μm and 7.2 ± 0.7 μm for respectively the A- and B-mode. The ±0.7 μm indicates the difference between the long (short) axis and the average diameter. The diameter of the laser area changes when we change the size of the pump spot. The A-mode is always larger than the B-mode in our device.

Figure 6.1 also shows the polarization state of the light. The measured Stokes parameters are visualized as white ellipses. The A-mode is mainly radially polarized; only the areas with high intensity show some elliptically polarized light (Stokes parameter $s_3 < 0.7$). The polarization of the monopole A-mode resembles the sum of two orbital-angular-momentum (OAM) beams with total angular momentum $j = \ell + s = 0$ ($\ell = \mp 1, s = \pm 1$) [116–120], as illustrated in the inset of Fig. 6.1(a) and discussed below. The polarization of the hexapole B-mode has a mixed radial and azimuthal character. The polarization changes six times from radial to azimuthal over the full 2π angular range, i.e. it resembles a $j = \pm 3$ ($\ell = \pm 2, s = \pm 1$) beam. The OAM description also includes the relative phase of different parts of the beam, which is indicated by the direction of the arrows in the insets of Fig. 6.1. This information cannot be derived from the Stokes parameters. It was obtained in a phase-resolving experiment with the technique described in ref. [65], which yields the local field polarization and phase as shown in Appendix 6.A. We thus confirmed that the polarization-arrows are in the directions indicated in the insets

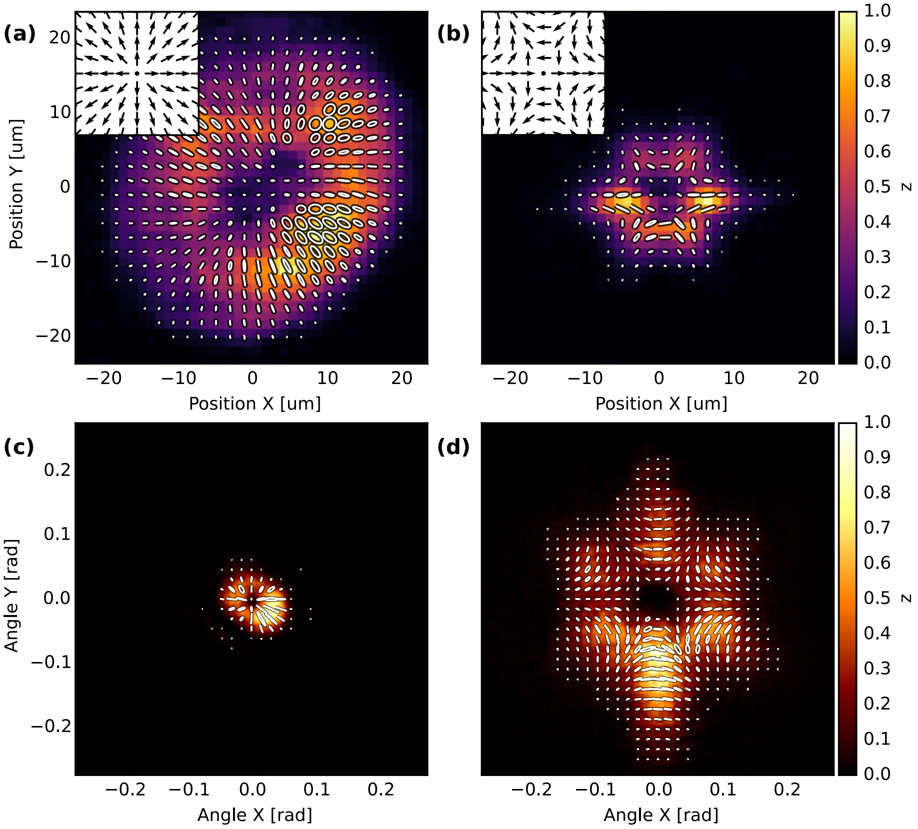

Figure 6.1: Intensity and polarization profiles of a surface plasmon laser in a hexagonal lattice under excitation with a pump spot of (a, c) ∼16 μm diameter or (b, d) ∼7 μm diameter. The monopole A-mode has (a) a large lasing area, and (c) a compact far-field. The hexapole B-mode has (b) a small lasing area, and (d) a wide far-field. The white ellipses indicate the local polarization direction and state of the light. Insets: Polarization pattern of a sum of OAM modes with (a) $j = 0$ for the A-mode, and (b) $j = \pm 3$ for the B-mode.

of Fig. 6.1(a,c).

The measured local phase of the beams also contains additional information: it shows that the A-mode has a positive radial phase-gradient. A similar gradient is observed for the A-mode in square-lattices [65]. The B-mode has a negative radial phase-gradient. These signs are as expected: the sign of the phase gradient depends on the operation wavelength compared to the lattice spacing, and a wavelength $\lambda > \sqrt{3}n_{eff}a/2$ will induce a negative phase-gradient, as is the case for the low-energy B-mode

Figures 6.1(c, d) show the far-field beam profiles. They are comparable to the near-field beam profiles described above: the A-mode is again donut-shaped, while the B-mode is hexagonal shaped. The difference is the opening angle; the large area of the A-mode generates a compact far-field with a max-max openings angle $2\Delta\theta = 56(4)$ mrad, while the small area of the B-mode generates a wide far-field with opening angle $2\Delta\theta = 162(10)$ mrad. The etendue $G = (\pi\Delta r\Delta\theta)^2$ is 1.0 μm^2 for the A-mode and 1.7 μm^2 for the B-mode. Furthermore, the six-lobed far-field intensity distribution of the B-mode is rotated by 90° compared to its near-field, while the polarization profile is not rotated.

The laser threshold and input-output characteristics of both modes are different. The A-mode has a threshold of 150(10) mW and an input-output slope $dP_{\text{out}}/dP_{\text{in}} = 5.2(5)$ μW/mW, while the B mode has a higher threshold of 200(3) mW and a steeper slope of 15(1) μW/mW for the pump sizes mentioned above. The larger slope indicates that the B-mode radiates more efficiently. The threshold and slope depend on the location on the sample and on the pump spot size. The observed thresholds are typically within 50 mW of the thresholds mentioned above. The laser threshold of the A-mode is typically higher than that of the B-mode. More details are shown in Appendix 6.B.

The A- and B-mode lase under distinct conditions. The A-mode lases when a large area is pumped, while the B-mode lases when a smaller area is pumped. The pump spot diameter at which the laser switches is typically 15 ± 1 μm for a pump power of 250 mW. Hence we can select a laser mode by tuning the size of the pumped area.

We studied the existence of the A- and B- laser mode in samples similar to the one described above and observed laser action in monopole and hexapole modes in samples with minimum hole spacing of $a = 515$, 525, and 535 nm. Besides samples with a hexagonal lattice, we also studied metal hole array lasers with honeycomb and kagome lattices. All observed laser beams are similar to the results reported here. Also in these lattices the desired laser mode can be selected by tuning the size of the pumped area. From this we conclude that lasing in two modes is a universal property of hexagonal-based (C_{6v} point group) lattices.

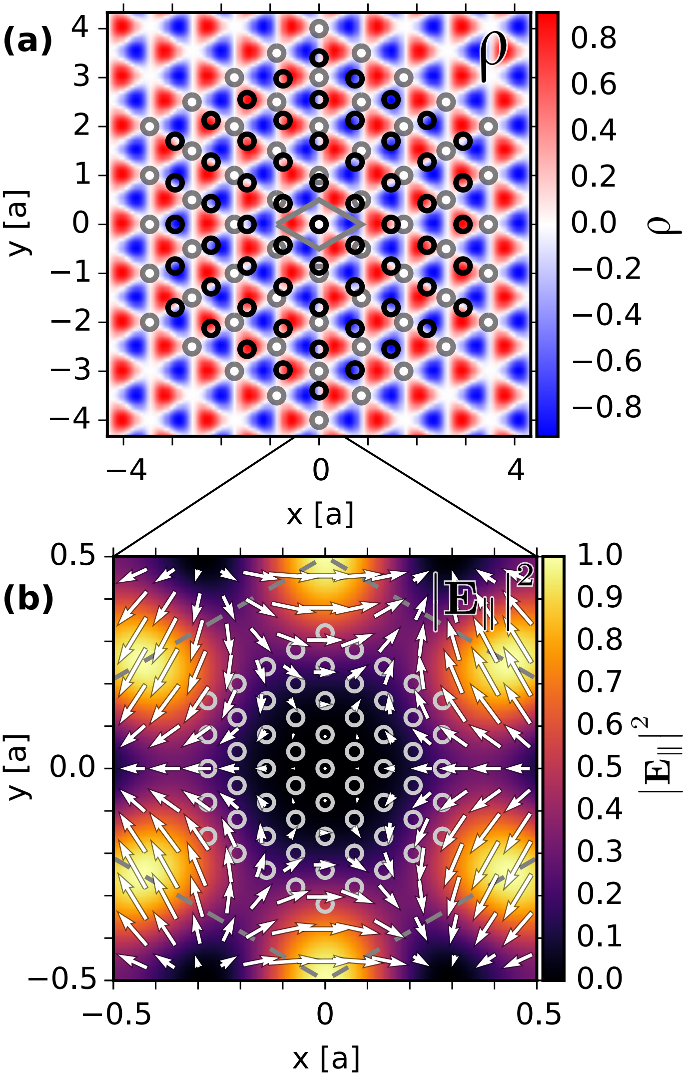

Figure 6.2: Model to understand radiation and polarization of a mode near the Γ-point, applied to the B-mode. (a) The charge distribution ρ of 9×9 unit cells. The grey rhombus indicates a single unit cell. The grey circles indicate the position of the holes when the lattice- and wave-vector are identical. The black circles indicate the (exaggerated) position of the holes for a wave-vector that is slightly shorter than the lattice-vector. (b) The black holes have been folded back on the unit cell. The polarization and intensity of the in-plane field $\mathbf{E}_{\parallel}$ is indicated with respectively white arrows and the colored background.

6.4 Discussion

The distinct profiles and polarizations of the A- and B-mode follow from symmetry by a two-step argument. First, the symmetry of the unit cell and lattice together dictate the charge distribution ρ [34, 98], and thereby the out-of-plane field $E_\perp \sim \rho$ [98] and the in-plane field $\mathbf{E}_{||} \sim \nabla \mathrm{E}_\perp$. For modes at the Γ-point ($k = 0$), the charge distribution can be described by an irreducible representation of the C_{6v} point group. Radiation to free space is governed by the in-plane H-field $\mathbf{H}_{||}$ [37, 115], associated with the in-plane E-field $\mathbf{E}_{||}$. Second, the radiation profile of the full device resembles the field distribution inside a single unit cell. This argument applies because the laser operates close to the Γ-point ($k \neq 0$) and is based on translation symmetry (Bloch theorem) and "spatial sampling" as explained below.

To elucidate the second step, we focus on the hexapole B-mode. Figure 6.2(a) shows the charge distribution of the hexapole B-mode [98]. The grey circles indicate the position of the holes when the lattice and wave vector are identical ($k = 0$), i.e. the lattice spacing is $a = 2\lambda_{sp}/\sqrt{3}$. Because SP lasers do not operate exactly at the Γ-point, but close to it [35, 65], the wave vectors are slightly longer or shorter than the lattice vector ($k \neq 0$). In our perturbative approach we neglect the influence of the holes on the fields. In this approach the mismatch $k \neq 0$ merely results in an elongation or contraction of the full field pattern relative to the lattice and therefore the nodes of the fields do not align with the position of the holes. This is illustrated in Fig 6.2(a), where the black circles indicate the (exaggerated) position of the holes for a wave vector that is slightly shorter than the lattice vector. Translation symmetry of the field pattern and the lattice now allows one to fold back the position of the (shifted) holes on the unit-cell [121, 122]. Every hole thereby samples the field at a different location in the unit cell as is indicated in Fig. 6.2(b). Hence, with this second, "spatial sampling", step we have mapped the radiated near-field of the whole lattice to the field inside a single unit cell. Figure 6.2(b) shows the predicted intensity and polarization of the radiating field for the B-mode; these patterns indeed resemble the experimentally observed polarization.

More quantitative results can be derived by Taylor-expanding the radiating field around the central hole in the unit cell. We performed this Taylor expansion for the radiating field derived from the charge distribution presented in ref. [98]. The resulting expression can be written as the sum of two $\pm j$-OAM beams; for the A-mode $j = 0$ ($\ell = \mp 1$, $s = \pm 1$) and for the B-mode $j = \pm 3$ ($\ell = \pm 2$, $s = \pm 1$). This is consistent with the observed polarization patterns in Fig. 6.1.

The experimentally observed polarization patterns can be described by the sum of two orbital angular momentum (OAM) beams with opposite circular polarization [116–120]:

$$\mathbf{E}^{\ell}(r, \phi) = u(r)\left[\exp\left[-i\left(\ell\phi + \varphi\right)\right]\mathbf{e}_{+} + \exp\left[i\left(\ell\phi - \varphi\right)\right]\mathbf{e}_{-}\right] \tag{6.4.1}$$

where (r, ϕ) are the radial and azimuthal coordinate of the beam. This function is the superposition of two components with helicity $s = \pm 1$ and orbital angular momentum $\mp \ell$. Equation (6.4.1) describes a field that has uniform intensity around the ring (azimuthal direction) and has a linear polarization everywhere. The phase difference 2φ between both polarizations determines the local orientation of the polarization. For example, $\ell = \mp 1$ describes a radial polarization when $\varphi = 0$, while it describes an azimuthal polarization when $\varphi = \pi/2$.

The radial part of the beams can be described with a $p = 0$ Laguerre-Gauss amplitude function $u(r) \propto r^{|\ell|} \exp\left(-r^2/r_0^2\right)$. The etendue of such Laguerre-Gauss OAM modes scales as $G \propto (2p+|\ell|+1)^2$ [120, 123], making $G_A/G_B = \left(\frac{|\ell=\mp 1|+1}{|\ell=\pm 2|+1}\right)^2 = 0.44$. This is in reasonable agreement with the experimental observed etendue $G_A/G_B = 0.56$. OAM beams are an effective description of the observed modes. They describe both the polarization pattern and the etendue.

There are two experimental observations that require us to go beyond the description presented in Eq. (6.4.1) and consider more than two OAM beams. First, the six bright lobes in the intensity profile of the B-mode indicate that this is not a pure $\pm j$ mode; these lobes can be explained by a mixture of 90% $j = \pm 3$ ($\ell = \pm 2$, $s = \pm 1$) and 10% of a $j = \mp 3$ ($\ell = \mp 4$, $s = \pm 1$) mode. Second, the A- and B-mode have distinct azimuthal profiles, while their radial profiles have approximately the same shape $u(r) \sim r^{\beta} \exp\left(-r^2/r_0^2\right)$ with $\beta \simeq 1$ (see Appendix 6.A). This profile is expected for the A-mode ($|\ell| = 1$), but strange for the B-mode ($|\ell| = 2$). Phenomenologically, we can explain the strange radial profile by admixing modes with a $p \neq 0$ component. However, the underlying physics is not yet understood. It might be related to the unbalance between the traveling waves that builds up outside the center of the device by the combined action of gain and feedback [35]. This unbalance removes the field nodes, enables radiation [87], and modifies the emitted intensity profile [72].

We can tune which mode lases by changing the pump spot size. To explain this behavior, we will discuss the total loss of both modes, and distinguish between in out-of-plane and in-plane loss.

The out-of-plane loss is radiative loss; it depends on the laser area, the spatial distribution of the modes, the scattering properties of the holes [52], the wave vector detuning [87], and the refractive index profile [65]. The radiative loss of the hexapole B-mode is higher than the monopole A-mode, as indicated by the higher slope of the threshold measurements. This is consistent with the field distribution picture presented above: the hexapole has more structure and its field increases more rapidly around the central hole in the unit cell than the monopole field. Hence the hexapole mode will radiate more efficiently at holes outside the center of the device.

The in-plane loss results from SPs that leave the pumped area due to insufficient feedback. The magnitude of the total in-plane loss depends on the length of the boundary of the pumped area. The feedback depends on the product of the effective in-plane coupling κ and the device length L [35]. The effective in-plane coupling coefficient κ contains contributions from scattering of all traveling waves and can thus be different for both modes [124]. We speculate that the effective in-plane coupling constant κ_A of the A-mode is smaller than κ_B of the B-mode, such that the A-mode requires a larger pump spot to obtain the same κL product.

We can tune the ratio between in-plane (circumference) and out-of-plane (surface) loss by changing the size of the pumped area; when the pumped area is small the ratio between circumference and surface is large. Hence lasing is favored in the B-mode with a low in-plane loss (high feedback), while a higher surface loss can be tolerated. When the pumped area is large, the device prefers to operate in a mode with less surface loss, while a high in-plane loss (limited feedback) can be tolerated and hence the device lasers in the A-mode.

Finally, we compare our observation of monopole and hexapole laser modes to previous results on photonic crystals. Imada *et al.* [72] reported on the hexapole mode in photonic crystals, for modes with a transverse electric (TE) polarization. In those electrically pumped experiments, an electrode was obscuring the view on the radiated light. The observed polarization is rotated 90° compared to our TM-modes. Liang *et al.* [124] demonstrated tuning between the monopole and hexapole mode by changing the size of the holes in a dielectric slab and hence changing the in-plane losses. The monopole and hexapole modes are also observed in the THz regime for modes with TM-polarization [115]; the polarization of the far field is observed, and selection between the modes is obtained by tuning a narrow-band gain spectrum to the resonance frequencies of the modes. From this we conclude that lasing in two modes is a universal property of hexagonal-based (C_{6v} point group) lattices.

6.5 Conclusion

In conclusion, we have observed SP-lasing in hexagonal metal hole arrays, both in a monopole and in a hexapole mode. The modes have different spatial and angular profiles which all resemble a superposition of circularly polarized OAM beams: a monopole mode with total angular momentum $j = 0$ ($\ell = \mp 1$, $s = \pm 1$), and a hexapole mode with $j = \pm 3$ ($\ell = \pm 2$, $s = \pm 1$). The observed intensity and polarization profile can be explained by symmetry arguments. Mode selection can be achieved by tuning the size of the pump spot, which affects the ratio between in-plane and out-of plane loss. These observations in TM-polarized plasmonic lasers are consistent with previous work on TE-polarized photonic crystals.

Acknowledgment. The authors thank Eric R. Eliel for useful discussions and feedback, and Peter J. van Veldhoven and Erik Jan Geluk for their help in fabricating the samples at the COBRA Research Institute of the Technische Universiteit Eindhoven, The Netherlands.

Appendices

In these appendices, we present the vectorial E-field of SP lasers in hexagonal arrays. The polarization of the field is explicitly presented as Stokes parameters, while it is implicit in the combined intensity and phase plots. Furthermore, we show the peculiar behavior of the SP lasers around laser threshold.

6.A Polarization, intensity and phase

We first give a Stokes representation of the polarization state of the emitted laser light. The s_0 parameter indicates the intensity of the light, the s_1 and s_2 parameters indicate the linear polarized state of light in two different polarization bases, and the s_3 parameter indicates the circular polarization state. The Stokes parametes s_1 and s_2 are measured by projecting the laser on a linear polarizer at four different orientations $(-45°, 0°, 45°, 90°)$ and the circular Stokes parameter s_3 is measured with an additional quarter-wave plate.

Figure 6.3 shows the measured Stokes parameters of the far-field beam profiles of the A- and B- mode. Measurements of s_1 and s_2 on the A-mode yield two-fold symmetric patterns as expected for a $\ell = \mp 1$ beam. The A-mode is predominantly radially polarized. The light is in a linearly polarized state along the $\theta_x = 0$ and $\theta_y = 0$ axis, while it is slightly elliptically polarized, with circular Stokes parameter $|s_3| < 0.7$, in the 45° direction. While symmetry prohibits emission of elliptically polarized light along mirror planes of the lattice, it does not prohibit emission of elliptically polarized light in other directions. The s_1 and s_2 parameters of the B-mode show a four-fold symmetric pattern, as expected for a $\ell = \pm 2$ beam. The B-mode polarization is six-fold azimuthally and radially polarized; it is azimuthally polarized in the Γ-K directions of the lattice and radially polarized in the Γ-M directions.

We have measured intensity and retrieved phase with a technique described in chapter 4. Figure 6.4 shows the measured intensity and retrieved phase of the A- and B-mode measured behind a horizontal (top row) or vertical (bottom row) polarizer. The polarization-resolved intensity measurements in Figs. 6.4(a, b) and Figs. 6.4(e, f) contain equivalent information as the Stokes s_1 parameter, which is already discussed above. Now we will discuss the phase profiles of the beams, which contain additional information. Figures 6.4(c, d) show the retrieved phase profile of the A-mode. The sharp transition in the dark center indicates a π-phase jump. This show that the electric fields on opposite sides of the beam are pointing in opposite directions, as expected for radially polarized light. Furthermore, the phase has a positive radial gradient; the phase increases by 0.5(2) rad from the center to the edge of the laser area. Figures 6.4(g, h) shows that the phase of the B-mode has a more complex profile; in both polarizations it is four-lobed. The phase of neighboring lobes is shifted by π-phase jump. The phase gradient of this mode is negative; the phase decreases by 0.7(3) rad from the center to the edge of the laser area.

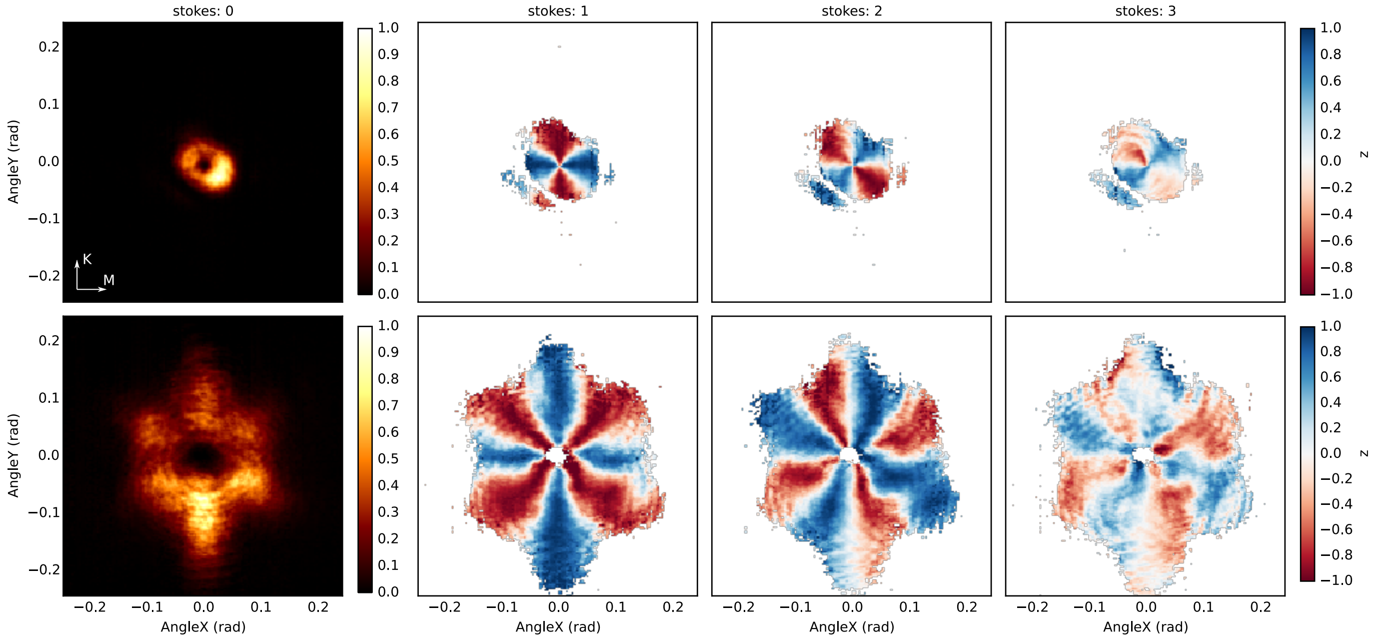

Figure 6.3: Stokes parameter representation of the far-field of the (top row) A- and (bottom row) B-mode.

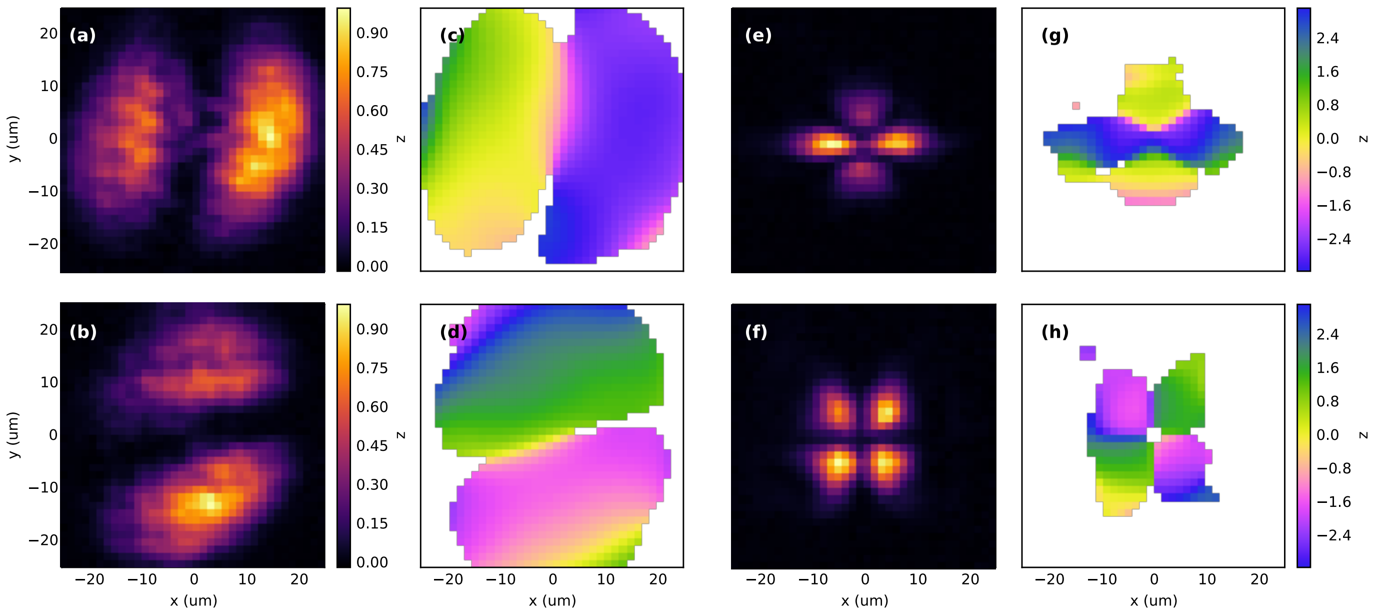

Figure 6.4: Polarization resolved intensity and phase of the (a-d) A- and (e-h) B-mode. (a, b, e, f) Near field intensity and (c, d, g, h) phase distribution, measured behind a horizontal (top row) or vertical (bottom row) polarizer. Note that the phase is only shown from areas with sufficient intensity, i.e. more than 3% of the maximum intensity.

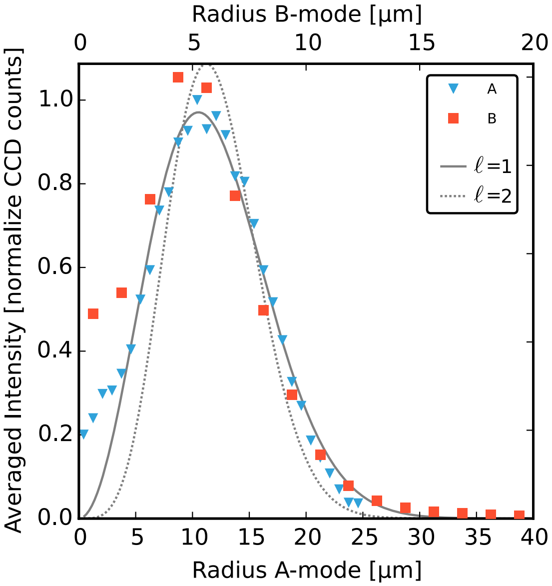

Figure 6.5: Radial intensity profile of the A- and B-modes. The curves indicate fits with Laguerre-Gauss modes with different ℓ.

The reported phase gradients originates from the mismatch between the wave-vector and the lattice-vector: a negative phase gradient is obtained when the SP wave-vector is shorter than the lattice-vector, such that the field at holes more outwards from the center lags behind the field at the center (see Fig. 6.2 for an illustration), and vice versa. The magnitude of the phase gradient can be modified by a non-uniform refractive index profile [65].

Figure 6.5 shows the measured radial intensity-profile of the A- and B-mode. The rotationally-averaged intensity is normalized by its maximum value. The radial intensity profiles of both modes are surprisingly similar. These profiles are fitted with $I(r) = |u(r)|^2$ where $u(r) \sim r^\beta \exp\left(-r^2/r_0^2\right)$; the resulting curves for $\beta = 1$ and $\beta = 2$ are displayed in Fig. 6.5 with respectively a solid and a dashed curve. The best overlap is found for $\beta = 1$ and the obtained beam widths are reported in section 6.3. An analysis of the beam profiles in the far-field shows that the radial profiles of the beams have the same shape and can also be best described by $\beta = 1$ (data not shown).

6.B Laser threshold

Figure 6.6 shows the power of the SP laser as a function of the pump power for lasing in the A- and B-mode. The output of the B-mode exhibits a clear threshold around 200 mW and increases linearly above threshold with slope

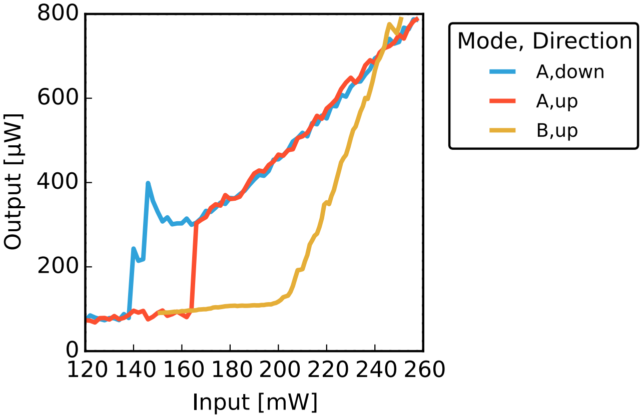

Figure 6.6: The output power of the SP lasers as a function of the pump power for lasing in the A- and B-mode.

$dP_{\text{out}}/dP_{\text{in}} = 15(1)\,\mu\text{W/mW}$ and does not show hysteresis. The A-mode has a more complicated input-output behavior. When scanning the input power from 100 mW up to 260 mW, the mode suddenly starts to laser in a step-wise fashion at threshold power $P_{\text{up}} = 160(2)\,\text{mW}$ and increases in power with a smaller slope $dP_{\text{out}}/dP_{\text{in}} = 5.2(2)\,\mu\text{W/mW}$. The A-mode shows hysteresis: when decreasing the power below P_{up}, the laser stays active till the threshold $P_{\text{down}} = 140(2)\,\text{mW}$. Even more surprising is that the output power increases just above the threshold P_{down} upon reduction of the pump power. We attribute this hysteresis to heating of the sample.

Bibliography

[1] G. G. Stokes, in *Rep. 16th Meet. Brit. Assoc. Adv. Sci.* (Murray, London, Southampton, 1846), pp. 1–20.

[2] Walter Munk, Frank Snodgrass, and George Carrier, *Edge Waves on the Continental Shelf*, Science **123**, 127 (1956).

[3] M. Fleischmann, P. J. Hendra, and A. J. McQuillan, *Raman spectra of pyridine adsorbed at a silver electrode*, Chemical Physics Letters **26**, 163 (1974).

[4] E. C. Le Ru, E. Blackie, M. Meyer, and P. G. Etchegoin, *Surface Enhanced Raman Scattering Enhancement Factors: A Comprehensive Study*, The Journal of Physical Chemistry C **111**, 13794 (2007).

[5] F. J. Garcia-Vidal, L. Martín-Moreno, and J. B. Pendry, *Surfaces with holes in them: new plasmonic metamaterials*, Journal of Optics A: Pure and Applied Optics **7**, S97 (2005).

[6] Nina Meinzer, William L. Barnes, and Ian R. Hooper, *Plasmonic meta-atoms and metasurfaces*, Nature Photonics **8**, 889 (2014).

[7] R. A. Shelby, D. R. Smith, and S. Schultz, *Experimental Verification of a Negative Index of Refraction*, Science **292**, 77 (2001).

[8] D. R. Smith, J. B. Pendry, and M. C. K. Wiltshire, *Metamaterials and Negative Refractive Index*, Science **305**, 788 (2004).

[9] Wenshan Cai and Vladimir Shalaev, *Optical Metamaterials* (Springer, New York, NY, 2010).

[10] Zhaowei Liu, Hyesog Lee, Yi Xiong, Cheng Sun, and Xiang Zhang, *Far-Field Optical Hyperlens Magnifying Sub-Diffraction-Limited Objects*, Science **315**, 1686 (2007).

[11] J. B. Pendry, *Negative Refraction Makes a Perfect Lens*, Physical Review Letters **85**, 3966 (2000).

[12] Fu Min Huang, Tsung Sheng Kao, Vassili A. Fedotov, Yifang Chen, and Nikolay I. Zheludev, *Nanohole Array as a Lens*, Nano Letters **8**, 2469 (2008).

[13] Francesco Aieta, Patrice Genevet, Mikhail A. Kats, Nanfang Yu, Romain Blanchard, Zeno Gaburro, and Federico Capasso, *Aberration-Free Ultrathin Flat Lenses and Axicons at Telecom Wavelengths Based on Plasmonic Metasurfaces*, Nano Letters **12**, 4932 (2012).

[14] Yang Zhao and Andrea Alù, *Manipulating light polarization with ultrathin plasmonic metasurfaces*, Physical Review B **84**, 205428 (2011).

[15] Nanfang Yu, Francesco Aieta, Patrice Genevet, Mikhail A. Kats, Zeno Gaburro, and Federico Capasso, *A Broadband, Background-Free Quarter-Wave Plate Based on Plasmonic Metasurfaces*, Nano Letters **12**, 6328 (2012).

[16] Carl Pfeiffer, Cheng Zhang, Vishva Ray, L. Jay Guo, and Anthony Grbic, *High Performance Bianisotropic Metasurfaces: Asymmetric Transmission of Light*, Physical Review Letters **113**, 023902 (2014).

[17] Xingjie Ni, Zi Jing Wong, Michael Mrejen, Yuan Wang, and Xiang Zhang, *An ultrathin invisibility skin cloak for visible light*, Science **349**, 1310 (2015).

[18] Thomas W. Ebbesen, H. J. Lezec, H. F. Ghaemi, T. Thio, and P. A. Wolff, *Extraordinary optical transmission through sub-wavelength hole arrays*, Nature **391**, 667 (1998).

[19] Frerik van Beijnum, Peter J. van Veldhoven, Erik Jan Geluk, Gert W. 't Hooft, and Martin P. van Exter, *Loss compensation of extraordinary optical transmission*, Applied Physics Letters **104**, 061112 (2014).

[20] Frerik van Beijnum, Peter J. van Veldhoven, Erik Jan Geluk, Michiel J. A. de Dood, Gert W. 't Hooft, and Martin P. van Exter, *Surface Plasmon Lasing Observed in Metal Hole Arrays*, Physical Review Letters **110**, 206802 (2013).

[21] M. A. Noginov, G. Zhu, A. M. Belgrave, R. Bakker, V. M. Shalaev, E. E. Narimanov, S. Stout, E. Herz, T. Suteewong, and U. Wiesner, *Demonstration of a spaser-based nanolaser.*, Nature **460**, 1110 (2009).

[22] Martin T. Hill, Yok-Siang Oei, Barry Smalbrugge, Youcai Zhu, Tjibbe de Vries, Peter J. van Veldhoven, Frank W. M. van Otten, Tom J. Eijkemans, Jaroslaw P. Turkiewicz, Huug de Waardt, Erik J. Geluk, Soon-Hong Kwon, Yong-Hee Lee, Richard Notzel, and Meint K. Smit, *Lasing in metallic-coated nanocavities*, Nature Photonics **1**, 589 (2007).

[23] Rupert F. Oulton, Volker J. Sorger, Thomas Zentgraf, Ren-Min Ma, Christopher Gladden, Lun Dai, Guy Bartal, and Xiang Zhang, *Plasmon lasers at deep subwavelength scale*, Nature **461**, 629 (2009).

[24] Ren-Min Ma, Rupert F. Oulton, Volker J. Sorger, Guy Bartal, and Xiang Zhang, *Room-temperature sub-diffraction-limited plasmon laser by total internal reflection*, Nature Materials **10**, 110 (2011).

[25] Xiangeng Meng, Jingjing Liu, Alexander V. Kildishev, and Vladimir M. Shalaev, *Highly directional spaser array for the red wavelength region*, Laser & Photonics Reviews **8**, 896 (2014).

[26] J. Stehr, J. Crewett, F. Schindler, R. Sperling, G. von Plessen, U. Lemmer, J.M. Lupton, T.A. Klar, J. Feldmann, A.W. Holleitner, M. Forster, and U. Scherf, *A Low Threshold Polymer Laser Based on Metallic Nanoparticle Gratings*, Advanced Materials **15**, 1726 (2003).

[27] Jae Yong Suh, Chul Hoon Kim, Wei Zhou, Mark D. Huntington, Dick T. Co, Michael R. Wasielewski, and Teri W. Odom, *Plasmonic Bowtie Nanolaser Arrays*, Nano Letters **12**, 5769 (2012).

[28] Wei Zhou, Montacer Dridi, Jae Yong Suh, Chul Hoon Kim, Dick T. Co, Michael R. Wasielewski, George C. Schatz, and Teri W. Odom, *Lasing action in strongly coupled plasmonic nanocavity arrays*, Nature Nanotechnology **8**, 506 (2013).

[29] A. Hinke Schokker, *Periodic and Aperiodic Plasmon Lattice Lasers*, Ph.D. thesis, University of Amsterdam, Amsterdam, 2016.

[30] Mohammad Ramezani, Alexei Halpin, Antonio I. Fernández-Domínguez, Johannes Feist, Said Rahimzadeh-Kalaleh Rodriguez, Francisco J. Garcia-Vidal, and Jaime Gómez Rivas, *Plasmon-exciton-polariton lasing*, Optica **4**, 31 (2017).

[31] Hua Zhang, L. Andrea Dunbar, Giacomo Scalari, Romuald Houdré, and Jérôme Faist, *Terahertz photonic crystal quantum cascade lasers*, Optics Express **15**, 16818 (2007).

[32] Y. Chassagneux, R. Colombelli, W. Maineult, S. Barbieri, H. E. Beere, D. A. Ritchie, S. P. Khanna, E. H. Linfield, and A. G. Davies, *Electrically pumped photonic-crystal terahertz lasers controlled by boundary conditions*, Nature **457**, 174 (2009).

[33] J. B. Pendry, L. Martín-Moreno, and F. J. Garcia-Vidal, *Mimicking Surface Plasmons with Structured Surfaces*, Science **305**, 847 (2004).

[34] Kazuaki Sakoda, *Optical Properties of Photonic Crystals* (Springer, Berlin, 2005).

[35] H. Kogelnik and C. V. Shank, *Coupled-Wave Theory of Distributed Feedback Lasers*, Journal of Applied Physics **43**, 2327 (1972).

[36] Kazuyoshi Hirose, Yong Liang, Yoshitaka Kurosaka, Akiyoshi Watanabe, Takahiro Sugiyama, and Susumu Noda, *Watt-class high-power, high-beam-quality photonic-crystal lasers*, Nature Photonics **8**, 406 (2014).

[37] M. P. van Exter, V. T. Tenner, F. van Beijnum, M. J. A. de Dood, P. J. van Veldhoven, E. J. Geluk, and G. W. 't Hooft, *Surface plasmon dispersion in metal hole array lasers*, Optics Express **21**, 27422 (2013).

[38] Pierre Berini and Israel De Leon, *Surface plasmon-polariton amplifiers and lasers*, Nature Photonics **6**, 16 (2012).

[39] Min W. Kim and P.-C. Ku, *Semiconductor nanoring lasers*, Applied Physics Letters **98**, 201105 (2011).

[40] Israel De Leon and Pierre Berini, *Amplification of long-range surface plasmons by a dipolar gain medium*, Nature Photonics **4**, 382 (2010).

[41] W. L. Barnes, W. A. Murray, J. Dintinger, E. Devaux, and T. W. Ebbesen, *Surface Plasmon Polaritons and Their Role in the Enhanced Transmission of Light through Periodic Arrays of Subwavelength Holes in a Metal Film*, Physical Review Letters **92**, 107401 (2004).

[42] P Lalanne, *A microscopic view of the electromagnetic properties of sub-λ metallic surfaces*, Surface Science Reports **64**, 453 (2009).

[43] F. J. Garcia-Vidal, L. Martin-Moreno, T. W. Ebbesen, and L. Kuipers, *Light passing through subwavelength apertures*, Reviews of Modern Physics **82**, 729 (2010).

[44] Frerik van Beijnum, Chris Rétif, Chris B. Smiet, Haitao Liu, Philippe Lalanne, and Martin P. van Exter, *Quasi-cylindrical wave contribution in experiments on extraordinary optical transmission*, Nature **492**, 411 (2012).

[45] Raffaele Colombelli, Kartik Srinivasan, Mariano Troccoli, Oskar Painter, Claire F. Gmachl, Donald M. Tennant, A. Michael Sergent, Deborah L. Sivco, Alfred Y. Cho, and Federico Capasso, *Quantum Cascade Surface-Emitting Photonic Crystal Laser*, Science **302**, 1374 (2003).

[46] W. L. Barnes, *Fluorescence near interfaces: The role of photonic mode density*, Journal of Modern Optics **45**, 661 (1998).

[47] ioffe, Semiconductor database of the Ioffe physical technical institute, St. Petersburg, Russia. http://www.ioffe.rssi.ru/SVA/NSM/Semicond/.

[48] P. Paddon and Jeff F. Young, *Two-dimensional vector-coupled-mode theory for textured planar waveguides*, Physical Review B **61**, 2090 (2000).

[49] D. M. Whittaker and I. S. Culshaw, *Scattering-matrix treatment of patterned multilayer photonic structures*, Physical Review B **60**, 2610 (1999).

[50] N. Rotenberg, M. Spasenović, T. L. Krijger, B. le Feber, F. J. García de Abajo, and L. Kuipers, *Plasmon Scattering from Single Subwavelength Holes*, Physical Review Letters **108**, 127402 (2012).

[51] C. Ropers, D. Park, G. Stibenz, G. Steinmeyer, J. Kim, D. Kim, and C. Lienau, *Femtosecond Light Transmission and Subradiant Damping in Plasmonic Crystals*, Physical Review Letters **94**, (2005).

[52] V. T. Tenner, A. N. van Delft, M. J. A. de Dood, and M. P. van Exter, *Loss and scattering of surface plasmon polaritons on optically-pumped hole arrays*, Journal of Optics **16**, 114019 (2014).

[53] Alexandre G. Brolo, Reuven Gordon, Brian Leathem, and Karen L. Kavanagh, *Surface Plasmon Sensor Based on the Enhanced Light Transmission through Arrays of Nanoholes in Gold Films*, Langmuir **20**, 4813 (2004).

[54] Ahmet A. Yanik, Min Huang, Osami Kamohara, Alp Artar, Thomas W. Geisbert, John H. Connor, and Hatice Altug, *An Optofluidic Nanoplasmonic Biosensor for Direct Detection of Live Viruses from Biological Media*, Nano Lett. **10**, 4962 (2010).

[55] H. Ditlbacher, J. R. Krenn, G. Schider, A. Leitner, and F. R. Aussenegg, *Two-dimensional optics with surface plasmon polaritons*, Applied Physics Letters **81**, 1762 (2002).

[56] A. Melikyan, L. Alloatti, A. Muslija, D. Hillerkuss, P. C. Schindler, J. Li, R. Palmer, D. Korn, S. Muehlbrandt, D. Van Thourhout, B. Chen, R. Dinu, M. Sommer, C. Koos, M. Kohl, W. Freude, and J. Leuthold, *High-speed plasmonic phase modulators*, Nature Photonics **8**, 229 (2014).

[57] William L. Barnes, Alain Dereux, and Thomas W. Ebbesen, *Surface plasmon subwavelength optics*, Nature **424**, 824 (2003).

[58] Ren-Min Ma, Rupert F. Oulton, Volker J. Sorger, and Xiang Zhang, *Plasmon lasers: coherent light source at molecular scales: Plasmon lasers: coherent light source at molecular scales*, Laser & Photonics Reviews **7**, 1 (2013).

[59] H. Gao, J. M. McMahon, M. H. Lee, J. Henzie, S. K. Gray, G. C. Schatz, and T. W. Odom, *Rayleigh anomaly-surface plasmon polariton resonances*

in palladium and gold subwavelength hole arrays, Optics Express **17**, 2334 (2009).

[60] I. Vurgaftman, J. R. Meyer, and L. R. Ram-Mohan, *Band parameters for III–V compound semiconductors and their alloys*, Journal of Applied Physics **89**, 5815 (2001).

[61] K Petermann, *Laser diode modulation and noise* (Kluwer Academic Publishers ; KTK Scientific Publishers ; Sold and distributed in the U.S.A. and Canada by Kluwer Academic Publishers, Dordrecht; Boston; Tokyo; Norwell, MA, 1988).

[62] Sheng S Li, *Semiconductor physical electronics* (Plenum, New York, 1993).

[63] B. Tromborg, H.E. Lassen, and H. Olesen, *Traveling wave analysis of semiconductor lasers: modulation responses, mode stability and quantum mechanical treatment of noise spectra*, IEEE Journal of Quantum Electronics **30**, 939 (1994).

[64] F. van Beijnum, A.S. Meeussen, C. Rétif, and M.P. van Exter, *Rayleigh scattering of surface plasmons by sub-wavelength holes*, Optics Express **22**, 10317 (2014).

[65] V. T. Tenner, M. J. A. de Dood, and M. P. van Exter, *Measurement of the Phase and Intensity Profile of Surface Plasmon Laser Emission*, ACS Photonics **3**, 942 (2016).

[66] R. W. Gerchberg and W. O. Saxton, *Practical Algorithm for Determination of Phase from Image and Diffraction Plane Pictures*, Optik **35**, 237 (1972).

[67] James R. Fienup, *Phase retrieval algorithms: a personal tour [Invited]*, Applied optics **52**, 45 (2013).

[68] J. M. Rodenburg and H. M L Faulkner, *A phase retrieval algorithm for shifting illumination*, Applied Physics Letters **85**, 4795 (2004).

[69] K. Sakai, E. Miyai, T. Sakaguchi, D. Ohnishi, T. Okano, and S. Noda, *Lasing band-edge identification for a surface-emitting photonic crystal laser*, IEEE Journal on Selected Areas in Communications **23**, 1335 (2005).

[70] Eiji Miyai, Kyosuke Sakai, Takayuki Okano, Wataru Kunishi, Dai Ohnishi, and Susumu Noda, *Photonics: Lasers producing tailored beams*, Nature **441**, 946 (2006).

[71] M. Notomi, H. Suzuki, and T. Tamamura, *Directional lasing oscillation of two-dimensional organic photonic crystal lasers at several photonic band gaps*, Applied Physics Letters **78**, 1325 (2001).

[72] Masahiro Imada, Alongkarn Chutinan, Susumu Noda, and Masamitsu Mochizuki, *Multidirectionally distributed feedback photonic crystal lasers*, Physical Review B **65**, (2002).

[73] Yan Cui, Ravi S. Hegde, In Yee Phang, Hiang Kwee Lee, and Xing Yi Ling, *Encoding molecular information in plasmonic nanostructures for anti-counterfeiting applications*, Nanoscale **6**, 282 (2014).

[74] Na Liu, Martin Mesch, Thomas Weiss, Mario Hentschel, and Harald Giessen, *Infrared Perfect Absorber and Its Application As Plasmonic Sensor*, Nano Letters **10**, 2342 (2010).

[75] C. Haffner, W. Heni, Y. Fedoryshyn, J. Niegemann, A. Melikyan, D. L. Elder, B. Baeuerle, Y. Salamin, A. Josten, U. Koch, C. Hoessbacher, F. Ducry, L. Juchli, A. Emboras, D. Hillerkuss, M. Kohl, L. R. Dalton, C. Hafner, and J. Leuthold, *All-plasmonic Mach–Zehnder modulator enabling optical high-speed communication at the microscale*, Nature Photonics **9**, 525 (2015).

[76] O. Hess, J. B. Pendry, S. A. Maier, R. F. Oulton, J. M. Hamm, and K. L. Tsakmakidis, *Active nanoplasmonic metamaterials*, Nature Materials **11**, 573 (2012).

[77] Jeremy Baumberg, Mikhail Noginov, Javier Aizpurua, Kaiqiang Lin, Thomas Ebbesen, Alexei A Kornyshev, Riccardo Sapienza, Niek van Hulst, Santhosh Kotni, F. Javier García de Abajo, Pavel Ginzburg, Ortwin Hess, Mark Brongersma, and Sergey Bozhevolnyi, *Quantum plasmonics, gain and spasers: general discussion*, Faraday Discuss. **178**, 325 (2015).

[78] John D. Joannopoulos, Steven G. Johnson, Joshua N. Winn, and Robert D. Meade, *Photonic Crystals: Molding the Flow of Light (Second Edition)* (Princeton University Press, Princeton, 2011).

[79] W. Streifer, R.D. Burnham, and D.R. Scifres, *Radiation losses in distributed feedback lasers and longitudinal mode selection*, IEEE Journal of Quantum Electronics **12**, 737 (1976).

[80] Y. Chassagneux, R. Colombelli, W. Maineult, S. Barbieri, S. P. Khanna, E. H. Linfield, and A. G. Davies, *Graded photonic crystal terahertz quantum cascade lasers*, Applied Physics Letters **96**, 031104 (2010).

[81] Gangyi Xu, Raffaele Colombelli, Suraj P. Khanna, Ali Belarouci, Xavier Letartre, Lianhe Li, Edmund H. Linfield, A. Giles Davies, Harvey E. Beere, and David A. Ritchie, *Efficient power extraction in surface-emitting semiconductor lasers using graded photonic heterostructures*, Nature Communications **3**, 952 (2012).

[82] Geert Morthier and Patrick Vankwikelberge, *Handbook of Distributed Feedback Laser Diodes, Second Edition* (Artech House, Boston, 2013).

[83] Martin T. Hill, *Status and prospects for metallic and plasmonic nano-lasers [Invited]*, J. Opt. Soc. Am. B **27**, B36 (2010).

[84] Kyosuke Sakai, Eiji Miyai, and Susumu Noda, *Two-dimensional coupled wave theory for square-lattice photonic-crystal lasers with TM-polarization*, Optics express **15**, 3981 (2007).

[85] K. Sakai, E. Miyai, and S. Noda, *Coupled-Wave Theory for Square-Lattice Photonic Crystal Lasers With TE Polarization*, IEEE Journal of Quantum Electronics **46**, 788 (2010).

[86] I. Vurgaftman and J.R. Meyer, *Design optimization for high-brightness surface-emitting photonic-crystal distributed-feedback lasers*, IEEE Journal of Quantum Electronics **39**, 689 (2003).

[87] Rudolf F. Kazarinov and Charles H. Henry, *Second-order distributed feedback lasers with mode selection provided by first-order radiation losses*, Quantum Electronics, IEEE Journal of **21**, 144 (1985).

[88] C. Ferreira Fernandes, *Mode spectrum and threshold gain calculations in DFB lasers*, Microwave and Optical Technology Letters **12**, 363 (1996).

[89] Toshihiko Makino and Jan Glinski, *Transfer matrix analysis of the amplified spontaneous emission of DFB semiconductor laser amplifiers*, Quantum Electronics, IEEE Journal of **24**, 1507 (1988).

[90] P. Vankwikelberge, G. Morthier, and R. Baets, *CLADISS-a longitudinal multimode model for the analysis of the static, dynamic, and stochastic behavior of diode lasers with distributed feedback*, IEEE Journal of Quantum Electronics **26**, 1728 (1990).

[91] Joseph W. Goodman, *Introduction To Fourier Optics* (Roberts and Company Publishers, Englewood, Colorado, 2005).

[92] L. J. Allen and M. P. Oxley, *Phase retrieval from series of images obtained by defocus variation*, Optics communications **199**, 65 (2001).

[93] Alon Greenbaum and Aydogan Ozcan, *Maskless imaging of dense samples using pixel super-resolution based multi-height lensfree on-chip microscopy*, Optics Express **20**, 3129 (2012).

[94] S. Marchesini, *A unified evaluation of iterative projection algorithms for phase retrieval*, Review of Scientific Instruments **78**, 011301 (2007).

[95] V. T. Tenner, M. J. A. de Dood, and M. P. van Exter, *Surface plasmon dispersion in hexagonal, honeycomb and kagome plasmonic crystals*, Optics Express **24**, 29624 (2016).

[96] J. B. Pendry, D. Schurig, and D. R. Smith, *Controlling Electromagnetic Fields*, Science **312**, 1780 (2006).

[97] Justyna K. Gansel, Michael Thiel, Michael S. Rill, Manuel Decker, Klaus Bade, Volker Saile, Georg von Freymann, Stefan Linden, and Martin Wegener, *Gold Helix Photonic Metamaterial as Broadband Circular Polarizer*, Science **325**, 1513 (2009).

[98] Hikaru Saito and Naoki Yamamoto, *Size dependence of bandgaps in a two-dimensional plasmonic crystal with a hexagonal lattice*, Optics Express **23**, 2524 (2015).

[99] W. L. Barnes, T. W. Preist, S. C. Kitson, and J. R. Sambles, *Physical origin of photonic energy gaps in the propagation of surface plasmons on gratings*, Physical Review B **54**, 6227 (1996).

[100] Jean-Luc R. Stevens, Philipp Rudiger, and James A. Bednar, in *HoloViews: Building Complex Visualizations Easily for Reproducible Science* (http://conference.scipy.org, Austin, 2015), pp. 61–69.

[101] Sadao Adachi and John Wiley & Sons, *Physical properties of III-V semiconductor compounds InP, InAs, GaAs, GaP, InGaAs, and InGaAsP* (Wiley, New York, 1992).

[102] Takayuki Okamoto and Satoshi Kawata, *Dispersion relation and radiation properties of plasmonic crystals with triangular lattices*, Optics Express **20**, 5168 (2012).

[103] M. Kerker, D.-S. Wang, and C. L. Giles, *Electromagnetic scattering by magnetic spheres*, Journal of the Optical Society of America **73**, 765 (1983).

[104] Haitao Liu and Philippe Lalanne, *Microscopic theory of the extraordinary optical transmission*, Nature **452**, 728 (2008).

[105] Haitao Liu and Philippe Lalanne, *General properties of the surface charge pattern of one-dimensional metallic gratings*, Optics Express **21**, 16753 (2013).

[106] Xin Zhang, Haitao Liu, and Ying Zhong, *Microscopic analysis of surface Bloch modes on periodically perforated metallic surfaces and their relation to extraordinary optical transmission*, Physical Review B **89**, 195431 (2014).

[107] D. V. Coevorden, *Light propagation in Ordered and Disordered Media*, Ph.D. thesis, Universiteit van Amsterdam, 1997.

[108] Shanhui Fan and J. D. Joannopoulos, *Analysis of guided resonances in photonic crystal slabs*, Physical Review B **65**, 235112 (2002).

[109] Virginie Lousse, Wonjoo Suh, Onur Kilic, Sora Kim, Olav Solgaard, and Shanhui Fan, *Angular and polarization properties of a photonic crystal slab mirror*, Optics Express **12**, 1575 (2004).

[110] Simon Bernard, Christoph Reinhardt, Vincent Dumont, Yves-Alain Peter, and Jack C. Sankey, *Precision resonance tuning and design of SiN photonic crystal reflectors*, Optics Letters **41**, 5624 (2016).

[111] Wonjoo Suh, M. F. Yanik, Olav Solgaard, and Shanhui Fan, *Displacement-sensitive photonic crystal structures based on guided resonance in photonic crystal slabs*, Applied Physics Letters **82**, 1999 (2003).

[112] Chong Pei Ho, Prakash Pitchappa, Piotr Kropelnicki, Jian Wang, Hong Cai, Yuandong Gu, and Chengkuo Lee, *Two-dimensional photonic-crystal-based Fabry–Perot etalon*, Optics Letters **40**, 2743 (2015).

[113] Masahiro Imada, Susumu Noda, Alongkarn Chutinan, Takashi Tokuda, Michio Murata, and Goro Sasaki, *Coherent two-dimensional lasing action in surface-emitting laser with triangular-lattice photonic crystal structure*, Applied Physics Letters **75**, 316 (1999).

[114] M. Meier, A. Mekis, A. Dodabalapur, A. Timko, R. E. Slusher, J. D. Joannopoulos, and O. Nalamasu, *Laser action from two-dimensional distributed feedback in photonic crystals*, Applied Physics Letters **74**, 7 (1999).

[115] Y. Chassagneux, R. Colombelli, W. Maineult, S. Barbieri, S. P. Khanna, E. H. Linfield, and A. G. Davies, *Predictable surface emission patterns in terahertz photonic-crystal quantum cascade lasers*, Optics Express **17**, 9491 (2009).

[116] K. J. Moh, X.-C. Yuan, J. Bu, R. E. Burge, and Bruce Z. Gao, *Generating radial or azimuthal polarization by axial sampling of circularly polarized vortex beams*, Applied Optics **46**, 7544 (2007).

[117] Yu Tokizane, Kazuhiko Oka, and Ryuji Morita, *Supercontinuum optical vortex pulse generation without spatial or topological-charge dispersion*, Optics Express **17**, 14517 (2009).

[118] Ignacio Moreno, Jeffrey A. Davis, Isaac Ruiz, and Don M. Cottrell, *Decomposition of radially and azimuthally polarized beams using a circular-polarization and vortex-sensing diffraction grating*, Optics Express **18**, 7173 (2010).

[119] Kyoko Kitamura, Kyosuke Sakai, Naoki Takayama, Masaya Nishimoto, and Susumu Noda, *Focusing properties of vector vortex beams emitted by photonic-crystal lasers*, Optics Letters **37**, 2421 (2012).

[120] Gerard Nienhuis, *Analogies between optical and quantum mechanical angular momentum*, Philosophical Transactions of the Royal Society A **375**, 20150443 (2017).

[121] Felix Bloch, *Über die Quantenmechanik der Elektronen in Kristallgittern*, Zeitschrift für Physik **52**, 555 (1929).

[122] Léon Brillouin, *Les électrons dans les métaux et le classement des ondes de de Broglie correspondantes*, Comptes Rendus Hebdomadaires des Séances de l'Académie des Sciences **191**, 292 (1930).

[123] A. E. Siegman, *Lasers* (University Science Books, Stanford, 1986).

[124] Yong Liang, Chao Peng, Kenji Ishizaki, Seita Iwahashi, Kyosuke Sakai, Yoshinori Tanaka, Kyoko Kitamura, and Susumu Noda, *Three-dimensional coupled-wave analysis for triangular-lattice photonic-crystal surface-emitting lasers with transverse-electric polarization*, Optics Express **21**, 565 (2013).

Curriculum Vitae

Vasco Tenner

2001-2007	High school degree VWO (NT and NG profile), Lorentz Casimir Lyceum, Eindhoven
2007-2011	Bachelor Physics and Astrophysics, University of Amsterdam Bachelor thesis: *X-ray scattering experiments on rare-earth titanate compounds.* Supervised by Prof. dr. J. Goedkoop.
2010	International exchange student at Lund University, Sweden
2011-2013	Master Advanced Matter and Energy Physics, University of Amsterdam / Vrije universiteit Amsterdam Graduated cum laude (with distinction) Master thesis: *Development of novel methods for broadband lensless imaging.* Supervised by dr. S. Witte, Laserlab, Vrije universiteit Amsterdam.
2013-2017	PhD candidate, Leiden University Thesis: *Surface plasmon lasers* Supervised by prof. dr. M. P. van Exter and prof. dr. E. R. Eliel. Teaching assistant for experimental physics and for atomic and molecular physics.

List of publications

- M. P. van Exter, V. T. Tenner, F. van Beijnum, M. J. A. de Dood, P. J. van Veldhoven, E. J. Geluk, and G. W. ’t Hooft, *Surface plasmon dispersion in metal hole array lasers*, Optics Express **21**, 27422 (2013).
- S. Witte, V. T. Tenner, D. W. E. Noom, and K. S. E. Eikema, *Lensless diffractive imaging with ultra-broadband table-top sources: from infrared to extreme-ultraviolet wavelengths*, Light: Science & Applications **3**, e163 (2014).
- V. T. Tenner, A. N. van Delft, M. J. A. de Dood, and M. P. van Exter, *Loss and scattering of surface plasmon polaritons on optically-pumped hole arrays*, Journal of Optics **16**, 114019 (2014).
- V. T. Tenner, K. S. E. Eikema, and S. Witte, *Fourier transform holography with extended references using a coherent ultra-broadband light source*, Optics Express **22**, 25397 (2014).
- V. T. Tenner, M. J. A. de Dood, and M. P. van Exter, *Measurement of the Phase and Intensity Profile of Surface Plasmon Laser Emission*, ACS Photonics **3**, 942 (2016).
- V. T. Tenner, M. J. A. de Dood, and M. P. van Exter, *Surface plasmon dispersion in hexagonal, honeycomb and kagome plasmonic crystals*, Optics Express **24**, 29624 (2016).

Summary

Surface plasmons (SPs) are surface waves at the interface between a dielectric and a good metal, such as silver and gold, and are formed by the interaction between light and the free electrons at the metal-dielectric interface. They provide strong field confinement for optical fields, opening new possibilities for enhanced light-matter interaction. Surface plasmons can be efficiently coupled to free-space photons by scattering on a periodic lattice of nanometer-size holes, i.e., a metal hole array.

Lasers are known to emit coherent, monochromatic, and strongly directional beams. There are two essential components to a laser: a (pumped) gain medium and a resonator. The gain medium amplifies the field and the resonator confines the laser mode and supplies the feedback needed to obtain coherence.

In this thesis, we describe experiments on SP propagation and SP lasing in active two-dimensional metal hole arrays operating at telecom wavelengths ($\lambda \sim 1500$ nm) and cryogenic temperatures. The gain is provided by an optically pumped InGaAs semiconductor layer closely spaced to a metallic gold film. A resonator for SPs is created by scattering on an array of holes in the gold film. As the feedback in metal hole arrays is distributed over the whole device, we are dealing with a distributed feedback laser instead of a Fabry-Pérot laser. Distributed feedback lasers provide a strong laser mode selection and stable operating wavelength.

We have studied such active hole arrays with square and hexagonal lattice symmetries both below and above their lasing threshold. We have investigated the role of the symmetry of the lattice on the SP propagation and SP lasing. We have explored the laser frequencies and the feedback mechanism of these SP lasers, and observed the spatial profile and direction of the emitted laser beams. The structure of this thesis is depicted schematically in the table below. The following paragraphs will give an overview of the contents of each chapter.

	□	△ ⬡ ▱
Below threshold	**Chapter 2** SP dispersion & SP scattering **Chapter 3** Loss & SP-photon scattering	**Chapter 5** SP-SP scattering & link to single hole scattering
Above threshold	**Chapter 4** Intensity, phase & feedback	**Chapter 6** Tuning between lasing in two modes

In order to understand SP lasing in metal hole arrays, we first need to understand SP propagation in metal hole arrays which can be studied by operating the SP lasers below their laser threshold. In chapter 2 we study metal hole arrays with a square lattice. We obtain the resonance frequencies from angle-dependent spectra and identify four SP bands. These four bands emit light with distinct polarizations. Three bands emit p-polarized light and one band emits s-polarized light. We develop a theoretical framework that quantitatively predicts these bands. This coupled-mode model is a central component in the thesis. Its main constituents are traveling SP waves in four directions and scattering of these traveling waves by the holes. This scattering couples the traveling waves, and thereby produces standing-wave components and induces energy splittings between the bands. We link the observed splitting between bands to scattering of SPs on the holes.

Which laser mode is active depends on the gain and loss of the available modes. In chapter 3, we identify and quantify the loss mechanisms of SPs in metal hole arrays by measuring the linewidths and intensity of the SP modes below laser threshold. The main loss channels are radiative loss and ohmic loss.

SP lasers in metal hole arrays emit donut shaped beams, i.e. the emission is limited to a small ring with a dark center. In chapter 4 we unravel mechanisms that are responsible for this feature. In order to understand what is happening inside the device, we measure the field profile of the laser beam, i.e., we observe both the intensity and the phase of the emitted light. The phase was retrieved with a novel beam-block method and an iterative algorithm. SP lasers in square arrays emit donut shaped beams that have a radial polarization profile. The observed fields do not agree with standard one-dimensional distributed feedback theory. We identify position dependent gain as the missing element, extend the distributed feedback theory with it, and find good agreement between theory and experiment. This is a prime example in which the observation of the phase of a wave phenomenon gives vital information about the studied problem.

In contrast to lattices with a square symmetry, lattices with a hexagonal symmetry have principal directions that are not perpendicular. In chapter 5 we study the influence of the lattice symmetry on the SP propagation by measuring the optical dispersion of three hexagonal based lattices with increasing complexity in the unit cell: hexagonal, honeycomb and Kagome. We retrieve angle-dependent scattering rates of these lattices and find that these rates are dominated by the hole density and not by the complexity of the unit cell. The observed angle-dependent scattering can be explained by a single-hole model based on electric and magnetic dipoles.

In chapter 6, we demonstrate SP lasing in hexagonal plasmonic crystals. We observe lasing in two modes with different polarization and intensity profiles. Tuning between these modes is achieved by changing the size of the pump spot. We link this observation to previous experimental and theoretical work on photonic crystals. Furthermore, we explain the mode and polarization profiles from symmetry arguments and show that a compact description of the mode profiles can be given in terms of a sum of orbital angular momentum (OAM) beams.

Samenvatting

Oppervlakteplasmonen zijn elektromagnetische oppervlaktegolven op het grensvlak tussen een isolator en een goed metaal, zoals zilver of goud. Ze bestaan door de interactie tussen licht en de vrije elektronen op het metaaloppervlak. Ze kunnen het optische veld sterk opsluiten waardoor er nieuwe mogelijkheden ontstaan voor verbeterde licht-materiaal wisselwerking. Oppervlakteplasmonen kunnen efficiënt worden omgezet naar fotonen in de vrije ruimte door verstrooiing aan een periodiek rooster met nanometerschaal gaatjes, een zogenaamd metalen gatenrooster.

Van lasers is bekend dat ze coherente, monochromatische en sterk gerichte lichtbundels uitzenden. Voor een laser zijn twee bestanddelen nodig: een (gepompt) lasermedium en een trilholte. Het lasermedium versterkt het veld. De trilholte sluit het veld op en voorziet de laser van de benodigde terugkoppeling om coherentie te verkrijgen.

In dit proefschrift beschrijven we proeven aan oppervlakteplasmonvoortplanting en oppervlakteplasmonlasers in actieve tweedimensionale gatenroosters. Deze roosters worden gekoeld tot cryogene temperaturen en stralen bij telecom golflengtes ($\lambda \sim 1500$ nm). De versterking van de oppervlakteplasmonen wordt geleverd door een optisch-gepompte InGaAs halfgeleiderlaag die vlakbij de goudfilm staat waaraan de de plasmonen gebonden zijn. Door verstrooiing in het gatenrooster ontstaat er een trilholte voor de oppervlakteplasmonen. Deze terugkoppeling vindt plaats op het hele rooster en daarom hebben we te maken met verspreide-terugkoppeling-lasers in plaats van Fabry-Pérot lasers. In verspreide-terugkoppeling-lasers is er een duidelijke keuze van de laser mode en daardoor een stabiele golflengte.

We bestuderen actieve gatenroosters met vierkante en zeshoekige roostersymmetrieën. We bestuderen de roosters zowel onder als boven hun laserdrempels. We onderzoeken de invloed van de roostersymmetrie op oppervlakteplasmonvoortplanting en oppervlakteplasmonlasers. We verkennen de frequenties en het terugkoppelmechanisme van deze oppervlakteplasmonlasers. We observeren het ruimtelijke profiel en richting van de uitgezonden laserbundel. De structuur van dit proefschrift is schematisch uitgebeeld in de hierop volgende tabel. De volgende paragrafen geven voor ieder hoofdstuk een samenvatting.

	□	△⬡▱
Onder drempel	**Hoofdstuk 2** Oppervlakteplasmondispersie & oppervlakteplasmonverstrooiing **Hoofdstuk 3** Verliezen & oppervlakteplasmon-foton verstrooiing	**Hoofdstuk 5** Oppervlakteplasmon-oppervlakteplasmon verstrooiing & verbinding met enkel-gat model
Boven drempel	**Hoofdstuk4** Intensiteit, fase & terugkoppeling	**Hoofdstuk 6** Schakelen tussen oppervlakteplasmonlasers in twee toestanden

Om te begrijpen hoe oppervlakteplasmonlasers in gatenroosters werken, moeten we eerst weten hoe oppervlakteplasmonen zich voortplanten door zulke roosters. In hoofdstuk 2 bestuderen we oppervlakteplasmonvoortplanting onder de laserdrempel in gatenroosters met een vierkante symmetrie. We verkrijgen de resonantiefrequentie uit hoekopgeloste spectra en herkennen vier SP-banden. Deze vier oppervlakteplasmonbanden zenden licht uit met verschillende polarisatie. Drie van deze banden stralen p-gepolariseerd licht uit en één band straalt s-gepolariseerd licht uit. We ontwikkelen een theoretisch raamwerk dat een centrale rol speelt in het gehele proefschrift. De belangrijkste ingrediënten zijn lopende oppervlakteplasmongolven die in vier richtingen reizen en de verstrooiing van deze golven op de gaatjes. Deze verstrooiing koppelt de lopende golven en daardoor ontstaan staande-golf componenten en energieverschillen tussen de banden. Wij verbinden de gemeten splitsingen tussen de banden aan de sterkte van de verstrooiing van oppervlakteplasmonen op de gaatjes.

Welke lasertoestand actief is hangt af van de versterking en verliezen van de beschikbare optische toestanden. In hoofdstuk 3 stellen we de verliesmechanismes van de oppervlakteplasmonen vast en bepalen we hun grootte. We doen dit door de lijnbreedtes en de intensiteit van de oppervlakteplasmonbanden te meten onder de laserdrempel. De voornaamste verlieskanalen zijn stralings- en Ohmse verliezen.

Oppervlakteplasmonlasers in gatenroosters zenden donutvormige laserbundels uit, met andere woorden het licht zit alleen in een smalle ring en in het midden is het donker. In hoofdstuk 4 ontrafelen we het verantwoordelijke mechanisme. Om te begrijpen wat er binnen in de laser gebeurt meten we het gehele veld van de laserbundel, dat wil zeggen dat we zowel het intensiteits- als het faseprofiel meten. Het faseprofiel verkrijgen we met behulp van een nieuwe bundelblokkeermethode en een iteratief algoritme. Oppervlakteplasmonlasers in roosters met een vierkante symmetrie zenden donutvormige laserbundels uit met een radiaal polarisatiepatroon. De waargenomen velden komen niet overeen met de standaard verspreide-terugkoppeling-lasertheorie. Wij identificeren positieafhankelijke versterking als ontbrekend element, breiden de verspreide-terugkoppeling-lasertheorie ermee uit en verkrijgen een goede overeenkomst tussen waarneming en theorie. Dit is een voorbeeld van een probleem waarbij de waarneming van de fase van een golfverschijnsel essentiële informatie verschaft.

In tegenstelling tot roosters met een vierkante symmetrie staan bij zeshoekige roosters de hoofdrichtingen niet loodrecht op elkaar. In hoofdstuk 5 bestuderen we de invloed van de roostersymmetrie op de voortplanting van oppervlakteplasmonen. Daarvoor meten we de optische dispersie van drie verschillende hexagonale roosters met steeds complexere eenheidscellen. We bestuderen preparaten met een hexagonaal, een honingraat en een Kagome rooster. We verkrijgen de hoekafhankelijke verstrooiing van deze roosters en ontdekken dat die wordt gedomineerd door de dichtheid van gaatjes en niet door de complexiteit van de eenheidscel. De waargenomen hoekafhankelijke verstrooiing kan worden uitgelegd aan de hand van een enkel-gat-model dat gebaseerd is op elektrische en magnetische dipolen.

In hoofdstuk 6 demonstreren we oppervlakteplasmonlasers in hexagonale plasmonische kristallen. Deze laser kan in twee toestanden werken met verschillende polarisatie- en intensiteitsprofielen. We kunnen schakelen tussen deze toestanden door de grootte van de pompbundel aan te passen. We verbinden deze waarneming aan bestaande experimenten en theorie over fotonische kristallen. Verder leggen we de intensiteits- en polarisatieprofielen uit met symmetrie argumenten en laten we zien dat er een bondige beschrijving van de profielen kan worden gegeven in termen van sommen van lichtbundels met een baanimpulsmoment.

Dankwoord

Door samen te werken gebeurt er meer. Dat geldt ook voor mijn onderzoek. Ik ben dankbaar voor de samenwerking en discussies die ik met mijn collega's heb kunnen voeren. Een aantal mensen wil ik extra bedanken.

In het bijzonder bedank ik mijn promotor en dagelijks begeleider Martin van Exter. Ik kreeg van hem alle ruimte en vrijheid om het onderzoek te ontwikkelen. Specifiek bedank ik Martin voor zijn eindeloze enthousiasme voor licht, voor zijn ideeën over plasmonen en natuurkunde, voor zijn hulp bij het opzetten van mathematische modellen, voor zijn steun bij tegenslagen en voor zijn grote geduld bij het corrigeren van dit manuscript.

Met veel plezier heb ik met Michiel vele zinvolle en ook vele zinloze discussies gevoerd over een breed scala aan onderwerpen, variërend tussen plasmonische bandenstructuren tot de wilde beesten in Canada, zowel op de universiteit, als op de fiets naar huis en tijdens een conferentie in San Jose.

Verder bedank ik Eric Eliel als promotor voor de scherpe en constructieve feedback op de tekst van dit proefschrift. Dirk Boonzajer Flaes heeft bijgedragen met aanwijzingen voor iteratieve phase retrieval algorithms en het beschikaar stellen van de computercode gebruikt voor de omslag van mijn proefschrift. I thank Philippe Lalanne and Liu Haitao for the useful discussions about quasi-cylindrical waves and Matthias Saba for the discussions about surface plasmon lasers. I also thank the authors of the Holoviews python package for their fast response on questions and bug reports.

Tijdens mijn promotie hebben drie studenten mijn onderzoek vooruit geholpen met hun projecten. André van Delft heeft metingen gedaan aan de dispersie van vierkante roosters zoals beschreven in hoofdstuk 3, Johan Bosman heeft record-lage lijnbreedtes van SP lasers waargenomen en Michel Hubert heeft samples met elliptische gaatjes bestudeerd. De samenwerking met jullie heb ik als een verrijking van mijn promotie ervaren.

De preparaten die ik heb bestudeerd zijn gemaakt in de cleanroom van de Technische Universiteit Eindhoven. Frerik van Beijnum maakte de eerste preparaten. De preparaten die ik later heb gemaakt zouden niet werken zonder de hulp van Erik Jan Geluk, Barry Smalbrugge, Tjibbe de Vries en René van Veldhoven. Furthermore, I thank Rosalinda Gaudio and Michele Cotrufo for their tips and company in the clean room.

Ik heb veel plezier gehad van de goede technische ondersteuning van de fijnmechanische dienst, de elektronische dienst en de cryogene afdeling en bedank in het bijzonder Harmen van der Meer, Emiel Wiegers, Peter van Veldhuizen, Arno

van Amersfoort, Hans Kuyk, Wilfred van der Geest en Ruud Kuyvenhoven. Ik ben dank verschuldigd aan Henriette van Leeuwen voor haar snelle administratieve ondersteuning.

Een gezellige en respectvolle sociale omgeving was voor mij belangrijk voor het succesvol afronden van mijn promotie. Ik wil graag de hele vakgroep bedanken voor het scheppen hiervan.

Mijn hele familie heeft me altijd gestimuleerd om te studeren en te onderzoeken en is altijd enthousiast en nieuwsgierig geweest naar mijn onderzoek. Verder bedank ik Anne Rietmeijer voor het proeflezen van de Nederlandse teksten in dit proefschrift.

Tot slot, dank ik Rosalie, die mijn leven zo veel leuker maakt.